Unraveling the Elusive Solvation Structure of Aqueous Ions

using advanced spectroscopic techniques

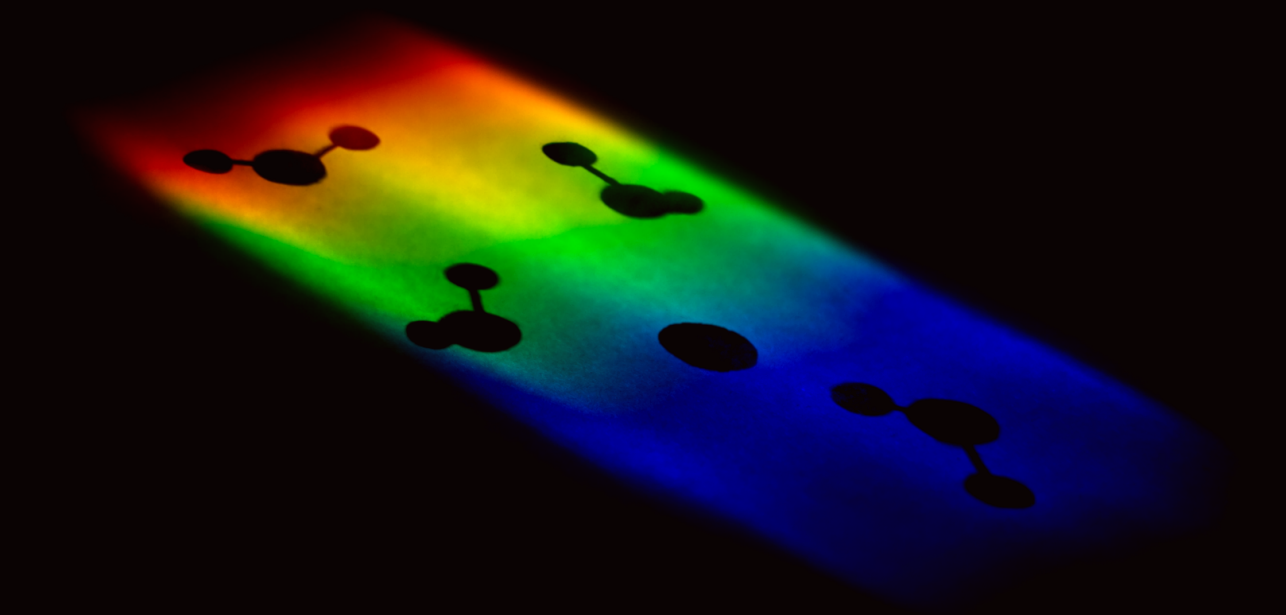

Roberto Cota

Unraveling the elusive solvation structure of aqueous ions using advanced spectroscopic techniques

Roberto Oziel Gutierrez Cota

Cover image: artistic picture of a spectroscopic experiment in which molecules are indirectly observed through the shadows that they cast.

Designed by Kateryna Kulakova & Roberto Cota

ISBN: 978-94-028-1999-1

Digital version of this thesis is available at https://dare.uva.nl

Printed and bound by Ipskamp Printing B.V.

Amsterdam, Netherlands, 2020

Unraveling the elusive solvation structure of aqueous ions using advanced spectroscopic techniques

ACADEMISCH PROEFSCHRIFT

ter verkrijging van de graad van doctor
aan de Universiteit van Amsterdam
op gezag van de Rector Magnificus
prof. dr. ir. K.I.J. Maex
ten overstaan van een door het College voor Promoties ingestelde commissie,
in het openbaar te verdedigen in de Aula der Universiteit

op vrijdag 30 oktober 2020, te 11:00 uur

door

Roberto Oziel Gutierrez Cota

geboren te Leon

Promotiecommissie:

Promotoren:	Prof. dr. S. Woutersen	Universiteit van Amsterdam
	Prof. dr. H. J. Bakker	Universiteit van Amsterdam
Overige leden:	Prof. dr. R. Buchner	Universität Regensburg
	Prof. dr. E. H. G. Backus	Universität Wien
	Prof. dr. W. J. Buma	Universiteit van Amsterdam
	Prof. dr. E. J. Meijer	Universiteit van Amsterdam
	Dr. B. Ensing	Universiteit van Amsterdam
Faculteit:	Faculteit der Natuurwetenschappen, Wiskunde en Informatica	

The research covered in this thesis was conducted in the Molecular Photonic Group at the Van 't Hoff Institute for Molecular Sciences, University of Amsterdam, and the Ultrafast Spectroscopy Group at AMOLF, Amsterdam. This work was financially supported by the Netherlands Organisation for Scientific Research (NWO). Grant number: 12PR2989.

A mi familia

&

to all those who were part of
this unforgettable journey

To the reader

This thesis encompasses the
journey across my PhD
This implicitly contains the laughter
and the tears of almost five years
This is part of me
in your hands
This is
many mistakes
many successes
many colleagues
many friends

A quien leyere

Esta tesis es evidencia del
camino a través de mi doctorado
Sus espacios en blanco hablan
de las alegrías y el esfuerzo de casi cinco años
En tus manos sujetas una parte de mí
Aquí hay
muchos errores
muchos aciertos
muchos compañeros
muchos amigos

Unraveling the elusive solvation structure of aqueous ions using advanced spectroscopic techniques

Publications covered in this thesis:

Chapter 4: R. Cota, N. Ottosson, H. J. Bakker, S. Woutersen. *Evidence for reduced hydrogen-bond cooperativity in ionic solvation shells from isotope-dependent dielectric relaxation.* Phys. Rev. Lett. **2018**, 120, 216001.

Chapter 5: R. Cota, N. Ottosson, H. J. Bakker, S. Woutersen. *Accurate hydration numbers of alkali-metal ions using isotope-dependent dielectric relaxation.* To be submitted.

Chapter 6: R. Cota, H. J. Bakker, S. Woutersen. *Solvation structure and dynamics of hydronium and hydroxide in water investigated with isotope-dependent dielectric relaxation spectroscopy.* To be submitted.

Chapter 7: R. Cota, E. P. van Dam, S. Woutersen, H. J. Bakker. *Slowing down of the molecular reorientation of water in concentrated alkaline solutions.* J. Phys. Chem. B **2020**, Accepted for publication.

Chapter 8: R. Cota, S. Woutersen, H. J. Bakker. *Accelerated vibrational energy relaxation of water in alkaline environments.* Submitted.

Chapter 9: R. Cota*, A. Tiwari*, B. Ensing, H. J. Bakker, S. Woutersen. *Hydration interactions beyond the first solvation shell in aqueous phenolate solution.* Phys. Chem. Chem. Phys. **2020**, 22, 19940–19947.

*These authors contributed equally to this work.

Other collaborations:

W. J. Smit, E. P. van Dam, R. Cota, H. J. Bakker. *Caffeine and taurine slow down water molecules.* J. Phys. Commun. **2019**, 3, 025010.

Contents

◀ *I faced the challenge of observing molecules with the help of state-of-the-art experimental techniques. Here, the reader must perform one last experiment using, by far, the most advanced observation instrument that we have: the human eye.*

(Hint: watch it horizontally)

1 Introduction

1.1 Water: a structured material

Despite being the most familiar and abundant compound on earth, water has captivated humankind for centuries. Since ancient times, for example, humans have wondered at the property of ice to float on liquid water, which is the consequence of water having a lower density as a solid than as a liquid. This anomalous behavior finds its origin in the nature of water to form structures: crystal-like networks that increase the volume of the system when it freezes. This example belongs to a long list of anomalies as compared to other liquids,[1] many of which are linked to the structured character of water. However, in spite of considerable efforts, a precise description of its structural properties remains elusive to date.[2]

In liquid water, hydrogen bonds are considered the intermolecular "glue" that gives rise to the structure called the hydrogen-bond network. In this network, each hydrogen bond results from the (mainly electrostatic) bonding between one of the partially positive hydrogen atoms and one of the lone-pair electrons in neighboring water molecules. Thus, each water molecule has the potential to participate in the formation of four hydrogen bonds: donating two (two hydrogen atoms) and accepting two (two lone-pair electrons), as depicted in Figure 1.1. As was validated in 1933 using X-rays, the perfect arrangement of water molecules leads to a periodic tetrahedral structure.[3]

Recent studies show, however, that liquid water possesses on average 3.5 hydrogen bonds per molecule in ambient conditions.[4–6] This means that the hydrogen-bond network is defective to the extent that it allows changes in the local coordi-

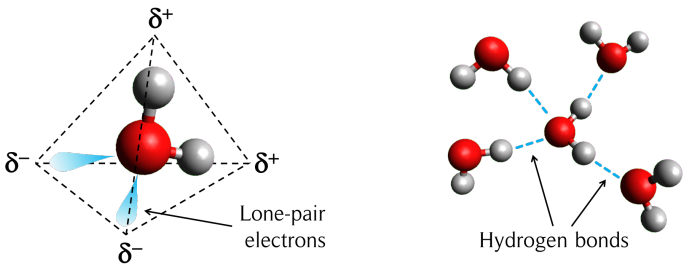

Figure 1.1. Left: Tetrahedral configuration of a water molecule. **Right:** Local hydrogen-bond structure of a water molecule that extends to form the so-called hydrogen-bond network of liquid water.

nates as well as structural rearrangements, which have been observed to occur on a sub-picosecond ($\leq 10^{-12}$ s) time scale.[7–10] As such, the hydrogen-bond network of water is a highly active and adaptive environment. It is thus not surprising that many chemical and biological processes occur in aqueous environments—an excellent environment for life to prosper in.[11–13]

Yet, water is often regarded as a stiff liquid, a concept introduced by Marcus,[14,15] in which the hydrogen bonding leads to cooperative dynamics. This cooperativity constrains the mobility of water molecules themselves, as well as the dynamics of other molecules dissolved in water. In aqueous solutions, the solutes can reciprocally affect the cooperative behavior due to discontinuities and defects in the hydrogen-bond network of water. If the concentration of solutes in water is high enough, one can observe changes in the macroscopic properties of water: the viscosity and surface tension increases or decreases depending on the nature of the solute.

1.2 The influence of ions on the structure of water

The way in which ions, among other solutes, modify the structural dynamics of water has been a long-standing question and is an active field of experimental and theoretical research. An accurate description of ion-water interactions is of importance for the study of many chemical and biological processes, ranging from the conformation of proteins to the selection rules for ion exchange in living cells.

In electrolyte solutions, ions generate strong local electric fields that modify the hydrogen-bond structure and induce local molecular ordering in the form of solvation shells. Based on the degree of water structuring in solvation shells, ions are classified as structure makers or structure breakers, concepts coined by Gurney

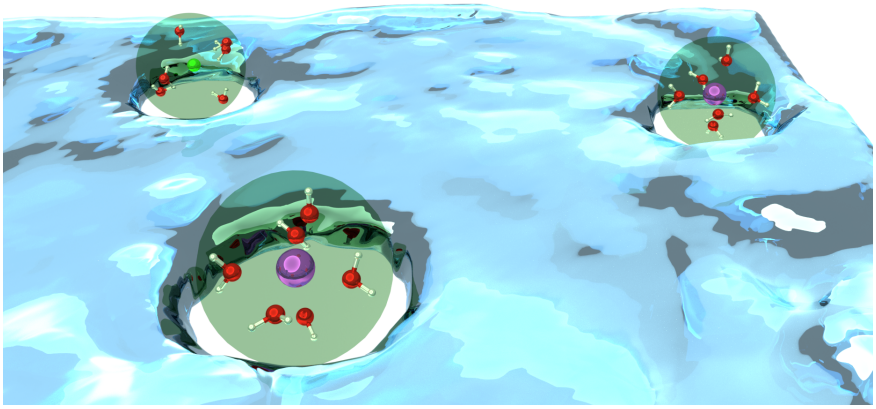

Figure 1.2. Visual representation of ions dissolved in water, and of ion–water solvation interactions. The strong local electric field of ions induce local ordering in the form of solvation shells. The structural dynamics of solvating water molecules differ from that of water molecules in neat bulk water. As such, the hydrogen-bond network is said to be locally broken.

in the 50s.[16] In this context, while small ions with high surface charge densities are structure makers that form tight solvation shells, large ions form labile solvation structures due to their low surface charge density.

Most of the work that has been carried out to study ion-water interactions has been reviewed by Yizhak Marcus[14,17] and Hitoshi Ohtaki[18] in three publications that have become a benchmark for the field of solvation. The evolution of the different techniques and their accuracy is observed in these publications. However, the spread in the reviews' results from the different techniques show that a precise description of solvation shells is still lacking.

These discrepancies find their origin in the fact that each technique is sensitive to different time scales and spatial ranges. For instance, scattering methods like X-ray and neutron diffraction deliver static snapshots of ionic structures. These techniques can be used to determine the packing capacity of water molecules around ions; a quantity referred to as *coordination number*. Large ions have large coordination numbers which do not reflect the strength of the solvation interactions, nor dynamic properties such as the residence time of water molecules in solvation shells.

In contrast, the hydration number is a wider concept that represents the capacity of ions to bind water molecules long enough that they diffuse with the ion as a whole. Hydration numbers are phenomenologically represented with the Hofmeister series, which follows the surface charge density of the ions under study, i.e. $Li^+ > Na^+ > K^+ > Cs^+$. This explains why Cs^+, which is weakly hydrated, dif-

fuses faster through water than the strongly hydrated Na^+ ion.[19] A straightforward method to determine hydration numbers is based on ionic mobility: from the diffusion coefficients one can determine the effective Stokes radii of ions.[20] This method intrinsically incorporates dynamic properties, however, ions (with their solvation structures) are considered to be perfect spheres immersed in a uniform continuum (as depicted in Figure 1.2), which is not entirely valid due to the local disruption of the hydrogen-bond network. Another problem in many experiments is the difficulty of separating the corresponding contributions of the cation and of the anion.

From the previous examples, one can deduce that in order to accurately estimate hydration numbers we require experimental techniques that directly measure the influence of ions on the structural dynamics of water. This calls for the adoption of techniques with a (sub)picosecond temporal resolution (the time scale of the structural fluctuations of water), and a method to separate the contributions of cations and anions.

1.3 Towards a better understanding of ion solvation

Over the last 20 years, the experimental situation has substantially improved with the advent of (i) vector network analyzers (VNA) with high (GHz) frequencies; and (ii) femtosecond laser pulses. Both instruments have the ability to retrieve data with high temporal resolution, which has been successfully exploited to study molecular dynamics.[8,9,21–43]

In particular, information on solvating structures and the dynamics of the hydrogen-bond network is obtained from the reorientation dynamics of water molecules,[22,23,25–28,34,36,40] a property which is the cornerstone of this thesis.

1.3.1 Macroscopic observation of the collective behavior of water

VNA-based dielectric relaxation spectroscopy (DRS) has been used to explore the structure and dynamics of polar molecules.[22,24,27,30,32–37,42] From DRS measurements, the dielectric constant defines the magnitude of the polarization that results from the reorientation of dipolar molecules in an applied electric field. In liquid water, the dielectric constant reflects the overall molecular dynamics, which incorporate the cooperative behavior of the hydrogen-bond network. As such, in electrolyte solutions, changes in the dielectric constant can be attributed to variations in the microscopic structure of water, e.g. the disruption of the hydrogen-bond network of water and the local molecular ordering in the form of solvation shells.

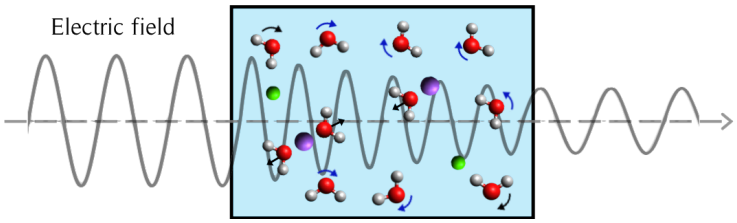

Figure 1.3. Schematic representation of dielectric relaxation spectroscopy. If an external electric field is applied, water molecules will reorient towards the direction of the electric field. However, in the presence of ions, the degrees of rotational freedom of some water molecules are reduced or even locked in local structures referred to as solvation shells.

This technique has the advantage of being primarily sensitive to solvation shells of positive ions. Cations restrict hydrating water molecules to rotations around their main symmetry axis, in which their permanent dipole moments are said to be rotationally immobilized. In contrast, around anions, the dipole moment of hydrating water molecules can rotate and react to external electric fields similar to those molecules in bulk water. The details of this disparity are left for subsequent chapters.

Concerning the solvation properties of ions, Richard Buchner and colleagues have carried out many studies using DRS.[33,44–54] In an excellent publication that has inspired part of the work presented in this thesis, Buchner has reported hydration numbers for several ions from combined DRS measurements, using theoretical predictions in order to separate static and kinetic contributions.[27]

Going one step further, we aim to determine hydration numbers by investigating the kinetic contribution to the depolarization experimental manner. In **Chapter 2**, we introduce the theoretical background and experimental methodology for the study of ion solvation using VNA-based DRS. In **Chapter 4**, we present a new method to extract hydration numbers based on the isotope dependence of the dielectric response. In this chapter, we aim to quantify the reduced cooperativity of water due to the local disruption of the hydrogen-bond network. In **Chapter 5**, we apply this method to establish hydration numbers of a series of alkali-metal ions, and observe the ion-size dependence. Subsequently, in **Chapter 6**, we present similar analyses to estimate the number of water molecules affected by aqueous H^+ and OH^- ions.

1.3.2 Microscopic observation of solvating water molecules

Femtosecond laser pulses have been used to perform ultrafast time-resolved vibrational spectroscopy (TRVS). This technique has been used to study molecular properties, e.g. molecular reorientation,[23,25,26,28,40] binding interactions,[8,9,38,39,41]

and energy equilibration.[21,29,31] In this experimental approach, the way that light couples to the vibrational motion of molecules permits the exploration of structures down to the scale of a chemical bond (∼1 Å). An aspect of particular interest is that the vibrational resonances of molecules, as well as the associated vibrational relaxation rates, are sensitive to the structure and dynamics of the surrounding environment. This structure-dependent character allows us to assess the structural dynamics of solvating water molecules, as well as the properties of the hydrogen-bond network.

In particular, the vibrational properties of the hydroxyl groups of water molecules are affected by the hydrogen bonds that they donate, and consequently, by the strength of the hydrogen-bonding interactions in their vicinity.[7,55,56] A clear proof of this effect is observed in the OH-stretch resonance that shifts from 3657 cm^{-1} in the gas phase (no hydrogen bonds) to lower frequencies around 3400 cm^{-1} in the hydrogen-bonded liquid. This means that hydrogen bonds weaken the strength of the OH covalent bonds of water.

In electrolyte solutions, the vibrational dynamics of water molecules near ions further changes due to the strong local electric fields and the disruption of the hydrogen-bond network of water. In aqueous perchlorate (ClO_4^-) solutions, for example, there are two well-defined OH stretch bands: the first band associated with the bulk OH stretch vibration with a resonant frequency of 3400 cm^{-1} and the second band at higher frequencies associated with OH oscillators that form weak hydrogen bonds with perchlorate ions.[31] One can thus selectively target and study the vibrational dynamics of solvating or bulk-like water molecules. As has been shown previously, TRVS experiments based on the OH stretch vibration are quite insensitive to the presence of cations.[57,58] This can be explained by the fact that no hydrogen bonds are donated to positive ions. This characteristic contrasts with DRS experiments.

Polarization-resolved TRVS experiments provide direct information on the reorientation dynamics of the probed OH vibrations. Previous studies have shown a significant slowing down of the molecular dynamics upon the addition of ions. In fact, the reorientation dynamics of water in anionic solvation shells are strongly constrained to rotations within a cone around the axis defined by the directional hydrogen bond of the OH group to the anion.[59–61] In addition, the wiggling motion of the OH group bonded to the anion restricts the formation of hydrogen bonds between water molecules in the first solvation shell and the outer environment. Hence, the slow-down effect is limited to the first solvation shell, and the hydrogen-bond network is accordingly disrupted.[14] In contrast, aqueous sugar solutions have shown a slowing down effect that extends beyond the first solvation shell. This is explained by the fact that, instead of a disruptive effect, the hydroxyl groups of the sugar molecules form part of the hydrogen-bond network.[62,63]

Protons (H^+) and hydroxide ions (OH^-) have the ability to form hydration complexes in which the excess charge is delocalized, and structural rearrangements lead

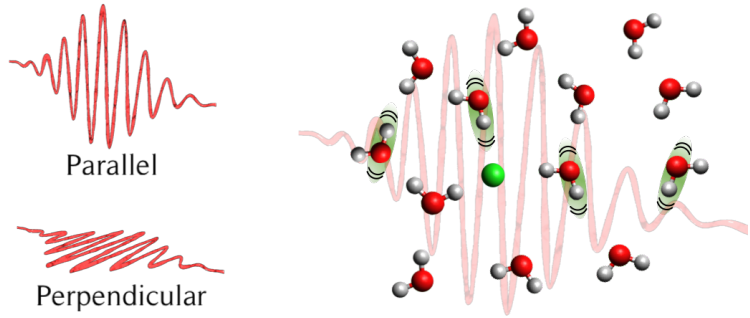

Figure 1.4. Schematic representation of time-resolved vibrational spectroscopy. An initial femtosecond pump pulse couples to local vibrational resonances of water molecules, which are afterwards tracked with a second femtosecond pulse called probe. In polarization-resolved TRVS, the sample is probed both in parallel and perpendicular configuration in order to observe molecular reorientation dynamics.

to proton transfer between neighboring water molecules. This effect has been a fascinating subject of intense research in the last two decades. However, while a fairly large number of experimental efforts have been carried out on acid solutions,[64–68] only a few experimental studies in alkaline solutions have been reported.[69–73] As has been discussed before,[74] this disparity can be explained from the classical view that hydroxide ions (OH^-, proton hole) mirror the effect of proton transfer via hydronium ions (H_3O^+, proton excess). Nonetheless, recent theoretical studies have shown that OH^- and H_3O^+ ions have different structural properties, calling for the study of hydroxide ions as a subject of independent experimental research.[75–81]

In **Chapter 3**, we introduce the theoretical background and experimental methodology for the study of intermolecular interactions in aqueous solutions using TRVS. **Chapters 7** and **8** focus on the study of structural properties in aqueous alkaline solutions using TRVS. In **Chapter 7**, we performed polarization-resolved measurements to explore whether hydroxide ions have an influence on the dynamics of water molecules beyond the first solvation shell. In **Chapter 8**, we explore whether the hydration complexes that hydroxide ions form can play a role in dissipating vibrational energy of surrounding molecules, an effect that has been observed in acidic solutions and has been attributed to the hydronium ion.[31] Finally, in **Chapter 9**, we study the solvation properties of aqueous phenolate ions using polarization-resolved TRVS and molecular dynamics simulations.

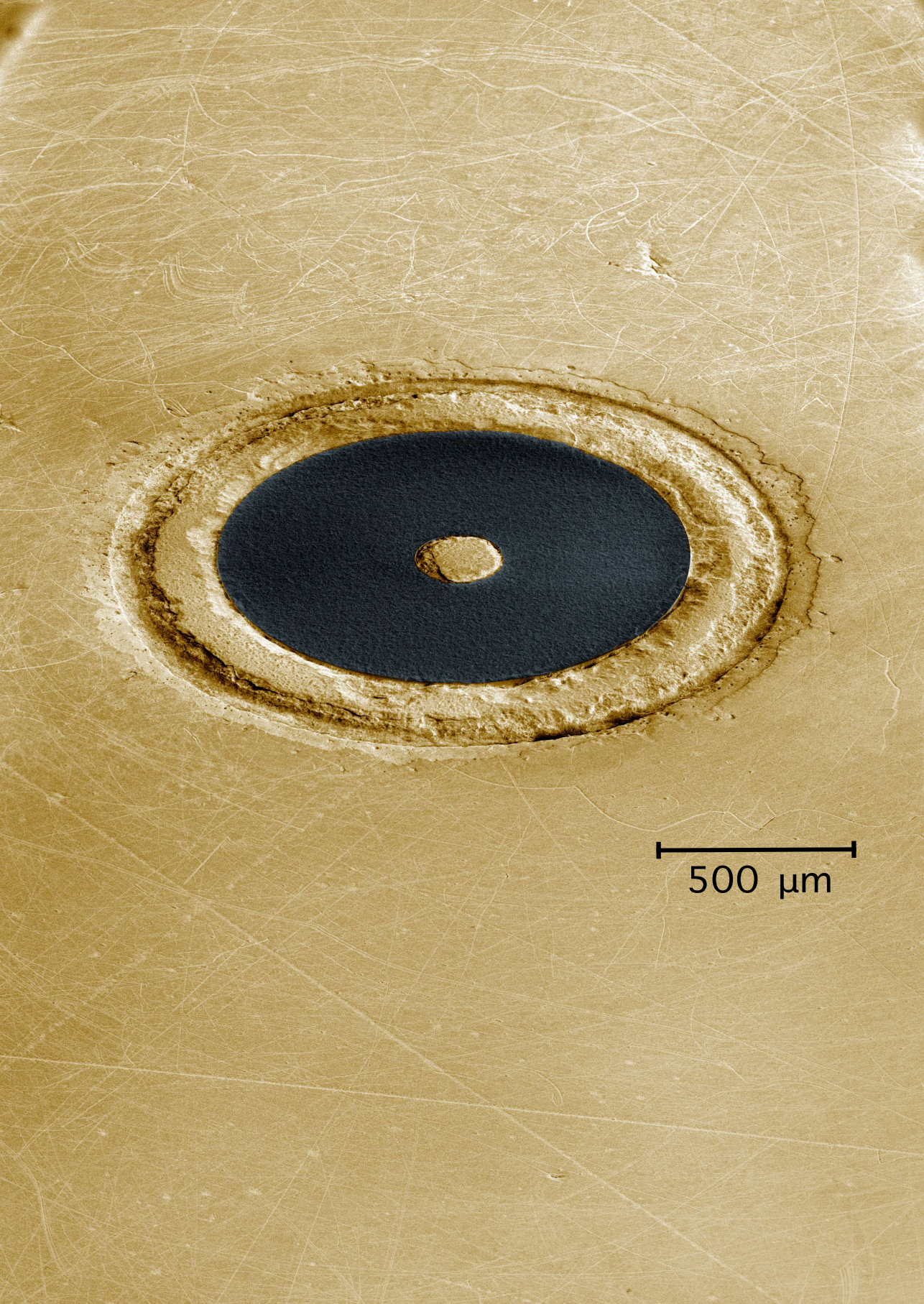
500 µm

◀ *Top view of the coaxial-probe head used for dielectric relaxation measurements. The marks on the surface show the erosion caused throughout the experiments presented in Chapters 4–6.*

SEM Photo, Lukas Helmbrecht. Edition, Roberto Cota

2

Methods I
Dielectric relaxation spectroscopy

The polarization properties of aqueous solutions, intimately linked to molecular structuring and solvation properties, are discussed in this chapter. First, we introduce the concept of dipole moment reorientation that results from the interaction with external electric fields. Then, we provide the microscopic molecular description underlying the observed macroscopic dielectric properties. As such, we can use dielectric relaxation spectroscopy to study molecular mobility and molecular cooperativity. If electrolyte solutions are our samples of interest, we can determine the extent to which ions affect the hydrogen bonding interactions of water. The discussion on the local ordering effect of water molecules in solvation shells is also one of the main goals of this chapter. Finally, the data analysis and modeling of the dielectric relaxation measurements are described.

2.1 Electromagnetic waves interacting with matter

A complete (classical) description of propagating electromagnetic fields can be performed by means of the Maxwell equations[82]

$$\nabla \cdot \vec{D} = \rho_e, \tag{2.1}$$

$$\nabla \cdot \vec{B} = 0, \tag{2.2}$$

$$\nabla \times \vec{E} = -\frac{\partial \vec{B}}{\partial t}, \tag{2.3}$$

$$\nabla \times \vec{H} = \vec{j} + \frac{\partial \vec{D}}{\partial t}, \tag{2.4}$$

in which Eq. 2.1 shows that the electric displacement $\vec{D}$ is determined by the distribution of electric charges ρ_e. Gauss's law for magnetism, Eq. 2.2, states that the net magnetic field $\vec{B}$ over a closed surface must be zero, meaning that magnetic monopoles cannot exist. The Maxwell-Faraday equation, Eq. 2.3 describes the induction of electric fields as the result of time-varying magnetic fields. While Ampère's law, Eq. 2.4, indicates the induced magnetic fields due to electrical currents and time-varying electric fields.

For an homogeneous and isotropic material with intrinsic properties that are time-independent, one can derive the following three constitutive equations

$$\vec{D} = \epsilon_0 \vec{E} + \vec{P} = \epsilon_0 \hat{\epsilon} \vec{E}, \tag{2.5}$$

$$\vec{B} = \mu_0 \vec{H} + \vec{M} = \mu_0 \hat{\mu} \vec{H}, \tag{2.6}$$

$$\vec{j} = \kappa \vec{E}, \tag{2.7}$$

where $\vec{P}$ and $\vec{M}$ are the polarization and magnetization density vectors, respectively. The material properties are described by the complex relative electric permittivity $\hat{\epsilon}$ and the complex relative magnetic permeability $\hat{\mu}$. These properties can also be expressed with the electric and magnetic susceptibilities of the material as $\hat{\epsilon} = 1 + \hat{\chi}_e$ and $\hat{\mu} = 1 + \hat{\chi}_m$. The quantities ϵ_0 and μ_0 describe the permittivity and permeability of free space. The quantity κ is the specific conductivity of the material. It is important to notice that Eqs. 2.1-2.7 constitute a set of linear equations to compute all kind of electromagnetic interactions.

From Eq. 2.5, one can observe that the electric displacement results from the polarization response of the material due to electric forces. This polarization response can involve a displacement of the electron cloud of atoms or molecules with respect of the unperturbed state. It can also involve the reorientation of a dipolar molecular towards the direction of the electric field $\vec{E}$. In the case of static electric fields, the complex permittivity reduces to the so-called static permittivity

ϵ_s, which is also commonly referred to as dielectric constant. The latter quantity defines the total static polarization.

Due to microscopic interactions and inertial effects, the reaction of the medium to an applied external electric field is not instantaneous. Instead, the system requires a time interval to reorient following the direction of the external field, meaning that the polarization effect is delayed with respect to the electric field $\vec{E}$. If we consider a monochromatic oscillating electric field $\vec{E}(t) = \vec{E}_0 cos(\omega t)$ with amplitude $\vec{E}_0$, a phase shift between $\vec{D}$ and $\vec{E}$ will emerge that depends on the frequency ω:

$$\vec{D}(t) = \vec{D}_0 \cos[\omega t - \delta(\omega)], \tag{2.8}$$

with $\delta(\omega)$ the frequency-dependent phase delay, which is also referred to as loss angle. Notice that $\vec{D}_0 = \epsilon_0 \hat{\epsilon}(\omega)\vec{E}_0$ according to Eq. 2.5.

By introducing the following reciprocal representation in the complex plane

$$\vec{D}_0[\cos\delta - i\sin\delta] = \epsilon_0 \vec{E}_0[\epsilon' - i\epsilon''], \tag{2.9}$$

the electric displacement given in Eq. 2.8 can be expressed with the following formula

$$\vec{D}(t) = \epsilon'(\omega)\epsilon_0 \vec{E}_0 \cos(\omega t) + \epsilon''(\omega)\epsilon_0 \vec{E}_0 \sin(\omega t). \tag{2.10}$$

The preceding equation shows that the electric displacement arises from two effects with different nature: (i) the in-phase dielectric dispersion is proportional to the real part of the relative permittivity, while (ii) the out-of-phase dielectric dissipation (dielectric loss) is proportional to the imaginary part of the relative permittivity. It is clear from Eq. 2.10 that the mathematical formulation can be promoted to complex notation, i.e. $\hat{\vec{D}} = \epsilon_0 \hat{\epsilon} \hat{\vec{E}}$. Notice that a similar delayed response can occur between the magnetic flux $\vec{B}$ and the magnetic field strength $\vec{H}$, and therefore Eq. 2.6 can be analogously written as Eq. 2.10.

One can describe the evolution of the electromagnetic fields as plane waves with the following functional forms

$$\hat{\vec{E}}(\vec{r}, t) = \hat{\vec{E}}(\vec{r}) \exp(i\omega t), \tag{2.11}$$

$$\hat{\vec{H}}(\vec{r}, t) = \hat{\vec{H}}(\vec{r}) \exp(i\omega t), \tag{2.12}$$

which in combination of Eqs. 2.1–2.7 (with a net electric charge of zero, i.e $\nabla \cdot \vec{D} = 0$) lead to the following wave equations

$$\nabla^2 \hat{\vec{E}}(\vec{r}) + \hat{k}^2 \hat{\vec{E}}(\vec{r}) = 0, \tag{2.13}$$

$$\nabla^2 \hat{\vec{H}}(\vec{r}) + \hat{k}^2 \hat{\vec{H}}(\vec{r}) = 0, \tag{2.14}$$

that describe the propagation of electromagnetic waves through a material. A solution to Eq. 2.13 is given by $\vec{E}(\vec{r}) = E_0 \exp\left(i\vec{k}\cdot\vec{r}\right)$, where $\hat{k}$ is the wave vector expressed by

$$\hat{k}^2 = k_0^2 \left[\hat{\mu}(\omega)\hat{\epsilon}(\omega) + \frac{\hat{\mu}(\omega)\hat{\kappa}(\omega)}{i\omega\epsilon_0}\right]. \tag{2.15}$$

with $k_0 (= \omega\sqrt{\mu_0\epsilon_0} = \omega/c)$ the propagation constant in vacuum. The preceding equation describes the response of a medium to electromagnetic fields, and shows the extent to which the propagation of the field deviates from that observed in free space.

For electrolyte solutions, which are the focus of interest in this work, the wave vector can be written as

$$\hat{k}^2 = k_0^2 \left[\hat{\epsilon}(\omega) + \frac{\sigma}{i\omega\epsilon_0}\right], \tag{2.16}$$

where $\hat{\kappa}(\omega)$ reduces to the DC ionic conductivity σ, since its frequency dependence is irrelevant in the frequency range of our interest (∼18 GHz the characteristic dielectric relaxation mode of water).[44,83–85]

In electrolyte solutions, the energy loss (imaginary part) arises from the non-instantaneous rearrangement of charges in the dielectric medium, as well as from the work exerted by rotating dipoles. The real part of the dielectric dispersion is related to the temporarily stored energy, and determined by the degree of orientation of the dipoles along the direction of the electric field.

2.2 Polarization

The polarization of a medium can be defined as the net macroscopic dipole per volume of a medium in the presence of an electric field. From Eq. 2.5, one can write

$$\hat{\vec{P}} = (\hat{\epsilon} - 1)\epsilon_0 \hat{\vec{E}}, \tag{2.17}$$

in which the polarization is described as the dielectric response of the medium to $\hat{\vec{E}}$. The underlying microscopic definition can be understood as the sum of two contributions

$$\hat{\vec{P}} = \hat{\vec{P}}_\mu + \hat{\vec{P}}_\alpha \tag{2.18}$$

where $\hat{\vec{P}}_\mu$ refers to the orientational response of molecular dipoles, while $\hat{\vec{P}}_\alpha$ is attributed to the polarization resulting from the intramolecular polarizability.

These two contribution are generally well separated. The orientational relaxation of dipoles along the applied electric field typically takes place in the order of picoseconds or slower, such as the dielectric response of water with a time constant of ∼8 ps at room temperature. While the molecular polarizability takes place at the femtosecond timescale. Thus, $\hat{\vec{P}}_\mu$ and $\hat{\vec{P}}_\alpha$ are considered independent with each other, leading to

$$\hat{\vec{P}}_\mu = \epsilon_0(\hat{\epsilon} - \epsilon_\infty)\hat{\vec{E}}, \qquad \text{and} \qquad \hat{\vec{P}}_\alpha = \epsilon_0(\epsilon_\infty - 1)\hat{\vec{E}}, \tag{2.19}$$

with ϵ_∞ the permittivity in the intermediate frequency region at which dipoles are insensitive to the fast oscillating field, but the molecular polarizability has attained its maximum amplitude. Experiments focused on the dipolar orientation effect in aqueous solutions have shown that ϵ_∞ is constant in the GHz frequency region.[86] In the limit of a static electric field ($\omega \to 0$), the orientational polarization reduces to $\vec{P}_{\mu,0} = \epsilon_0(\epsilon_\mathrm{s} - \epsilon_\infty)\vec{E}_0$. The static permittivity ϵ_s is attained when all types of polarizations reach equilibrium with a switched-on DC electric field. The microscopic description is discussed in the following section.

2.3 Microscopic description of static permittivity

The macroscopic static permittivity can be connected to the microscopic notion of the collection of molecular dipoles aligned along the direction of the external field.

Under the action of an electric field, dipoles tend to reorient towards the direction of the electric field in order to minimize their internal energy, defined as

$$U(\theta) = -\vec{\mu} \cdot \vec{E} = -\mu E \cos\theta, \tag{2.20}$$

where θ represents the angle between the dipole moment vector $\vec{\mu}$ and the electric field vector $\vec{E}$. Thus, it is clear to see that the minimum energy is attained at $\theta = 0$, which mean a perfect alignment to the electric field. Such a situation is physically unaccessible since it means a system in perfect order with no entropy– this could theoretically occur at extremely low temperatures at which, ironically, the molecules would not have enough energy to rotate and align with the electric field. At non-zero temperatures the molecules will diffuse and rotate constantly because of the thermal energy of the system.

Under the action of an external electric field, the orientation of the dipoles is slightly shifted from the random distribution, leading to an effective (averaged) dipole moment $\langle\vec{\mu}\rangle$. If we assume that the medium is formed by only one type of dipoles, the polarization can be written as

$$\vec{P} = \rho\langle\vec{\mu}\rangle, \tag{2.21}$$

which is proportional to the density ρ of dipolar molecules.

In this view, the system is formed by dipoles with a statistical distribution between $\theta_{\min} = 0$ and $\theta_{\max} = \pi$. The Boltzmann distribution equation can be used to determine the fraction of dipoles with a certain energy U:

$$N(U) = A \exp\left(-\frac{U(\theta)}{k_{\mathrm{B}}T}\right) \tag{2.22}$$

with T and k_{B} the temperature of the system and the Boltzmann constant, respectively. Given the preceding equation, the averaged dipole moment can be obtained summing up the contribution of all possible states, as follows

$$\langle\vec{\mu}\rangle = \frac{\int_0^{\pi} N[U(\theta)] \cdot \mu \cos\theta \cdot d\Omega}{\int_0^{\pi} N[U(\theta)] \cdot d\Omega} \tag{2.23}$$

where $d\Omega$ ($= 2\pi \sin\theta d\theta$) is the solid angle increment on a unit sphere when θ changes to $\theta + d\theta$. Notice that Ω account for the three-dimensional system, in which the polarization is invariant to rotations over the azimuthal angle around the electric field vector. The solution to Eq. 2.23 yields $\langle\vec{\mu}\rangle = \mu \mathrm{L}(\xi)$, with L the Langevin equation, and $\xi = \mu E/k_{\mathrm{B}}T$. In the limit of $\xi \ll 1$ (which is valid even for very strong electric fields and strong dipoles), $\mathrm{L}(\xi) \simeq \xi/3$, we reach to the Langevin-Debye equation for the induced polarization is obtained[87,88]

$$\vec{P} = \frac{\rho\mu^2}{3k_{\mathrm{B}}T}\vec{E} = \epsilon_0(\epsilon_{\mathrm{s}} - \epsilon_{\infty})\vec{E}, \tag{2.24}$$

and thus:

$$\epsilon_{\mathrm{s}} - \epsilon_{\infty} = \frac{\rho\mu^2}{3\epsilon_0 k_{\mathrm{B}}T}. \tag{2.25}$$

2.3.1 The Lorentz cavity field and Debye's theory of dielectrics

The above description assumes that each molecule is solely affected by the action of the external field, and the total polarization is the result of the collection of individual contributions. However, a dipole immerse in the system will be also affected by the macroscopic polarization of the system $\vec{P}$. The force that a given polar molecules experiences arises from the sum of the external field and the collective polarization of the system, such that

$$\vec{E}_{\mathrm{loc}} = \vec{E} + \frac{\vec{P}}{3\epsilon_0} \qquad \Longrightarrow \qquad \vec{E}_{\mathrm{loc}} = \frac{\epsilon_{\mathrm{s}} + 2}{3}\vec{E}, \tag{2.26}$$

which is known as the Lorentz cavity field.[89] In this approach, one assumes that each dipole is inside a small spherical cavity with a charge distribution at the surface as the result of the macroscopic polarization. As can be seen in Eqs. 2.21 and 2.26, the Lorentz field acts parallel to the applied field $\vec{E}$ and effectively enhances the response of the dipoles.

Debye was the first one to use this notion to model the temperature-dependent dielectric constant, which Eq. 2.25 failed to predict. With this approach Debye derived

$$\frac{\epsilon_\mathrm{s} - 1}{\epsilon_\mathrm{s} + 2} = \frac{\rho\mu^2}{9\epsilon_0 k_\mathrm{B} T} + \frac{\rho\alpha}{3\epsilon_0}, \tag{2.27}$$

or if we consider the Clausius-Mossotti relation for molecular polarizability α,[90] the dielectric constant can be written as

$$\frac{\epsilon_\mathrm{s} - 1}{\epsilon_\mathrm{s} + 2} - \frac{\epsilon_\infty - 1}{\epsilon_\infty + 2} = \frac{\rho\mu^2}{9\epsilon_0 k_\mathrm{B} T}, \tag{2.28}$$

which is limited to estimate the dielectric response of gases and dilute solutions of polar molecules in non-polar solvents due to assumptions in defining Eq. 2.26.

Furthermore, if the term for polarizability is neglected, one can derive a critical behavior for the dielectric constant with the following functional form

$$\epsilon_\mathrm{s} = \frac{T + 2T_c}{T - T_c}, \qquad \text{with} \qquad T_c = \frac{\rho\mu^2}{9\epsilon_0 k_\mathrm{B}}, \tag{2.29}$$

that defines a critical temperature T_c at which the dielectric response would diverge. Near T_c, the polarization becomes so large, meaning extremely large local electric fields, that the dipoles would align to one another even in case of $E \sim 0$ (analogous to a permanent magnet!). This problem and limitations were spotted and criticized by Onsager. * Onsager derived a more strict model by noting that for dipolar molecules the local electric field differs from the average electric field that results from the polarization of all molecules in the medium.

2.3.2 Onsager equation of dielectrics

Onsager described the dielectric response as the contribution of polar molecules contained in spherical cavities with radius a, in which the sum of all the spheres equals to the volume of the material.[92,93] He started by computing the electric field in a spherical cavity resulting from the applied field in the dielectric medium surrounding the cavity, and the electric field resulting from the back reaction of the medium on the dipole moment of the molecule in the cavity.

*Onsager submitted a paper with a criticism of Debye's theory to *Physikalische Zeitschrift* at which Debye was the editor by the time. It got rejected.[91]

Within this model, the internal field acting on a given dipole consist of two contributions: (i) the cavity field generated which is parallel to the external field, and (ii) the reaction field resulting from the back reaction of the surrounding medium to the dipole in the cavity. Under the influence of these two fields, the confined dipole will be polarized so that its instantaneous dipole moment differs from its permanent dipole moment $\vec{\mu}$.[94]

Onsager was able to establish the following relation between dielectric constant, polarizability and vacuum dipole moment:

$$\frac{(\epsilon_s - \epsilon_\infty)(2\epsilon_s + \epsilon_\infty)}{\epsilon_s(\epsilon_\infty + 2)^2} = \frac{\rho\mu^2}{9\epsilon_0 k_B T}, \tag{2.30}$$

which does not contain singularities, in contrast to Debye's description. This equation offers a better description for the dielectric constant of polar liquids.[44,45,94]

2.3.3 Kirkwood-Fröhlich equation of dielectrics

In the approaches of Debye and Onsager, the dielectric response has been established based on a continuum description of the dielectric medium, but the effect of intermolecular interactions has been neglected. Aqueous systems, which are of our interest, tend to behave in a cooperative manner. Kirkwood and later Fröhlich performed a rigorous statistical study of the intermolecular interactions to extend the Onsager equation of dielectrics.[93,95,96] They derived the following expression

$$\frac{(\epsilon_s - \epsilon_\infty)(2\epsilon_s + \epsilon_\infty)}{\epsilon_s(\epsilon_\infty + 2)^2} = \frac{\rho\mu^2 g_K}{9\epsilon_0 k_B T}, \tag{2.31}$$

where $g_K = 1 + z\langle\cos\gamma\rangle$ is the Kirkwood correlation factor which is a measure of the microscopic ordering of the medium. In the latter expression for g_K, z is the solvation number and $\langle\cos\gamma\rangle$ is the average orientation between two neighbouring dipoles. Notice that in the limit $g_K = 1$, which corresponds to a completely uncorrelated orientation of the dipoles, Eq. 2.31 reproduces the expression of Onsager. In case that dipoles cooperate in a parallel manner $g_K > 1$, while $g_K < 1$ means that neighbouring dipoles have an antiparallel character. For liquid water a Kirkwood correlation factor of 2.7 has been observed.[44] Then, it is clear that the structure of water increases the dielectric response with respect to an uncorrelated orientation.

2.4 Dielectric relaxation

The previous section has discussed the microscopic picture of polarization, under the assumption of static electric fields. The following question concerns to the dynamic permittivity in oscillating electric fields.

Let us start with a dielectric medium in its static $\vec{P}_{\mu,0}$ state, if the electric field is switched off, the polarization vector will decay due to thermal motions. The simplest assumption is to assume that the polarization decay follows a first-order differential equation as

$$\frac{d\hat{\vec{P}}_{\mu}(t)}{dt} = -\frac{\hat{\vec{P}}_{\mu}(t)}{\tau_{\mathrm{D}}}. \tag{2.32}$$

To determine the dielectric spectrum, we use the Fourier transformation to express the polarization in the frequency domain, therefore Eq. 2.32 yields

$$\hat{\vec{P}}_{\mu}(\omega) = \frac{\vec{P}_{\mu,0}}{1 + i\omega\tau_{\mathrm{D}}}, \tag{2.33}$$

which combined with Eq. 2.19 leads to

$$\hat{\epsilon}(\omega) = \epsilon_{\infty} + \frac{\epsilon_{\mathrm{s}} - \epsilon_{\infty}}{1 + i\omega\tau_{\mathrm{D}}}. \tag{2.34}$$

The preceding equation is the well-know Debye dielectric relaxation mode,[87,97] which assumes that all the microscopic dipoles respond with a single relaxation time τ_{D}. In Eq. 2.34, $A_{\mathrm{D}} = \epsilon_{\mathrm{s}} - \epsilon_{\infty}$ determines the strength of the Debye relaxation mode. As shown in Figure 2.1, the dielectric loss is maximum when the frequency of the external electric field matches the Debye relaxation time.

The Debye model considers a single-exponential relaxation which provides a good description of the relaxation mechanism of pure solvents, such as water.[27,44] However, systems in which the neat structure is perturbed, the relaxation process can comprise a rather broader distribution of relaxation times. Nonetheless, the analytical approach is difficult, a series of empirical models have been offered to account for such deviations. The most general approach to account for this distribution is the Havriliak-Negami equation[98]

$$\hat{\epsilon}(\omega) = \epsilon_{\infty} + \frac{\epsilon_{\mathrm{s}} - \epsilon_{\infty}}{\left[1 + (i\omega\tau_{\mathrm{D}})^{1-\alpha}\right]^{\beta}}, \tag{2.35}$$

in which the empirical parameters α and β account for symmetrical and asymmetrical spectral broadening, respectively. When $\beta = 1$ the equation reduces to the so-called Cole-Cole relaxation mode,[99,100] which has been shown to be a good approach to model the relaxation process in electrolyte solutions.[19,36,45,101,102] If $\alpha = 0$ and $\beta = 1$, Eq. 2.35 recovers the mono-exponential Debye relaxation process. The upper panel in Figure 2.1 shows the contrast between the Cole-Cole mode and the Debye mode.

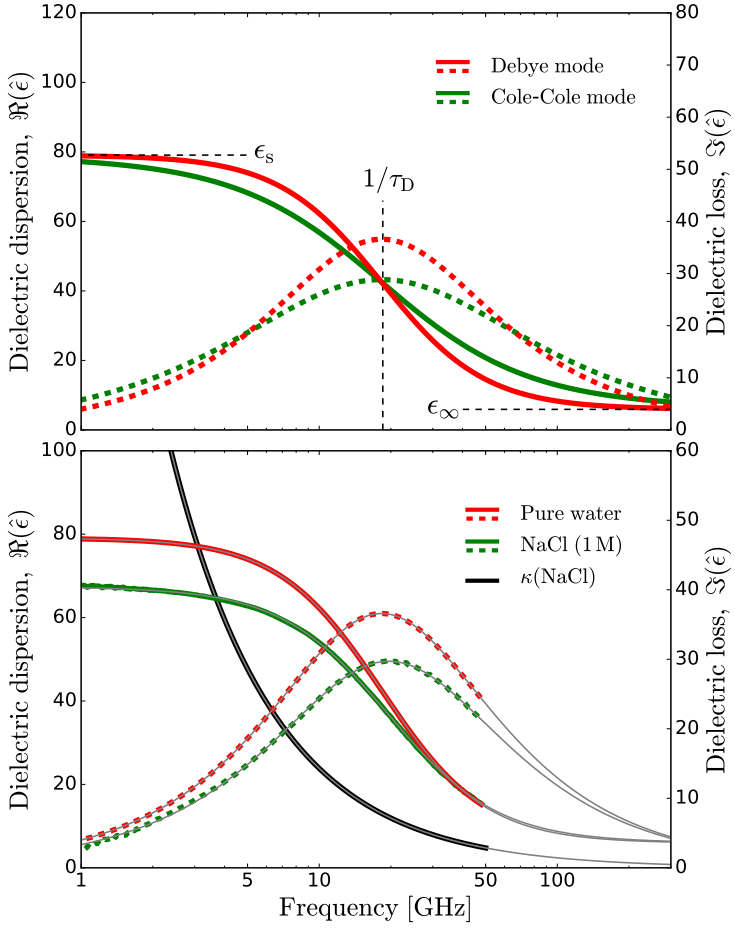

Figure 2.1. The **upper panel** shows the band shapes of the Debye relaxation mode and the Cole-Cole relaxation mode. In both cases $A_D = 80$, $\epsilon_\infty = 6$ and $\tau_D = 8.7$ ps which corresponds to the dielectric properties of pure water at 23^{o}C,[44,85] while the Cole-Cole deviates from the Debye band by $\alpha = 0.15$. Solid lines represent the dielectric dispersion, and dashed lines the dielectric loss. The **lower panel** displays dielectric spectra for pure water and a 1 M NaCl:H_2O solution. The corresponding dielectric loss of the alkaline solution has been corrected for the ionic conductivity, which is shown in black. From the dielectric constant at low frequencies, it is clear that the amplitude of the polarization is reduced in the presence of ions, an effect called depolarization. The solid grey curves result from fits using the Debye and the Cole-Cole modes for pure water and the alkaline solution, respectively.

For a conducting material, such as electrolyte solutions, the macroscopic dielectric response is modeled with the following generalized permittivity

$$\hat{\eta}(\omega) = \epsilon_\infty + \frac{\epsilon_s - \epsilon_\infty}{1 + (i\omega\tau_D)^{1-\alpha}} - \frac{i\sigma}{\epsilon_0\omega}, \tag{2.36}$$

which has shown to be sufficient to model the dielectric spectra reported in this thesis. The lower panel in Figure 2.1 displays dielectric spectra for pure water and a 1 M NaCl:H_2O solution both at 23^{o}C. The Debye mode is well suited to fit the spectra of pure water, while the electrolyte solution is fitted using a Cole-Cole mode showing a broadening of $\alpha = 0.02$. Therefore, the presence of ions induce a relaxation distribution that differs from the single exponential decays.

Moreover, in many systems the dielectric response rises from the contribution of multiple dipolar species, as in aqueous taurine solutions where taurine molecules also align with the electric field,[103] or the discrete dynamics of water in tetramethylurea solutions.[54] In these cases the dielectric spectrum can be model as the sum of n independent relaxation processes.

2.5 Depolarization

In electrolyte solutions, ion generate strong local electric fields, orienting the dipoles of neighbouring water molecules. These interactions induce local ordering and reduce (locally) the degrees of orientational freedom of the water, an effect generally called depolarization. This effect reduces the absolute magnitude of the dielectric constant (static permittivity), as is shown in the lower panel of Figure 2.1. This depolarization can be described by the sum of three contributions:

- Dilution of the solvent: having a finite size, the excluded volume of ions leads to reduction in the density of water molecules with respect to the pure solvent.[92,93,104] The amplitude of this effect is given by

$$A_{D,n}(c) = \frac{c_w(c)}{c_{w,0}} A_{D,0} \tag{2.37}$$

  where $c_{w,0}$ and $A_{D,0}$ are the molecular concentration and the amplitude of the Debye relaxation mode of pure water, and c is the ion concentration. The amplitude of the Debye relaxation mode $A_{D,n}(c)$ scales linearly with the density of water molecules, which is consistent with the Onsager model of Eq. 2.31 since the dielectric response of water is dominated by the reorientation of the dipoles, leading to the approximation that $2\epsilon_s + \epsilon_\infty \approx 2\epsilon_s$. As a result, the dielectric response $\epsilon_s - \epsilon_\infty$ of Eq. 2.31 is directly proportional to the density. Eq. 2.37 assumes that the dilution does not lead to a change of the Kirkwood correlation factor g_K of the remaining water in the solution.

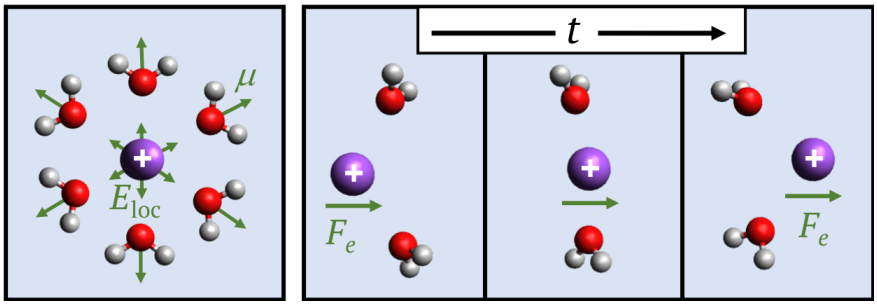

Figure 2.2. Left panel: Static depolarization induces strong binding of water molecules leading to hydration shells. **Right panel:** Kinetic depolarization rises due to the rotational response of water molecules to the translational motion of ions. Here, μ is the permanent dipole moment of a water molecule, E_{loc} the ionic electric field, and F_e is the driving force that an ion experiences in the presence of a external electric field. The figures are exaggerated representations for conceptual purposes.

- Static depolarization: the strong ionic field induces local ordering in solvation shells, locking the orientational motion of solvating water molecules[105,106] (see Figure 2.2). Static depolarization $\Delta A_{\text{D,sta}}$ is linked to ionic hydration numbers[27] as follows

$$Z_{\text{hyd}} = \frac{c_{w,0}}{A_{\text{D},0}} \frac{\Delta A_{\text{D,sta}}(c)}{c}. \tag{2.38}$$

  One should take the nature of hydration around cations and anions into account. Static depolarization is generally attributed to cations because they constrain the degrees of orientational freedom of water much more than anions (see Figure 2.3). As such, the relative contribution of the anions to the static depolarization is negligible.[18,45,51,105–108]

- Kinetic depolarization: the long-range orientational response of water molecules to moving ions. An ion moving along the direction of the external electric field causes an opposite orientation of the solvent dipoles as compared to that caused by the external electric field.[109–114]

The amplitude of depolarization has been widely used to investigate local structuring in solvation shells. However, the static and kinetic contributions are difficult to separate experimentally.[19] Over the last five decades the common approach was to compute the amplitude of kinetic depolarization from theoretical predictions. Hence, the difference between the experimentally obtained depolarization (corrected for dilution) and the value obtained theoretically was assigned to static depolarization, which was used to estimate hydration numbers.[27,34,36,45–47,115,116]

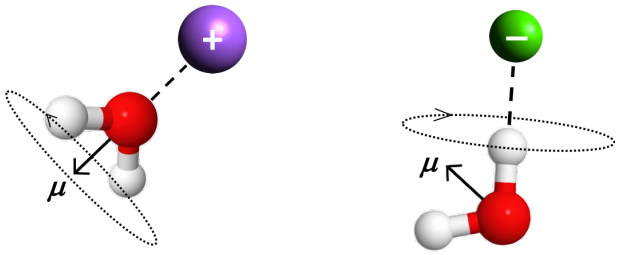

Figure 2.3. Static binding in the ionic vicinity. Water molecules hydrating cations are bounded along their dipole symmetrical axis, leading to a negligible orientation motion of the dipole. Hence, water molecules hydrating cations are assumed frozen with respect to the macroscopic dielectric response. On the other hand, water molecules in the anionic vicinity bond along the direction of one of their hydroxyl groups, providing still degrees of rotational motion to the permanent dipole moments.

The Hubbard-Onsager continuum model for dielectric deficiency[109–111] has been widely used to estimate the magnitude of kinetic depolarization.[27,34,36,45–47,102,115–118] This model assumes that the ions are immersed in a continuum environment with uniform dielectric behavior as that in pure water. Within this model, it is also assumed that the viscous friction is much larger than the dielectric drag that the orientating dipoles could cause on the ions. Based on these assumptions, the following expression for kinetic depolarization is obtained:

$$\Delta A_{\mathrm{D,kin}}(c) = p\sigma(c)\left(\frac{\tau_{\mathrm{D}}}{\epsilon_0}\cdot\frac{\epsilon_{\mathrm{s}}-\epsilon_{\infty}}{\epsilon_{\mathrm{s}}}\right), \tag{2.39}$$

where the values between the parenthesis are the dielectric properties of the pure solvent. This equation implies that twater molecules would react to the field of moving ions via a dielectric relaxation mechanism that is the same as the macroscopic dielectric relaxation.

Hence, changes in the amplitude of kinetic depolarization depend only on the concentration-dependent ionic conductivity $\sigma(c)$, and the factor p that characterizes the frictional forces at the ionic surface. Hubbard and Onsager also derived the values for the p-factor, with limiting cases of $p = 1$ for a infinite frictional force at the ionic surface (stick) and $p = 2/3$ for a negligible friction on the ionic surface (slip).

It is clear that this model does not account for the ion specificity. In fact, the model implicitly assumes that water preserves the same local structure and ordering regardless the presence of ions, meaning that the cooperative molecular behavior is unperturbed in solvation shells (see Section 2.3.3). However, this assumption is contradictory to the notion of ions as structure breakers and structure

makers, which have been determined from experiments and simulations.[14,40] This discrepancy is addressed in Chapter 4.

2.6 Experiment realization

Dielectric relaxation spectroscopy enables us to measure the induced complex polarization of a sample in the frequency domain, which in consequence provides the characteristic complex permittivity $\hat{\epsilon}(\omega)$. Vector network analyzers (VNA) are a novel tool to study dielectric properties due to their capacity to measure simultaneously the phase and amplitude of electromagnetic waves in a wide range of frequencies. The used experimental setup is based on a vector network analyzer (Rhode-Schwartz ZVA67) operating at frequencies up to 67 GHz in combination with a open-ended coaxial probe cell. The VNA and the probe cell are connected with a phase-stable coaxial cable (Rhode-Schwartz ZV-Z96). The reflectrometric sample cell is held between two metal blocks that can be set at a desired temperature with a water-flow loop using a thermoelectric chiller (ThermoTek T257P-20) with a temperature stability of 0.1^oC.

We perform one-port reflection measurements in which the liquid sample is in contact with the probe head. The reflectrometric disc cell is built based on the probe geometry previously proposed by Blackham et al.[119] The data are recorded in the frequency range of 1–50 GHz, which encompasses the main relaxation mode of water centered at 18 GHz.[85]

In this one-port experimental configuration, we applied an initial signal $\hat{a}(\omega)$ to the sample and detect the reflected signal $\hat{b}(\omega)$. These signals are linked via the complex scattering parameter $\hat{S}_r(\omega)$ with the following relation

$$\hat{b}(\omega) = \hat{S}_r(\omega) \cdot \hat{a}(\omega). \tag{2.40}$$

where $\hat{S}_r$ is related to the dielectric properties of the sample.

In the open-ended probe geometry, the signal is determined by the transition from the impedance of the coaxial probe $\hat{Z}_c$ to the impedance of the sample $\hat{Z}_p$. The complex scattering parameter is related to the normalized impedance $\hat{Y} = \hat{Z}_p/\hat{Z}_c$ via

$$\hat{S}_r(\omega) = \frac{1 - \hat{Y}(\omega)}{1 + \hat{Y}(\omega)}. \tag{2.41}$$

For the geometry of the open-ended reflectrometric sample cell, the permittivity-to-impedance relation is given by[119]

$$\hat{Y} = \frac{-\hat{k}_s^2}{\pi \hat{k}_c^2 \ln(D/d)} \sum_{n=0}^{\infty} \frac{(-i)^n \hat{k}_s^n I_{n+1}}{n!} \tag{2.42}$$

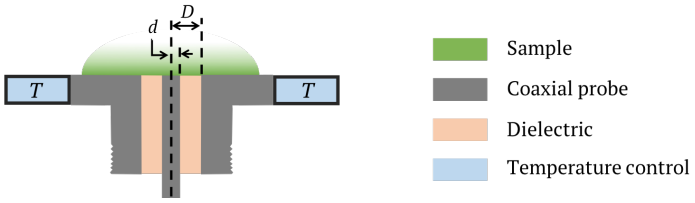

Figure 2.4. Transversal cut of the open-ended probe head. The ratio of the incident and the reflected signals at the sample-probe head determines the complex scattering parameter $\hat{S}_r$. The coaxial cable, mentioned in the main text, connects underneath the probe sample cell.

where D and d are the radii of the inner and outer conductors of the coaxial probe, $\hat{k}_c(\omega) = \omega\sqrt{\epsilon_c\epsilon_0\mu_0}$ is the wavevector of the electric field within the coaxial probe, and $\hat{k}_s(\omega) = \omega\sqrt{\hat{\epsilon}_s\epsilon_0\mu_0}$ is the wavevector of the electric field in the sample with complex permittivity $\hat{\epsilon}(\omega)$. The coefficients I_n are given by

$$I_n = \int_d^D \int_d^D \int_0^\pi R^{n-2}\cos(\phi)d\phi dr dr' \qquad \text{with} \qquad R^2 = r^2 + r'^2 - 2rr'\cos(\phi) \tag{2.43}$$

As has been discussed in the original literature for the open-ended sample cell,[119] the I_n coefficients can be calculated theoretically, but they must be optimized empirically due to the presence of higher order modes of the electric field, which are not included in the derivation of Eq. 2.42. The first 40 optimized coefficients I_n have been taken from Johannes Hunger's PhD dissertation,[120] as have been used for the study of multiple aqueous samples.[19,34,36,53,54,103]

Since the sample is located at a certain distance away from the instrument and the setup consist of multiple components, the setup has to be calibrated prior to the measurements. To avoid systematic errors due to imperfections in the electrical network (non-ideal coaxial line), the measured scattering parameter $\hat{S}_{r,m}$ must be corrected to the actual scattering parameter $\hat{S}_{r,a}$ at the probe head according to

$$\hat{S}_{r,m} = \hat{\epsilon}_\lambda + \frac{\hat{\epsilon}_\nu \hat{S}_{r,a}}{1 - \hat{\epsilon}_\sigma \hat{S}_{r,a}}, \tag{2.44}$$

where $\hat{\epsilon}_\lambda$ accounts for the directional imperfections of the coupling elements, the frequency response $\hat{\epsilon}_\nu$ accounts for changes in the phase that may occur along the finite length of the network, and source match $\hat{\epsilon}_\sigma$ accounts for an impedance mismatch between the the VNA port and the coaxial cable that would lead to re-reflections back to the probe head.

The setup is calibrated by a two-consecutive calibration procedure using three standard references in each step, according to Eq. 2.44. First, the VNA-coaxial

cable interface is calibrated via the built-in full-one-port calibration routine using the open, short and match plugs from the ZV-Z218 calibration kit. Second, the interface between the coaxial cable and the sample cell head is calibrated using air (open), conductive silver paint (short) and pure water (match). In all the dielectric relaxation measurements reported in this thesis we employed this calibration routine.

2.7 Data analysis and modeling

Since Eq. 2.42 has no analytical solution, the complex permittivity is computed numerically via a minimization routine using "Python" and the libraries "Numpy" and "Scipy". These scripts are very extensive to be shown in this thesis, but available at https://github.com/RobertoCota/Dielectric-relaxation-spectroscopy.

The dielectric properties of the solutions studied in this thesis are obtained by means of least-square minimization routines by which the the models discussed in Section 2.4 are fitted to the measured dielectric spectra. While the dielectric responses of pure solvents were fitted using a single Debye relaxation mode, the spectra of electrolyte solutions are well described by the sum of a Cole-Cole relaxation mode and a ionic-conductivity term, as expressed in Eq. 2.36. In the lower panel of Figure 2.1, the superposed grey lines display the results that best reproduce the experimental data.

The minimization routine used to determine dielectric properties of electrolyte solutions (as the 1 M NaCl:H_2O in Figure 2.1) is shown in Listing 2.1.

```
1
2  # -*- coding: utf-8 -*-
3
4  import numpy as np
5  from scipy.optimize import leastsq
6
7  eps0 = 8.8541878176e-12 #Permittivity of free space
8
9  #Cole-Cole relaxation mode plus ionic conductivity term
10 def ColeCon(x, AD, tau, alfa, kappa):
11     CC = 5.915 + (AD)/(1 + ((1j*(2*np.pi)*(tau)*(x))**(1 - alfa)
       ))
12     Con = (kappa)/(2*np.pi*(eps0)*(x))*1j
13     return CC - Con
14
15 #Residual function
16 def Residual(P,f,epsR,epsI):
17     ResR = epsR - ColeCon(f, *P).real
18     ResI = epsI - ColeCon(f, *P).imag
19     return np.sqrt(np.power(ResR, 2) + np.power(ResI, 2))
20
21 #Importing raw permittivity
22 Freq, epsRaw_Real, epsRaw_Imag = np.loadtxt('File_Name', unpack=
       True)
23
24 #Initial values
25 p0=[65.0, 8.7e-12, 0.01, 7.0]
26
27 #Least-square minimization
28 ParOpt, CovOpt, info, errmsg, ier = leastsq(Residual, p0, args=(
       Freq, epsRaw_Real, epsRaw_Imag), full_output=1)
29
30 ### ParOpt: optimized parameters
31 ### CovOpt: optimized covariance matrix
```

Listing 2.1. Generalized Python script for global analysis in which the real and imaginary components of the complex permittivity are optimized simultaneously.

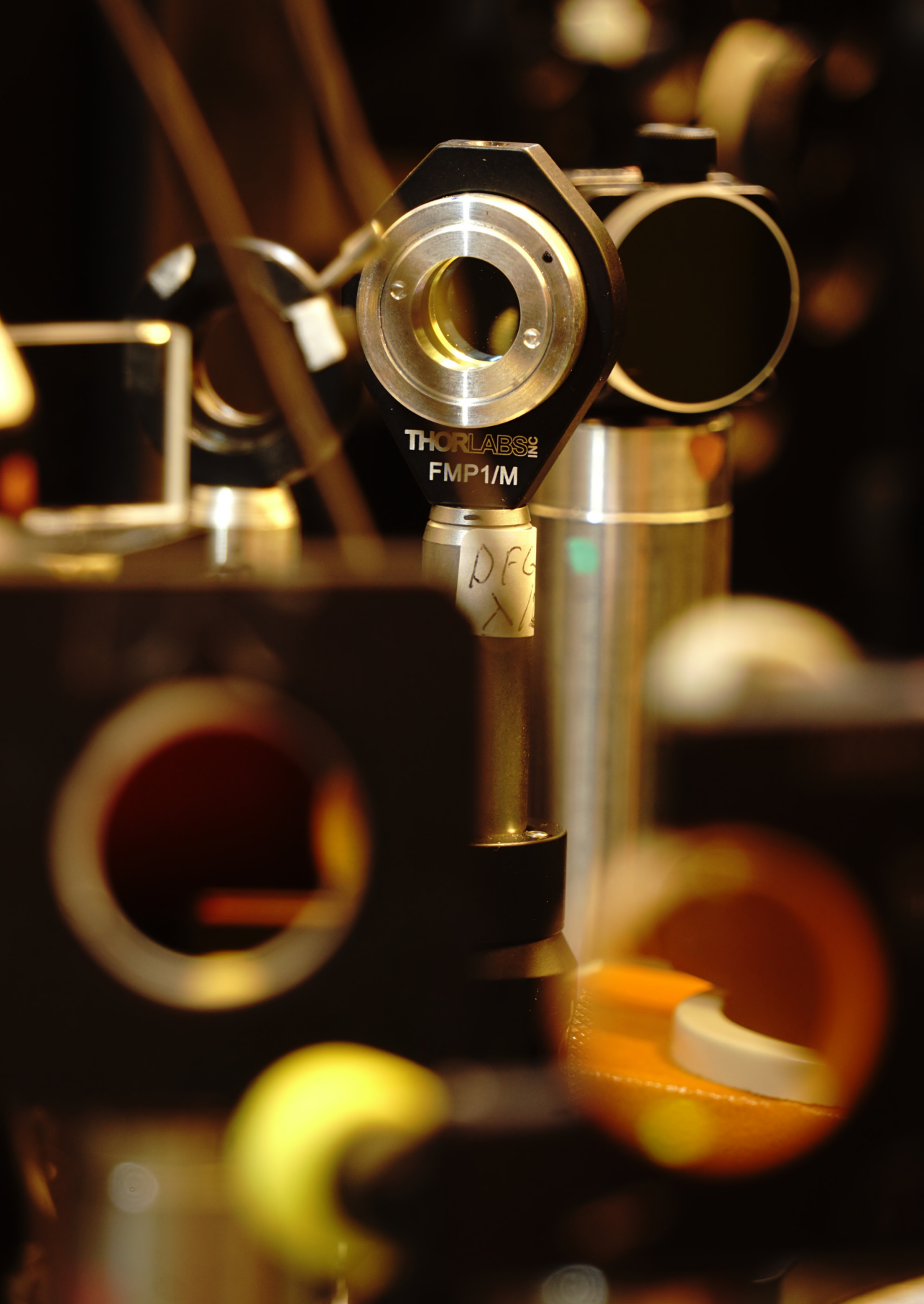
THORLABS
FMP1/M

◀ *A ZnSe window (the close field orange element in the bottom right) splits our laser pulses into a pump and a probe beam. A halfwave plate (at the focus of the image) enables us to change the polarization of our pump pulses. These two elements set the basis of polarization-resolved pump-probe spectroscopy, leading to a suitable method to observe molecular reorientation.*

3
Methods II
Vibrational spectroscopy

In this chapter we discuss the theoretical background and experimental methodology used to study aqueous solutions by means of vibrational spectroscopy. In particular, we discuss the aspects that allow light to couple with molecular oscillators and to induce vibrational transitions. By targeting specific vibrational modes, we can then determine the connection between the observable macroscopic properties, such as absorption, and the underlying microscopic structure and dynamics.

3.1 The classical harmonic oscillator

The simplest description of molecular vibrations starts from the classical approach of a diatomic molecule with masses m and M (with $M \gg m$). The two atoms are connected by a covalent chemical bond that acts as a spring, as shown in Figure 3.1A. If m experiences a small displacement with respect to its equilibrium position x_0 (i.e. the equilibrium bond length), the spring exerts a restoring force that follows Hooke's law with a spring constant k. Newton's second law states

$$m\frac{d^2x}{dt^2} + kx = 0, \tag{3.1}$$

with the solution

$$x(t) = x_0 \cos(\omega_0 t), \tag{3.2}$$

where $\omega_0 = \sqrt{k/m}$ is the frequency at which m oscillates harmonically around its equilibrium position. The preceding equation describes the periodic displacement of m bound to a much heavier atom.

Most molecules consist of more than two atoms. The intramolecular interactions are described as springs pairing all the atoms within the molecule (Fig. 3.1B). This means that the position of a given atom can be affected by multiple bonds, leading to more complex dynamics as compared to the previous example. For a molecule composed of N atoms the equations of motion can be written as

$$M\frac{d^2X}{dt^2} + KX = 0, \tag{3.3}$$

with X a $3N$-element vector that describes the position of all masses in the three-dimensional space, and M and K matrices ($3N \times 3N$) that contain the corresponding masses m_i and spring constants k_{ji}.

Equation 3.3 constitutes a set of coupled differential equations, which can be solved by a linear transformation to compute the eigenfrequencies of each oscillator in the molecule. We define a unitary matrix U such that

$$(M^{-1}K)U = U\Omega, \tag{3.4}$$

where Ω is a diagonal matrix that contains the eigenfrequencies ω_i. The unitary matrix can also operate on X to define a new vector as $Q = U^{-1}X$. Hence, Eq. 3.3 can be diagonalized, and leads to the equation

$$\frac{d^2Q}{dt^2} + \Omega Q = 0, \tag{3.5}$$

that provides a set of $3N$ uncoupled differential equations. Hence, the oscillating

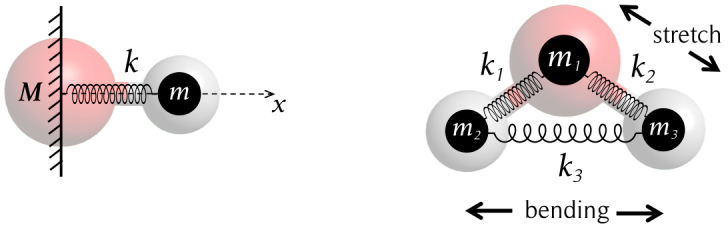

Figure 3.1. Left: Covalent chemical bonds can be modeled as harmonic oscillators. **Right:** Representation of a polyatomic molecule (water) with respect of its different degrees of vibrational freedom.

dynamics of atoms within the molecule are described by superposition of independent harmonic oscillators q_i, conventionally called "normal modes".

Water molecules are formed by three atoms with two non-parallel covalent bonds, so water has three normal modes (see Fig. 3.1B): a bending mode, and two OH stretches that combine to give the symmetric and antisymmetric stretch modes.[56,121,122]

3.2 Quantum description and vibrational transitions

In the quantum mechanical description of molecular vibrations, we again describe chemical bonds as harmonic oscillators, leading to the following Hamiltonian:

$$\hat{H}_0 = \frac{\hat{p}^2}{2m} + \frac{1}{2}k\hat{x}^2, \tag{3.6}$$

where $\hat{p}$ $(= -i\hbar\partial_x)$ and $\hat{x}$ are the momentum and position operators. The first term represents the kinetic energy of the system, while the second corresponds to the potential energy of a particle in a Hooke's law-type potential.

Solving the time-independent Schrödinger equation $\hat{H}_0 |\Psi\rangle = E |\Psi\rangle$ yields a family of solutions defined by the following orthogonal eigenstates

$$|\psi_n(x)\rangle = \frac{1}{\sqrt{2^n n!}} \cdot \left(\frac{m\omega_0}{\pi\hbar}\right)^{1/4} \cdot \exp\left(-\frac{m\omega_0 x^2}{2\hbar}\right) \cdot H_n\left(\sqrt{\frac{m\omega_0}{\hbar}}x\right), \tag{3.7}$$

with $|\psi_n\rangle$ the stationary wavefunctions that obey the relation $\langle\psi_n|\psi_m\rangle = \delta_{nm}$, with δ_{nm} the Kronecker delta, and H_n the Hermite polynomials. The corresponding

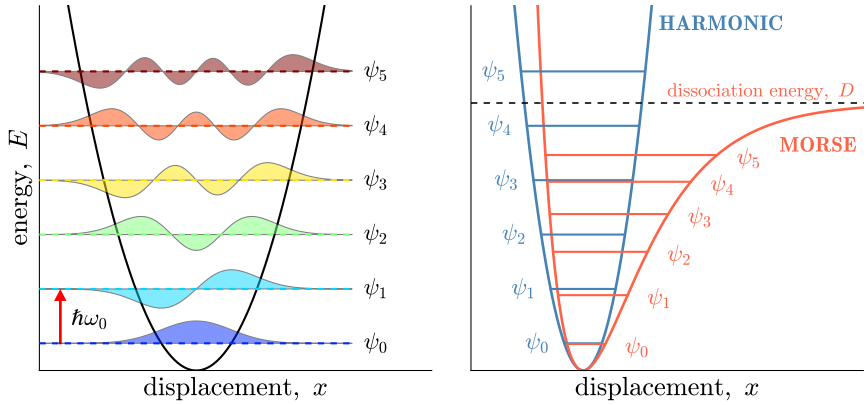

Figure 3.2. Left: Wavefunctions described in a harmonic oscillator potential. Each wavefunction is drawn at its corresponding energy level. Consecutive level are equidistant by a quanta of energy $\hbar\omega_0$. **Right:** Comparison between the harmonic oscillator potential and anharmonic vibrations described by the Morse potential. Notice that the latter has a asymptotic behavior at large distances, which corresponds to the dissociation energy level. In the Morse potential, the space between consecutive energy levels decreases with increasing the quantum number n.

eigenenergies are given by

$$E_n = \hbar\omega_0 \left(n + \frac{1}{2}\right), \qquad \text{with} \qquad n \in \mathbb{N}_0. \tag{3.8}$$

The value n corresponds to the vibrational quantum number, and $\omega_0 = \sqrt{k/m}$. Eqs. 3.7 and 3.8 state that the energy is quantized and the system can only be in discrete states, referred to as zeroth, first, second and higher order vibrational states, shown in the left panel of Fig. 3.2. From Eq. 3.8, it is clear that the energy of the ground state ($n = 0$) is not zero, but $E_0 = \hbar\omega_0/2$ which is called the zero-point energy. Subsequent states are equidistantly separated by a quantum of energy $\hbar\omega_0$.

In the quantum description, transitions between levels can occur as the result of a time-dependent perturbation, such as light (electromagnetic waves). As shown in Eq. 2.20, an electromagnetic wave interacts with the charges in the system, adding a new term to the Hamiltonian:

$$\hat{H} = \hat{H}_0 + \hat{V}_{\text{int}}(t), \qquad \text{with} \qquad \hat{V}_{\text{int}}(t) = \hat{\vec{\mu}} \cdot \vec{E}(t), \tag{3.9}$$

where $\vec{E}(t)$ refers to the electric field of the light and the dipole moment operator $\hat{\vec{\mu}}$ defines the distribution of charges q in the system following $\hat{\vec{\mu}} = \sum_i q_i \hat{\vec{x}}_i$.

A transition from a vibrational level to another can be described using the time-dependent Schrödinger equation

$$\hat{H}(t)\,|\Psi\rangle = i\hbar\frac{\partial}{\partial t}\,|\Psi\rangle\,, \tag{3.10}$$

which can be solved by separation of variables. Using the expressions given by Eqs. 3.7 and 3.8, the general solution to Eq. 3.10 is written as

$$|\Psi\rangle = \sum_n c_n(t)e^{-iE_nt/\hbar}\,|\psi_n\rangle \tag{3.11}$$

where $c_n(t)$ is the corresponding amplitude of each energy level at time t.

Using Eqs. 3.9, 3.10 and 3.11, the time-dependent amplitude of a given $|\psi_m\rangle$ state can be computed as follows

$$\frac{d}{dt}c_m(t) = \frac{1}{i\hbar}\sum_n c_n(t)\,\langle\psi_m|\,\hat{V}_{\text{int}}\,|\psi_n\rangle\,e^{-i\omega_{nm}t}, \tag{3.12}$$

where $\omega_{nm} = (E_n - E_m)/\hbar = -\omega_{mn}$ is the energy difference between the states n and m. The preceding equation provides a full description of the population of the state m, although not practical because each unknown coefficient c_m is determined by the whole set of c_n coefficients. Assuming that the system is entirely in a single state k at $t = 0$ and the initial state is negligibly perturbed over the time, meaning $c_k(0) = 1$ and $c_k(t) \simeq 1$, Eq. 3.12 reduces to[123]

$$c_m(t) \simeq \frac{1}{i\hbar}\int_0^t \langle\psi_m|\,\hat{V}_{\text{int}}(t')\,|\psi_k\rangle\,e^{-i\omega_{km}t'}. \tag{3.13}$$

The simplest description of such perturbation is to assume a harmonically oscillating electric field (harmonic perturbation) as $\vec{E} = \vec{E}_0[\exp(i\omega t) + \exp(-i\omega t)]$. In that case, the transition rate $\Gamma_{k\to m}$, that is defined as the time derivative of the square modulus of c_m, is given by

$$\begin{aligned}\Gamma_{k\to m} \simeq \frac{d}{dt}|c_m|^2 &= \frac{2\pi}{\hbar^2}|\,\langle\psi_m|\,\hat{\vec{\mu}}\cdot\vec{E}_0\,|\psi_k\rangle\,|^2\delta(\omega\pm\omega_{km}),\\ &= \frac{2\pi}{\hbar^2}E_0^2\cos^2(\theta)|\,\langle\psi_m|\,\hat{\mu}\,|\psi_k\rangle\,|^2\delta(\omega\pm\omega_{km}),\end{aligned} \tag{3.14}$$

which is the so-called Fermi's golden rule, where θ defines the angle between the dipole moment and the polarization of the perturbing electric field. The expression $\mu_{mk} = \langle\psi_m|\,\hat{\mu}\,|\psi_k\rangle$ is generally called transition dipole moment. In the last expression, the dipole operator $\hat{\mu}$ refers to the entire distribution of charges, which encompasses transition dipoles of any kind. In the case of vibrational transitions, the transition dipole operator can be written in terms of the oscillation coordinate

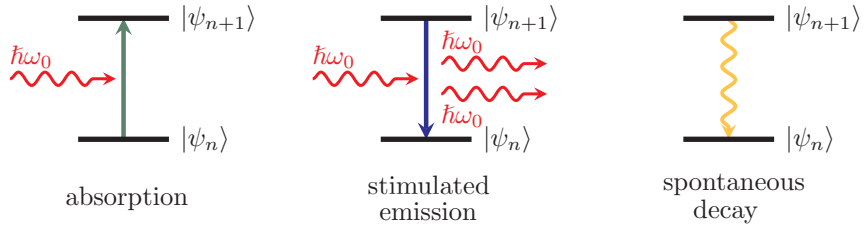

Figure 3.3. Illustration for three different transition processes: absorption, stimulated emission and spontaneous decay. The illustration pictures the ideal case in which the energy of the photon matches the energy difference between two consecutive states.

x and the equilibrium position x_0 by the following expansion

$$\hat{\mu} = \mu_0 + \frac{d\mu}{dx}(\hat{x} - x_0) + \cdots \tag{3.15}$$

which leads to

$$\Gamma_{k\to m} = \frac{2\pi}{\hbar^2} E_0^2 \cos^2(\theta) \left(\frac{d\mu}{dx}\right)^2 |\langle\psi_m|\,\hat{x}\,|\psi_k\rangle|^2 \delta(\omega \pm \omega_{km}). \tag{3.16}$$

This equation has the following physical interpretation:

- The $\delta(\omega \pm \omega_{km})$ term represents the conservation of energy in the transition $|\psi_k\rangle \to |\psi_m\rangle$. We see that such condition can only be satisfied either by energy taken away from the external electric field (absorption if $E_m \simeq E_k + \hbar\omega$) or by energy given out to the external electric field (stimulated emission if $E_m \simeq E_k - \hbar\omega$). In both cases, such transition takes place when ω matches the energy difference between the states m and k (see Fig. 3.3).
- The $\langle\psi_m|\,\hat{x}\,|\psi_k\rangle$ term establishes the transition selection rule since it is zero unless $m = k \pm 1$, meaning that transitions only occur between consecutive states.[123]
- The $d\mu/dx$ term implies that the external electric field only couples to those vibrations that induce changes in the dipole moment.
- From the term $\cos^2(\theta)$, we observe that the probability of a $|\psi_k\rangle \to |\psi_m\rangle$ transition to occur depends on the angle between the transition dipole moment and the polarization of the external electric field. This probability is maximal at $\theta = 0$, which means $\vec{\mu} \parallel \vec{E}_0$. This is the basis of polarization-resolved spectroscopy which we will discuss later.

In real molecules, the potential cannot be quadratic due to molecular dissociation at large interatomic distances.[124] A more adequate potential to include the effect of molecular dissociation is given by

$$V_{\mathrm{M}}(x) = D\left(1 - e^{-ax}\right)^2, \tag{3.17}$$

the so-called Morse potential,[125] shown in the right panel of Figure 3.2. The energy at which the bond dissociates is represented by D, and $a = \sqrt{k/2D}$ the width of the potential. By introducing Eq. 3.17 in Eq. 3.6 instead of the harmonic oscillator potential, the corresponding eigenenergies related to the Morse potential are expressed as follows

$$E_n = \hbar\omega_0\left(n + \frac{1}{2}\right) - \frac{\hbar^2\omega_0^2}{4D}\left(n + \frac{1}{2}\right)^2, \tag{3.18}$$

where n again is the vibrational quantum number and the angular frequency ω_0 ($= \sqrt{k/m}$) satisfies also the relation $\omega_0 = a\sqrt{2D/m}$. In contrast to the description of an harmonic oscillator, the energy separation between consecutive states becomes smaller with increasing the quantum number n. At low n, Eq. 3.18 can be well represented by Eq. 3.8. Further potentials have been explored to overcome some limitations of the Morse potential, such as the long-range Morse potential that captures the attractive long-range behavior in real systems.[126]

3.3 Linear absorption spectroscopy

The way in which light interacts with an absorbing medium can give information at the molecular level. As in the previous chapter, to describe the vibrational experiments we need to construct models based on the changes that an incident field (light) experiences as it propagates through a medium.

Assume a system of molecular oscillators of the same species in thermal equilibrium, meaning that the system is isotropic and in the ground state $|0\rangle$, so absorption is the most likely process to occur in the presence of light. This process will lead to attenuation of the incident field and non-zero, but relatively small, population of the first excited state $|1\rangle$.

For monochromatic light with intensity of $I_0 = c\epsilon_0|E_0|^2/2$ and frequency ω, the absorbed power associated with the $|0\rangle \rightarrow |1\rangle$ transition is written as $P_{01} = \hbar\omega\Gamma_{0\rightarrow 1}$. The absorption cross section σ_{10} is defined as the ratio between the latter expressions, and using Eq. 3.16, is given by

$$\sigma_{10}(\omega) = \frac{P_{10}(\omega)}{I_0} = \frac{\pi\omega}{3c\epsilon_0\hbar}\mu_{10}\delta(\omega \pm \omega_{10}) \tag{3.19}$$

in which $\langle cos^2\theta\rangle = 1/3$ since the material is assumed isotropic. The cross section

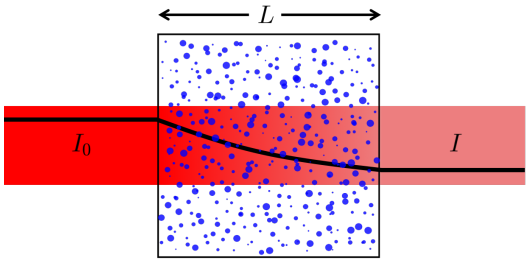

Figure 3.4. In linear absorption spectroscopy, one studies the decrement on the intensity of light as it propagates through a material. The initial and the final intensities are linked by the spectroscopic properties of the sample as described by Eqs. 3.19 and 3.21.

can be understood as an effective transverse area (not necessarily linked to the dimensions of the molecule) that the incident field must hit in order for the given transition to occur.

Assume now that a field propagates in the z direction through a material with thickness L and density of oscillators in the ground state ρ (Fig. 3.4), the Lambert-Beer law

$$dI = -\sigma_{10}(\omega)\rho I dz \tag{3.20}$$

states that the variation of intensity dI through propagation in a segment dz is equal to the product between the intensity and the cross section of the material. Integrating this expression gives

$$I = I_0 \exp[-\beta(\omega)L], \tag{3.21}$$

with $\beta(\omega) = \rho\sigma_{10}(\omega)$ the attenuation coefficient. This equation provides a link between the macroscopic transmission of the material, $T = I/I_o$, with the microscopic molecular property σ_{10}. The absorbance, which provides a more convenient and linear relation between the relevant parameters, is given by

$$\alpha(\omega) = -\ln\frac{I}{I_0} = \sigma_{10}(\omega)\rho L. \tag{3.22}$$

As can be observed from Eq. 3.19, a vibrational transition will only occur when the frequency of the electric field matches the energy difference between the excited and ground states.

In condensed-phase systems, the absorption spectrum $\alpha(\omega)$ is not a delta function as it would result from Eqs. 3.19 and 3.22, but has a finite width. This is due to two effects. First, the finite excited-state lifetime and fast fluctuations in

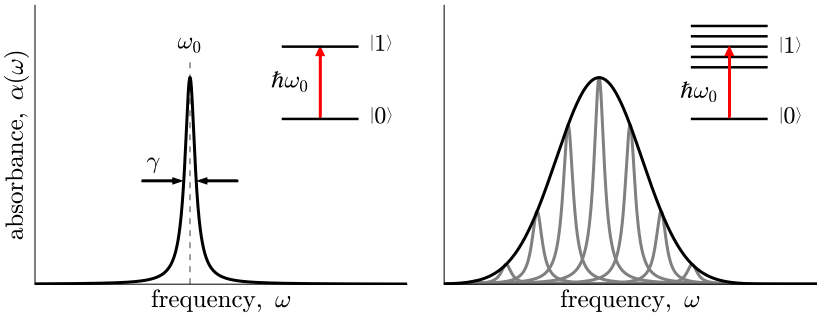

Figure 3.5. Left: homogeneous broadening due to the finite lifetime of the excited state and fast fluctuations of the resonance frequency. This effect follows a Lorentzian functional form. **Right:** the absorption lineshape is further broadened due to intermolecular interactions such as hydrogen bonding, leading to a statistical distribution of the resonance frequency.

the resonance frequency (due to interaction of the oscillator with its surroundings) give rise to so-called homogeneous broadening. This broadening occurs for each individual oscillator, and if all oscillators have the same resonance frequency ω_{10}, it typically gives rise to a Lorentzian line shape:

$$I(\omega) \propto \frac{1}{\pi} \frac{\gamma/2}{(\omega - \omega_{10})^2 + (\gamma/2)^2}, \tag{3.23}$$

where γ is the homogeneous line width (see Fig. 3.5-left). In addition, there may exist a distribution of resonance frequencies ω_{10} in the sample, so that the absorption spectrum becomes the convolution of Eq. 3.23 with this distribution of resonance frequencies (see Fig. 3.5-right). This so-called inhomogeneous broadening occurs very often in hydrogen-bonded systems, where local differences in hydrogen-bond strength give rise to a broad distribution of OH- or OD-stretch frequencies (see Chapters 7, 8 and 9).

3.4 Time-resolved vibrational spectroscopy

Pump-probe spectroscopy is a useful tool to study dynamical aspects of molecular systems. This technique is based on an intense pulse that excites a significant fraction of the oscillators contained in a sample to the excited state (pump), while a second time-delayed weak pulse monitors the equilibration mechanism of the excited oscillators (probe). The pump and probe processes are shown in Figure 3.6.

Here, we aim to provide a phenomenological understanding behind pump-probe spectroscopy. To this purpose, we start with the notion of transient absorption

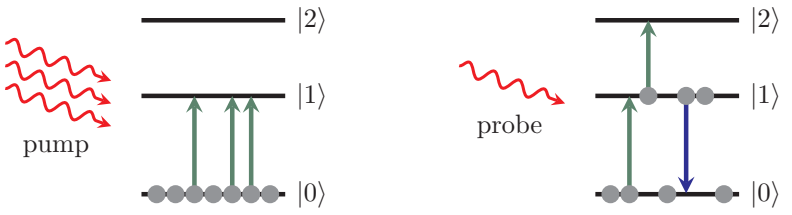

Figure 3.6. Illustration of pump-probe spectroscopy in which the first three vibrational states are considered. The gray circles represent population. **Left:** at $t = 0$, an intense pump beam promotes vibrations to the first excited state (green arrows), which are after monitored by a second beam called probe. **Right:** the probe induces three different effects: excitation from ground to the first excited state, excitation from the first to the second excited state, and stimulated emission from the first to the ground state.

which arises from the difference between the absorption of the perturbed sample and of the unperturbed sample. The system is perturbed out of its equilibrium due to te intense pump pulse. The transient absorption is defined as

$$\Delta\alpha(\omega, t) = \alpha_{\mathrm{p}}(\omega, t) - \alpha_{\mathrm{u}}(\omega), \tag{3.24}$$

where the subindices p and u refer to the pumped and the unpumped sample. As shown in Eq. 3.22, the absorbance of the unpumped sample is given by

$$\alpha_{\mathrm{u}}(\omega) = \sigma_{01}(\omega)N_0 \tag{3.25}$$

with $N_0 = \rho L$ the number of vibrational absorbers per area unit in the ground state. After excitation by the pump pulse, the prope pulse will experience a change in the absorption as the result of three different processes. First, the density of absorbers in the ground state is reduced, such that the $|0\rangle \rightarrow |1\rangle$ absorption is reduced by a factor of $(N_0 - N_1(t))/N_0$, with $N_1(t)$ the density of molecules in the excited state at any time. A second effect is stimulated emission that also manifests itself as an increase in the transmission of the sample, in other words, a reduced absorbance according to Eq. 3.22. Third, the probe pulse can promote molecules from the first to the second excited state which induces an absorption matching the $|1\rangle \rightarrow |2\rangle$ transition. These effects can be represented as follows

$$\alpha_{\mathrm{p}}(\omega, t) = \underbrace{\sigma_{10}(\omega)[N_0 - N_1(t)]}_{\substack{\text{ground state} \\ \text{depletion}}} - \underbrace{\sigma_{01}(\omega)N_1(t)}_{\substack{\text{stimulated} \\ \text{emission}}} + \underbrace{\sigma_{21}(\omega)N_1(t)}_{\substack{\text{induced} \\ \text{absorption}}}. \tag{3.26}$$

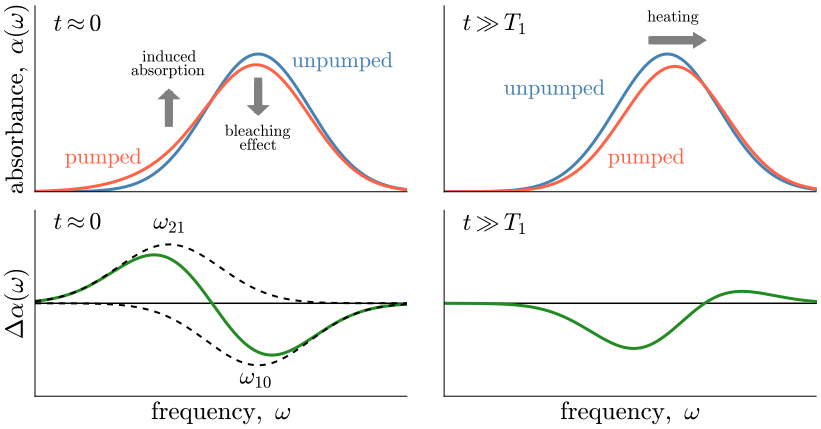

Figure 3.7. Illustration of pump-probe spectra that resemble the response of the OD stretch vibration of HDO molecules isotopically diluted in H_2O. **Left:** at short time delays the absorption is reduced around ω_{10} (bleaching), while absorption around ω_{21} is accessible. **Right:** at long time delays the absorption spectrum shifts to the blue and reduces in amplitude due to temperature increase upon vibrational relaxation.

Since $\sigma_{10} = \sigma_{01}$, the transient absorption change defined in Eq. 3.24 reduces to

$$\Delta\alpha(\omega, t) = -\underbrace{2\sigma_{10}(\omega)N_1(t)}_{\substack{\text{bleaching}\\ \text{band}}} + \underbrace{\sigma_{21}(\omega)N_1(t)}_{\substack{\text{induced}\\ \text{absorption}}}, \tag{3.27}$$

with features that are represented in the left side of Figure 3.7 (for short time delays).

In the simplest scenario, the excited molecules decay directly to the ground state, so that the bleaching and induced absorption vanish exponentially in the same fashion, such that

$$\Delta\alpha(\omega, t) = [-2\sigma_{10}(\omega) + \sigma_{21}(\omega)]N_1(0)e^{-t/T_1}, \tag{3.28}$$

with T_1 the lifetime of the vibrationally excited state. In general, the lifetime represents the equilibration rate of the excited vibration with respect to its surroundings.

In Chapter 7, we show that OD stretches hydrating hydroxide ions relax much faster (∼0.3 ps) than those in neat water with vibrational lifetime of 1.7 ps. The accelerated equilibration rate is associated to the strong hydrogen bonds in the immediate ionic vicinity. This type of dynamical variations, along with spectral differences, allow us to disentangle different spectral contributions in a way that is

not possible with linear absorption spectroscopy. This separation has been widely used to interrogate the behavior of molecules in different environments, as shown in Chapters 7, 8 and 9.

In aqueous solutions, vibrational energy relaxation may follow more complicated relaxation pathways that involve intermediate states, and in the presence of solutes, different modes that overlap spectrally may be excited simultaneously, as we will see in Chapters 7 and 8.

3.5 Polarization-resolved pump-probe spectroscopy

The assumption of having an isotropic system in thermal equilibrium holds valid, until the pumped pulse, which in our case is linearly polarized, interacts with the system. As has been discussed before, Eq. 3.16 shows that light couples primarily with transition dipole moments aligned parallel to the polarization of the electric field. In fact, this polarization-dependent absorption will induce an anisotropy in the distribution of excited oscillators that can be used to explore molecular reorientation, which is intimately linked to structural properties.

Once again, let us assume a system of molecules that show an isotropic distribution. Immediately after excitation, the normalized distribution of excited vibrations is given by

$$p(\theta, \phi, t = 0) = \frac{3}{4\pi} \cos^2(\theta) \tag{3.29}$$

with θ the polar and ϕ the azimuthal angles with respect of the pump polarization. Hence, probing the sample in polarization parallel or perpendicular to that of the pump will delivers a polarization-dependent transient absorption.

If we define our coordinate system with the pump light propagating along the x axis with its polarization along the z axis, it follows to the parallel (z-polarization) and perpendicular (y-polarization) transient signals described by

$$\Delta\alpha_{\parallel}(\omega, t) = 3\Delta\sigma(\omega) N_1(t) \int_S p(\theta, \phi, t) \cos^2(\theta) dS \tag{3.30}$$

$$\Delta\alpha_{\perp}(\omega, t) = 3\Delta\sigma(\omega) N_1(t) \int_S p(\theta, \phi, t) \sin^2(\theta) \sin^2(\phi) dS \tag{3.31}$$

where the integral runs over the surface of the unit sphere. The term $\Delta\sigma(\omega) = -2\sigma_{10}(\omega) + \sigma_{21}(\omega)$ is the (theoretical) isotropic cross section which encompasses the bleaching band and induced absorption, see Eq. 3.27. By explicitly solving the integrals using Eq. 3.29, we find the initial parallel and perpendicular signals in

terms of the isotropic response as

$$\Delta\alpha_{\parallel}(\omega,0)=\frac{9}{5}\Delta\sigma(\omega)N_1(0)\qquad\text{and}\qquad\Delta\alpha_{\perp}(\omega,0)=\frac{3}{5}\Delta\sigma(\omega)N_1(0),\tag{3.32}$$

which shows that the parallel transient response is three times larger than that in perpendicular configuration. Over time, the preceding quantities will vanish due to molecular randomization and vibrational relaxation. The relative difference between the parallel and perpendicular signals will reduce over the time due to orientational diffusion of the excited oscillators.

If we are interested only in vibrational relaxation, the free-of-rotation transient signal corresponding to the isotropic transient absorption is constructed as follows

$$\Delta\alpha_{\text{iso}}(\omega,t)=\frac{\Delta\alpha_{\parallel}(\omega,t)+2\Delta\alpha_{\perp}(\omega,t)}{3},\tag{3.33}$$

where one can prove that $\Delta\alpha_{\text{iso}}(\omega,t)=\Delta\sigma(\omega)N_1(t)$, which resembles Eq. 3.27.

On the other hand, if we are interested in molecular orientation, we measure the difference between parallel and perpendicular signals as a function of time. The anisotropy, which depends exclusively on molecular reorientation dynamics, is given by

$$R(\omega,t)=\frac{\Delta\alpha_{\parallel}(\omega,t)-\Delta\alpha_{\perp}(\omega,t)}{\Delta\alpha_{\parallel}(\omega,t)+2\Delta\alpha_{\perp}(\omega,t)}.\tag{3.34}$$

Whilst it is easy to derive $R(t=0)=2/5$, the time-dependent anisotropy is related to the time-dependent orientational distribution of the excited oscillators by[127]

$$R(t)=\frac{3}{5}\langle\cos^2\theta_r(t)\rangle-\frac{1}{5},\tag{3.35}$$

where $\theta_r(t)$ is the angular displacement of a given transition dipole moment over the time and $\langle\cdots\rangle$ indicates the ensemble average. The anisotropy of OD/OH stretch oscillators isotopically diluted in H_2O/D_2O follows a single exponential decay, such that

$$R(t)=\frac{2}{5}\exp(-t/\tau_r),\tag{3.36}$$

with a reorientation time constant of $\tau_r\sim$2.5 ps for both vibrations at room temperature.[25,26] In general, the orientational dynamics of a vibration is strongly dependent on the interactions with its surroundings, as we will see in subsequent chapters.

3.6 Experimental realization

The results described in Chapters 7–9 consist of the study of the effects on water structure and dynamics using the OD and OH stretch vibrations as a probe. We perform experiments in a concentration dependent manner to address the extent to which the presence of ions affects the structural dynamics of water. We also discuss the local ordering of water in solvation shells–an effect caused by the strong local electric fields of ions. While the preparation of every sample is discussed separately in each experimental chapter, the two setups used for vibrational spectroscopy will be described here:

1. Linear infrared spectroscopy: Fourier-transform infrared (FT-IR) spectrometers are widely used to extract IR spectra in a rapid way over wide spectral ranges, in contrast to dispersive spectrometers limited to narrow spectral steps at the time.[128] In general, a FT-IR spectrometer starts with broadband collimated light source. Based on a Michelson interferometer, the light passes through a beam splitter that generates a reference beam and a second beam that must interact with the sample. The two beams are then reflected by two mirrors back and recombine in the same beam splitter, forming a third propagation arm that contains an interference pattern. Since this pattern is sensitive to the difference between the two optical path lengths, one could measure the interferogram as a function of the retardation between the two beams. This function is linked to the absorption spectrum by a Fourier transformation.[128]

   Using FT-IR spectrometers, one can extract the IR spectrum of a given sample at once, and average over multiple scans in a reliable and easy manner. All FT-IR-based linear spectra presented in this thesis were measured in transmission mode on two comparable spectrometers: Bruker Vertex 70 and Bruker Vertex 80v. In both cases, we measured in the spectral range of 1000–4000 cm^{-1} with a resolution of 2 cm^{-1}.

2. One-color mid-IR pump-probe spectroscopy: this technique offers a tool to track the dynamics of vibrations in real time, as has been described in the previous sections. For a reliable determination of vibrational and reorientation dynamics these experiments rely on having pulses with a duration significantly shorter than the lifetime of the vibration under study. Studies based on OH/OD stretch vibrations require the use of sub-ps IR pulses. Measurements were performed on a setup that integrates a commercially available femtosecond IR pulse generator and an in-house built optical setup to generate different beams and to modulate the pump-to-probe delay time.

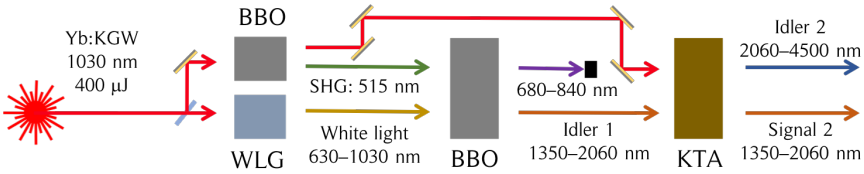

Figure 3.8. Schematic of the frequency conversion process to generate ultrafast IR pulses. BBO: barium borate crystal. WLG: white light generation substrate, sapphire. SHG: second harmonic generation. KTA: potassium titanyle arsenate crystal.

3.6.1 Ultrafast pulse generation

As displayed in Figure 3.8, the required femtosecond mid-IR pulses are generated by a multiple frequency conversion process from a near-IR pulsed laser with a repetition rate up to 50 kHz (Yb:KGW, Light Conversion Pharos). Each pulse from the laser has an energy of 400 μJ and is centered at 1030 nm. All pump-probe experiments presented in this thesis where set to a repetition rate of 1 kHz, using the built-in pulse picker of the laser.

These pulses interact with multiple non-linear crystals inside an optical parametric amplifier (OPA, Light Conversion Orpheus-ONE-HP) to generate pulses at the desired IR frequency. Briefly, in the first stage, the beam is split in two beams. The first beam is frequency doubled (515 nm) in a BBO crystal (barium borate), while the second beam is focused into a white light generation substrate to produce a tunable beam in the frequency range of 630–1030 nm. These two resulting beams interact in a second BBO crystal that leads to a signal beam S1 (680–840 nm), and an idler beam ID1 (1350–2060) which will be used as seed in a subsequent interaction. Ultimately, a KTA crystal (potassium titanyle arsenate) is used to combine the ID1 seed with the residual fraction of the fundamental after the second harmonic generation process. These processes lead to a strong signal beam S2 (1350–2060 nm), and an idler beam ID2 (2060–4500 nm).

For the pump-probe experiments described in this thesis, the laser was set to the resonance frequency of the OH and the OD stretch vibrations. For the former vibration that peaks at 2510 cm^{-1} ($\sim$4000 nm), the pulses have an energy of 12μJ, a bandwidth of 120 cm^{-1} and a duration of 200 fs. For the latter vibration the laser was set at 3390 cm^{-1}, where the energy of the pulses is 25μJ, the bandwidth 90 cm^{-1} and the duration 280 fs.

3.6.2 Pump-probe optical setup

As discussed previously in Section 3.4 and expressed in Eq. 3.24, the aim of pump-probe spectroscopy is to measure the time-dependent changes in absorption as

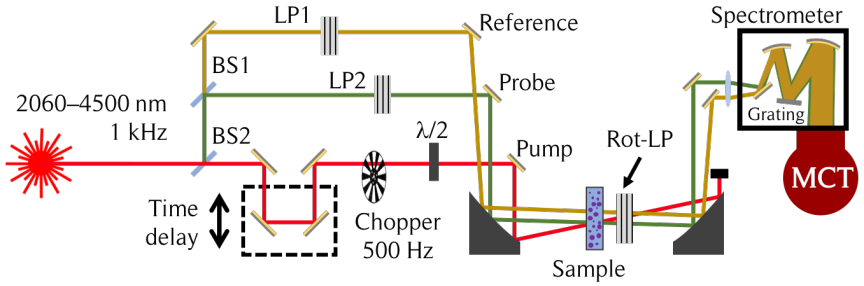

Figure 3.9. Schematic of the pump-probe optical setup. BS: ZnSe beam splitter, LP: wire-grid linear polarizer, $\lambda/2$: zero-order half-wave plate, Rot-LP: rotational wire-grid linear polarizer, MCT: mercury-cadmium-telluride detector.

a given sample is perturbed by an intense pump pulse. The experimental setup consists of the following elements: pump pulses, probe pulses, a time-modulation translational stage and an IR sensitive detector. A schematic of the setup is shown in Figure 3.9.

After setting the laser at the desired frequency, the beam (p-polarized) is directed to a ZnSe beam splitter at an incident angle of 45^o, which transmits most of the light ($\sim$90%) to generate the pump beam. The reflected light is directed to a second ZnSe beam splitter to form the probe and the reference beam. The pump beam is sent to a computer-controllable translational stage to modulate the pump-to-probe time delay. Using a zero-order $\lambda/2$ plate, the polarization of the pump beam is set to 45° with respect of that polarization of the probe and reference beams. To determine pumped and unpumped transient signals, a chopper blade at a frequency of 500 Hz is placed in the pump optical path. Two wire-grid linear polarizers are used, one for the reference and one for the probe, to filter out undesired perpendicular or elliptical components.

At this point, pump and probe are focused into the sample at the same spot, while the reference passes through the sample but does not overlap with the other beams. Directly after the sample, a rotating lineal polarizer is used to selectively filter out either the parallel or perpendicular components of the probe and the reference. This enables measurements to be taken in a polarization-resolved manner. After this selective step, the pump beam is blocked, while probe and reference are directed into a grating-based spectrometer that disperses the light onto a 3×32-pixel array MCT (mercury-cadmium-telluride) detector.

The intensity of the probe is normalized with the intensity of the reference, and

the transient absorption change is given by

$$\Delta\alpha(\omega,t) = -\ln\underbrace{\left[\frac{I_{\text{probe}}(\omega,t)}{I_{\text{ref}}(\omega,t)}\right]}_{\text{pumped}} + \ln\underbrace{\left[\frac{I_{\text{probe},0}(\omega,t)}{I_{\text{ref},0}(\omega,t)}\right]}_{\text{unpumped}}, \tag{3.37}$$

which leads to

$$\Delta\alpha(\omega,t) = -\ln\left[\frac{I_{\text{probe}}(\omega,t)}{I_{\text{ref}}(\omega,t)}\frac{I_{\text{ref},0}(\omega,t)}{I_{\text{probe},0}(\omega,t)}\right]. \tag{3.38}$$

The preceding equation enables us to correct for shot-to-shot intensity fluctuations of the probe. This relation holds valid for both parallel and perpendicular transient absorption.

3.7 Data analysis and modeling

In this section we describe the the procedures used to extract information from our pump-probe experimental data. The transient signal is characterized by an excited state that decays ultimately into a hot ground state. However, the relaxation mechanism can be quite complicated, since the relaxation process may involve intermediate states. In aqueous solutions, additional excitation may appear due to the inhomogeneities caused by the solutes. One can often distinguish hydration water molecules from those which are far from any ion and behave in a bulk-like manner. In general, ions generate strong local electric field that change the spectra and relaxation rates of vibrations in their immediate vicinity. Therefore, the pump pulse might excite different vibrations at the same time, leading to a complicated spectral response.

We build up the analysis starting with the isotropic signal $\Delta\alpha_{\text{iso}}$, which is insensitive to molecular reorientation. We assume that the relaxation process consists of a linear combination of discrete relaxation steps, where each level is associated to a different spectral component with different population dynamics. As such, we can write

$$\Delta\alpha_{\text{iso}}(\omega,t) = \sum_{i=1}^{n}\Delta\sigma_i(\omega)N_i(t), \tag{3.39}$$

with $\Delta\sigma_i$ the spectral signature of each constituent component and N_i its corresponding population dynamics. The factor n represents the number of energy levels that the relaxation mechanism possesses.

For the simplest relaxation mechanism, a two-level system, the population dy-

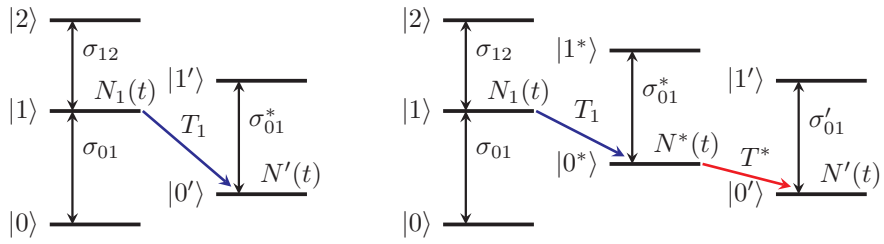

Figure 3.10. Left: One-step relaxation mechanism in which the excited oscillators relax directly to a final state (not necessarily the original ground state). **Right:** Two-step relaxation mechanism in which the excited oscillators decay first to an intermediate state, before attaining the final equilibrium state. The difference between the final state and the original ground state accounts for irreversible changes or heating in the sample due to the intense pump pulse.

namics can be represented by the following set of differential equations

$$\frac{d}{dt}\begin{pmatrix} N_1(t) \\ N'(t) \end{pmatrix} = \begin{pmatrix} -k_1 & 0 \\ +k_1 & 0 \end{pmatrix}\begin{pmatrix} N_1(t) \\ N'(t) \end{pmatrix} \qquad \text{with} \qquad N_i(0) = \begin{pmatrix} N_1(0) \\ 0 \end{pmatrix} \tag{3.40}$$

where N_1 and N' refer to the population dynamics of the excited and a final state that is not necessarily the ground state, and the relaxation rate k_1 is the reciprocal of the vibrational lifetime T_1. Solving these equation leads to the following description

$$\Delta\alpha_{\text{iso}}(\omega, t) = \Delta\sigma_1(\omega)N_1(0)e^{-k_1 t} + \Delta\sigma'(\omega)N_1(0)\left(1 - e^{-k_1 t}\right), \tag{3.41}$$

where $\Delta\sigma_1(\omega) = -2\sigma_{10}(\omega)+\sigma_{21}(\omega)$ is the transient spectral response of the excited state, and $\Delta\sigma' = \sigma'_{10}(\omega) - \sigma_{10}(\omega)$ associated with the final state, as described in Eqs. 3.24 and 3.27. This relaxation mechanism is represented in the left side of Figure 3.10.

Unfortunately, the vibrational relaxation process in aqueous systems is never this simple. It has been demonstrated that the vibrational relaxation dynamics of OD/OH stretch vibrations in isotopically diluted H_2O/D_2O is well described by a two-step consecutive model as shown in the right side of Figure 3.10,[25,26] in which the population dynamics are represented with the following differential equations

$$\frac{d}{dt}\begin{pmatrix} N_1(t) \\ N^*(t) \\ N'(t) \end{pmatrix} = \begin{pmatrix} -k_1 & 0 & 0 \\ +k_1 & -k^* & 0 \\ 0 & +k^* & 0 \end{pmatrix}\begin{pmatrix} N_1(t) \\ N^*(t) \\ N'(t) \end{pmatrix}, \tag{3.42}$$

where the initial conditions are $N_i(0) = (N_1(0), 0, 0)$. In this model, the system relaxes via an intermediate state $|0^*\rangle$ to the hot ground state $|0'\rangle$. It has been

found previously that the intermediate state has the same spectrum as the ground ground state ($\sigma^*_{01} = \sigma_{01}$), meaning that the intermediate state has no associated transient spectrum. In this case, the isotropic transient signal can be model as

$$\begin{aligned}\Delta\alpha_{\text{iso}}(\omega,t) &= \Delta\sigma_1(\omega)N_1(0)e^{-k_1 t} \\ &+ \Delta\sigma'(\omega)N_1(0)\left(1+\frac{k_1}{k^*-k_1}e^{-k^* t}-\frac{k^*}{k^*-k_1}e^{-k_1 t}\right), \quad (3.43)\end{aligned}$$

with $\Delta\sigma_1(\omega) = -2\sigma_{10}(\omega) + \sigma_{21}(\omega)$ the transient signal of the excited state, and $\Delta\sigma' = \sigma'_{10}(\omega) - \sigma_{10}(\omega)$ the transient signal associated with the hot ground state.

For more complex models, providing a solution to the set of differential equations becomes complicated and tedious for numerical analyses. A easier solution consists of diagonalizing the rate matrix K of the Eqs. 3.40 and 3.42 written in matrix form as

$$\frac{d}{dt}\vec{N} = K\vec{N}. \quad (3.44)$$

We aim to find a unitary matrix U such that $KU = U\lambda$, where λ is a diagonal matrix that contains the eigenvalues and U contains the vectors that form the eigenbasis. As such, the population dynamics are given by

$$\vec{N}(t) = U\exp(\lambda t)U^{-1}\vec{N}(0), \quad (3.45)$$

which offers a general solution as a linear combination of exponential decays in terms of the eigenvalues of the rate matrix K.

To extract meaningful information from the experimental data $\Delta\alpha^{\text{exp}}_{\text{iso}}(\omega,t)$ with standard deviation $\xi(\omega,t)$, we perform least-squares fits to minimize the following weighted χ^2 function

$$\chi^2 = \int\int\left(\frac{\Delta\alpha^{\text{exp}}_{\text{iso}}(\omega,t) - \sum_i \Delta\sigma_i(\omega)N_i(t)}{\xi(\omega,t)}\right)^2 dtd\omega, \quad (3.46)$$

in which the spectral components $\Delta\sigma_i$ and the decay rate constants $\mathbf{k}$ are treated as fit parameters.

If one knows the relaxation mechanism $K(\mathbf{k})$, the time traces $\vec{N}$ are determined by the $\mathbf{k}$ parameters, and we can find the spectral components that minimize the χ^2 function at all times. This method is usually called spectral decomposition. This approach starts out with an estimate for the decay rates $\mathbf{k}$, from which a subsequent minimization process finds the spectral signatures that best fit the experimental data following the expression

$$\frac{d}{d\tilde{\sigma}_i(\omega)}\int\left(\frac{\Delta\alpha^{\text{exp}}_{\text{iso}}(\omega,t) - \sum_i \Delta\tilde{\sigma}_i(\omega)N_i(\mathbf{k},t)}{\xi(\omega,t)}\right)^2 dt = 0 \quad (3.47)$$

to find the optimal decay rates $\mathbf{k}$. A minimization routine following this approach is shown in Listing 3.1 using the kinetic model from Eq. 3.42.

Analogously, if one knows the spectral components $\Delta\sigma_i$, one can run a minimization process to extract the time traces that best fit the experimental data. This approach is called temporal decomposition, and from

$$\frac{d}{d\tilde{N}_i(t)} \int \left(\frac{\Delta\alpha_{\text{iso}}^{\text{exp}}(\omega,t) - \sum_i \Delta\sigma_i(\omega)\tilde{N}_i(t)}{\xi(\omega,t)} \right)^2 d\omega = 0, \tag{3.48}$$

we obtain the population dynamics. This approach is more convenient for the study of samples in which unconventional processes, such as Förster resonance energy transfer,[129] play an important role in the relaxation dynamics. A complete analysis of experimental data that show a Förster-like relaxation process is available at https://github.com/RobertoCota/Forster-energy-transfer

To extract information on the molecular reorientation dynamics, we use Eqs. 3.33, 3.34 and 3.39 to define the following equations

$$\Delta\alpha_{\parallel}(\omega,t) = \sum_{i=i}^{n}[1+2R_i(t)]N_i(t)\Delta\sigma_i(\omega) = \sum_{i=1}^{n} N_{i,\parallel}(t)\Delta\sigma_i(\omega) \tag{3.49}$$

$$\Delta\alpha_{\perp}(\omega,t) = \sum_{i=i}^{n}[1-R_i(t)]N_i(t)\Delta\sigma_i(\omega) = \sum_{i=1}^{n} N_{i,\perp}(t)\Delta\sigma_i(\omega), \tag{3.50}$$

in which we associate an anisotropy $R_i(t)$ with each spectral component. To this purpose, we can perform a temporal decomposition minimization on both parallel and perpendicular signals. Having retrieved $N_{i,\parallel}(t)$ and $N_{i,\perp}(t)$, we can calculate the anisotropy of each constituent component as

$$R_i(t) = \frac{N_{i,\parallel}(t) - N_{i,\perp}(t)}{N_{i,\parallel}(t) + 2N_{i,\perp}(t)}. \tag{3.51}$$

A global minimization is possible by performing a least-square routine to minimize the following χ^2 function

$$\begin{aligned}\chi^2 = \int\int dtd\omega \Bigg[&\left(\frac{\Delta\alpha_{\parallel}^{\text{exp}}(\omega,t) - \sum_i[1+2R_i(t)]N_i(t)\Delta\sigma_i(\omega)}{\xi_{\parallel}(\omega,t)} \right)^2 \\ &+ \left(\frac{\Delta\alpha_{\perp}^{\text{exp}}(\omega,t) - \sum_i[1-R_i(t)]N_i(t)\Delta\sigma_i(\omega)}{\xi_{\perp}(\omega,t)} \right)^2 \Bigg]\end{aligned} \tag{3.52}$$

where parallel and perpendicular signals are minimized simultaneously. As shown in Chapter 7, this equation can be used to perform spectral decomposition if one de-

fines the relaxation pathway and assign functional forms to each R_i component. An example of this type of analysis is available at https://github.com/RobertoCota/Time-resolved-vibrational-spectroscopy.

```
###   SPECTRAL DECOMPOSITION   ###

import numpy as np
from scipy.optimize import least_squares

def Residuals(params, Nt, Dat, StdDat):
    Sig_v = np.array(params)
    diff = np.power((Dat - Nt@Sig_v)/StdDat,2.0)
    return diff.reshape(-1)

def Chi2_Iso(Par, Lambda_Pop, freq, time, data, data_e):

    KineticModel = np.array([[ -Par[0],       0.0,   0.0],
                             [ +Par[0],   -Par[1],   0.0],
                             [     0.0,   +Par[1],   0.0]])

    EigenVectors, EigenValues = KineticModel.diagonalize()

    N0 = np.array([1,0,0])

    #Given the decay rates, compute the population matrix
    Popt = EigenVectors@np.exp(EigenValues*time)@(EigenVectors
    **-1)@N0

    #Create the spectra matrix
    Spectra = np.zeros((len(N0),len(freq)), dtype = 'float64')

    #Initial zeros
    p0 = np.zeros((len(N0)),dtype='float64')

    #Find the frequency components that best fit the
    experimental data
    for i in range(len(freq)):
        params = least_squares(Residuals, p0, args=(Popt, data
    [:,i], data_e[:,i]), method='trf', loss='linear', max_nfev =
     1000)
        p0 = params['x']
        Spectra[:,i] = params['x']

    #Save the spectral signature for future use
    np.savetxt('Write_FileName',Spectra,fmt='%.18e', delimiter='
    \t')

    #Chi-square function
    X2 = np.power((data - Popt@Spectra)/data_e,2.0)
    return X2.reshape(-1)

```

```
#Importing experimental data
t = np.loadtxt('File_Time')
omega = np.loadtxt('File_Frequency')

Iso_signal = np.loadtxt('File_ExperimentalData')
Iso_error = np.loadtxt('File_ExperimentalStDev')

#Initial estimation: decay rates
k0 = [1.0/1.7, 1.0/1.2]

#Least-square minimization
OptPar = least_squares(Chi2_Iso, k0, args=(omega, t, Iso_signal,
     Iso_error), method='trf', loss='linear', max_nfev = 3000)

### OptPar['x']:    optimized decay rates
### OptPar['jac']:  optimized Jacobian to be used for
    statistical analysis
```

Listing 3.1. Python script for the analysis of isotropic transient absorption in which a two-step consecutive model, represented by Eqs. 3.42 and 3.43, is used.

4

Evidence for reduced hydrogen-bond cooperativity in ionic solvation shells from isotope-dependent dielectric relaxation*

We find that the reduction in dielectric response (depolarization) of water caused by solvated ions is different for H_2O and D_2O. This isotope dependence allows us to reliably determine the kinetic contribution to the depolarization, which is found to be significantly smaller than predicted by existing theory. The discrepancy can be explained from a reduced hydrogen-bond cooperativity in the solvation shell: we obtain quantitative agreement between theory and experiment by reducing the Kirkwood correlation factor of the solvating water from 2.7 (the bulk value) to $\sim$1.6 for NaCl and $\sim$1 (corresponding to completely uncorrelated motion of water molecules) for CsCl.

* *This chapter is based on:* Roberto Cota, Niklas Ottosson, Huib J. Bakker and Sander Woutersen, *Evidence for reduced hydrogen-bond cooperativity in ionic solvation shells from isotope-dependent dielectric relaxation*, Phys. Rev. Lett. **2018**, 120, 216001.

4.1 Introduction

The solvation of ions in water plays a crucial role in numerous physical, chemical and biological processes, ranging from ion transport in fuel cells to the electrostatic screening of DNA. As such, ion hydration is a subject of intense and active experimental and theoretical physical research.[130–135] Dielectric relaxation spectroscopy (DRS, Chapter 2), is widely used to investigate water and aqueous solutions. With this method crucial information on the structure and dynamics of aqueous solutions can be obtained,[27,33,36,37,42,45,101,136–139] in particular on the effect of ions on the hydrogen-bond network of water. Ions generate strong local electric fields, orienting the dipole moments of the neighbouring water molecules in solution, and thus causing a reduction in the dielectric response of the water, an effect referred to as depolarization. As has been discussed previously in Section 2.5, this depolarization is the sum of three contributions: (i) the dilution of the water solvent,[93,95,140] (ii) the strongly reduced mobility of water molecules solvating the ions (static depolarization)[106] and (iii) the reaction of water molecules to the moving ions (kinetic depolarization): an ion moving in the direction of an externally applied electrical field causes a reorientation of the surrounding water molecules such that their dipoles are directed opposite to the applied field.[109–114]

To investigate the structure and dynamics of water in electrolyte solutions using DRS, one must separate the different contributions to the depolarization. For the dilution contribution this is trivial, but the static and kinetic depolarization are difficult to separate. A common approach to address this problem is to subtract a theoretical prediction for the kinetic-depolarization contribution from the observed depolarization (corrected for dilution), thus obtaining an estimate for the static depolarization. The amplitude of the static depolarization can then be used to estimate the number of water molecules immobilized per solvated cation, the so-called hydration number (the contribution of the anions to the static depolarization is negligible).[18,27,36,45,51,105–108,115] To this purpose, the most commonly used models for kinetic depolarization (originally developed by Onsager and Hubbard,[109–111] and later extended by others[113,114,141]) integrate the local electromagnetic interactions in the framework of the Navier-Stokes equations of motion for the water. These models provide a closed expression of the kinetic depolarization in terms of the DC conductivity and the Debye relaxation time of the water. As yet, experimental tests of these models for kinetic depolarization are largely lacking. The above-mentioned subtraction procedure sometimes leads to unphysical results, such as negative values for the static depolarization[47] (which would imply negative hydration numbers), which indicates the need for an experimental investigation of kinetic depolarization.

Here, we use the isotope dependence of the depolarization to investigate the kinetic contribution for a series of NaCl and CsCl solutions. We find that the experimentally determined kinetic depolarization is much smaller than the kinetic

depolarization that follows from commonly used models. This discrepancy is due to the assumption that the solvating water has the same dielectric response as bulk water, which is incorrect since the ions locally disrupt the hydrogen-bond structure of water.[14,142–149]

4.2 Experimental

We record dielectric spectra of NaCl and CsCl solutions in H_2O and D_2O in the frequency range of 1–50 GHz, which fully covers the main relaxation mode of water at ∼18 GHz.[85] The experimental setup used for these experiments is described in Section 2.6. The complex permittivity of the solutions is recorded for a range of concentrations (0.0–1.0 mol/l). These experiments were carried out at 23°C.

The total dielectric permittivity of the solutions is well described by the sum of a Cole-Cole relaxation term for water and an ionic-conductivity term (see Section 2.4):

$$\hat{\epsilon}(\nu) = \epsilon_\infty + \frac{\epsilon_s - \epsilon_\infty}{1 + (i2\pi\nu\tau_D)^{1-\alpha}} - \frac{i\sigma}{2\pi\nu\epsilon_0}, \tag{4.1}$$

where ϵ_s is the static permittivity at low frequencies, ϵ_∞ is the asymptotic permittivity at high frequencies, ϵ_0 is the vacuum permittivity, τ_D the Debye relaxation time, α a parameter characterizing the width of the distribution of relaxation times, σ the DC ionic conductivity, and $A_D = \epsilon_s - \epsilon_\infty$ the amplitude of the Debye relaxation mode. We determine these parameters by performing a least-squares fit of Eq. 4.1 to the data displayed in Figure 4.1. The dielectric response at high frequencies is independent of concentration (as has been observed previously[36,86,117]), so in the fit we keep ϵ_∞ fixed to its zero-concentration value.

4.3 Results

Figure 4.1 shows the complex permittivity of the investigated solutions, after subtraction of the ionic-conductivity contribution. Both the addition of NaCl and CsCl leads to a significant reduction of the dielectric response. The curves in Figure 4.1 are the result of the least-squares fits, and Figure 4.2a shows the concentration-dependent conductivity σ obtained from the fits. The values in H_2O agree well with previous results (see Appendix).[45,150] The conductivities of all the solutions are well described by the empirical function $\sigma(c) = Dc - Ec^{3/2}$, which has the same functional form as Kohlrausch's law that applies to dilute solutions. To correct the A_D obtained from the fit for the trivial dilution effect, we define the

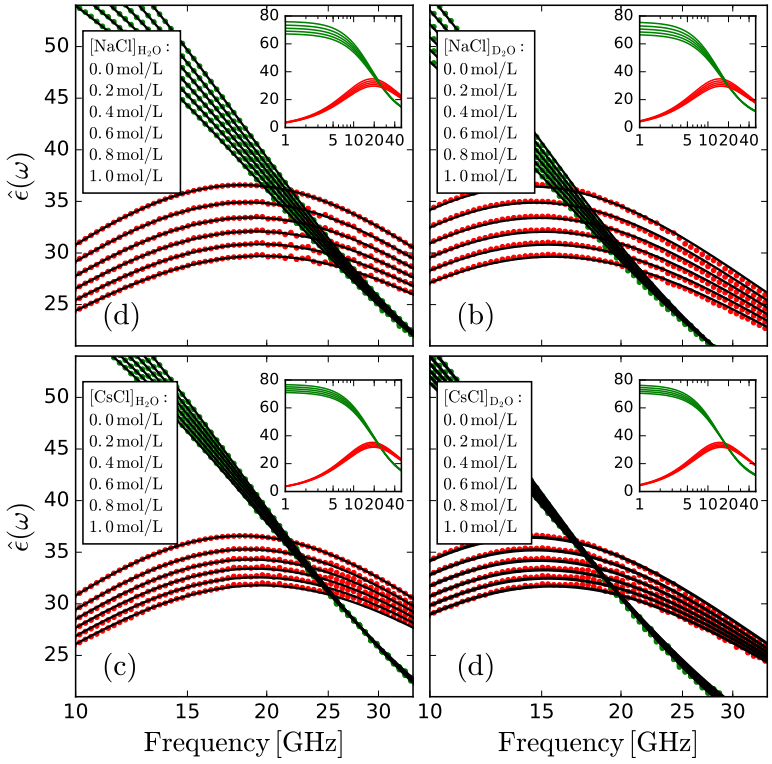

Figure 4.1. Complex dielectric permittivity spectra of aqueous solutions of NaCl in H_2O (a), NaCl in D_2O (b), CsCl in H_2O (c) and CsCl in D_2O ranging from the neat solvent to 1.0 mol/L at 23°C. The red and green dots indicate the data measured by DRS for the dielectric diffusion $\epsilon'(\omega)$ and dielectric losses $\epsilon''(\omega)$, respectively. The solid lines are fits to Eq. 4.1. All data is tabulated in the Appendix.

concentration-dependent quantity

$$A_{\mathrm{D,n}}(c) = \frac{c_{\mathrm{w}}(c)}{c_{\mathrm{w,0}}} A_{\mathrm{D,0}}, \tag{4.2}$$

with $A_{\mathrm{D,0}}$ and $c_{\mathrm{w,0}}$ the amplitude of the Debye relaxation and the molecular concentration of undiluted neat water, and $c_{\mathrm{w}}(c)$ is the water concentration of the electrolyte solution. $A_{\mathrm{D,n}}$ is the (hypothetical) dielectric strength if the only effect of ions in water would be a reduction in water concentration. The dilution-corrected depolarization

$$\Delta A_{\mathrm{D}} = A_{\mathrm{D,n}} - A_{\mathrm{D}}, \tag{4.3}$$

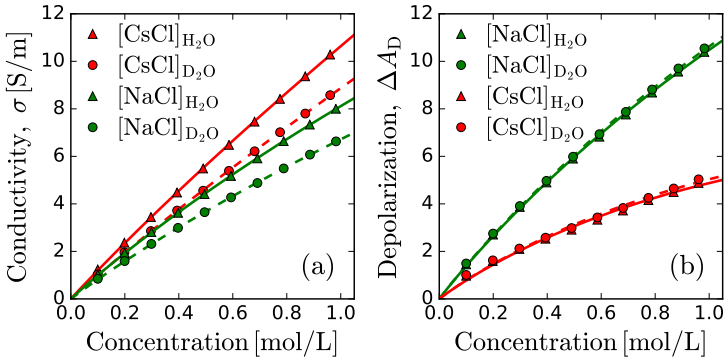

Figure 4.2. (a) Conductivity σ as a function of the salt concentration for four salt solutions. (b) Depolarization as a function of concentration for the same solutions as in the left panel. The triangles and circles represent ions dissolved in H_2O and D_2O, respectively; red and green refer to solutions with Na^+ and Cs^+ ions, respectively.

is the depolarization caused by the interaction of the ions and the water. In the following, the term depolarization will refer to this dilution-corrected quantity ΔA_D.

Figure 4.2b shows that the depolarization ΔA_D increases with concentration. In addition, there is a small but significant isotope effect: the depolarization is larger for D_2O than for H_2O solutions. This can be seen more clearly in Figure 4.3, where we present the isotope-difference $\Delta A_D^{H_2O} - \Delta A_D^{D_2O}$ as a function of concentration. Dividing this difference by the value of ΔA_D itself (Fig. 4.2b), we find that the isotope-effect is ∼1.5% for NaCl and ∼3% for CsCl solution. The depolarization consists of a static and kinetic contribution:[106,109,110,112–114] $\Delta A_D = \Delta A_{D,st.} + \Delta A_{D,kin.}$ The dipole moments of H_2O and D_2O differ by only 0.06%,[151] which is negligible compared to the observed isotope effect, and to the uncertainty in our data. Hence, the static contributions to the depolarization can be assumed equal for H_2O and D_2O, so that

$$\Delta A_D^{H_2O} - \Delta A_D^{D_2O} = \Delta A_{D,kin.}^{H_2O} - \Delta A_{D,kin.}^{D_2O} \tag{4.4}$$

The preceding result enables us to determine the kinetic depolarization independently from the static depolarization. In particular, we can directly compare the experimentally observed $\Delta A_{D,kin.}^{H_2O} - \Delta A_{D,kin.}^{D_2O}$ to theoretical predictions.

4.4 Determining the reduced cooperativity of water near ions

The most commonly used model for kinetic depolarization is the continuum model derived by Hubbard and Onsager[110,112] (see Section 2.5). In this model, the response of the water surrounding the moving ions is described as a continuum exhibiting the same Debye-relaxation behaviour as bulk neat water. Provided that the viscous frictional forces are much larger than the dielectric drag, the predicted kinetic depolarization is then given by

$$\Delta A^{\mathrm{HO}}_{\mathrm{D,kin.}} = p\sigma(c)\left(\frac{\tau_{\mathrm{D}}}{\epsilon_0}\cdot\frac{\epsilon_s-\epsilon_\infty}{\epsilon_s}\right), \tag{4.5}$$

where $\sigma(c)$ is the concentration-dependent specific conductivity, τ_{D} the Debye-relaxation time, and p a factor which characterizes the tangential contact forces between the water molecules and ion surface, the limiting cases being perfect slip (no tangential force, $p = 2/3$), and perfect stick (infinite tangential force, $p = 1$). This equation has no explicit dependence on the size of the ions. Since we measure all the parameters entering Eq. 4.5 for both H_2O and D_2O, we can directly test the validity of the Hubbard-Onsager model for the kinetic depolarization using Eq. 4.4. The red lines in Figure 4.3 are the theoretical predictions for perfect slip (solid lines) and perfect stick (dashed lines). Clearly, the Hubbard-Onsager model predicts a much larger H_2O/D_2O difference in kinetic depolarization than is observed experimentally.

In a later, more rigorous theory for the kinetic depolarization, Hubbard, Colonomos and Wolynes describe the system as ionic spheres immersed in a solution of rotating dipoles, which are again assumed to exhibit Debye relaxation identical to that of bulk water. In this model the finite size of the solvent molecules is taken into account (as opposed to the earlier continuum model). They obtained an expression for the depolarization in which the radius of the ion occurs explicitly:[112]

$$\Delta A^{\mathrm{HCW}}_{\mathrm{D,kin.}} = \frac{p\sigma(c)\tau_{\mathrm{D}}}{\epsilon_0}\left[\frac{NR_i}{e}\left\langle\frac{\vec{\mu}\cdot\hat{r}}{r^2}\right\rangle\right], \tag{4.6}$$

where N is the number of water dipoles per volume unit, R_i the ionic radius, μ the water molecule dipole moment, r the distance between the water molecule and the ion and e the ionic charge. In Ref. 112 the authors numerically evaluated the number in square brackets in Eq. 4.6, in particular for Na^+, Cs^+ and Cl^-. The $\Delta A^{\mathrm{H_2O}}_{\mathrm{D,kin.}} - \Delta A^{\mathrm{D_2O}}_{\mathrm{D,kin.}}$ predicted by this theory is shown as the green lines in Figure 4.3, again for both limiting values of p. Again, the theory predicts a much larger difference in kinetic depolarization than is observed experimentally.

The discrepancy between the theoretically predicted and experimentally ob-

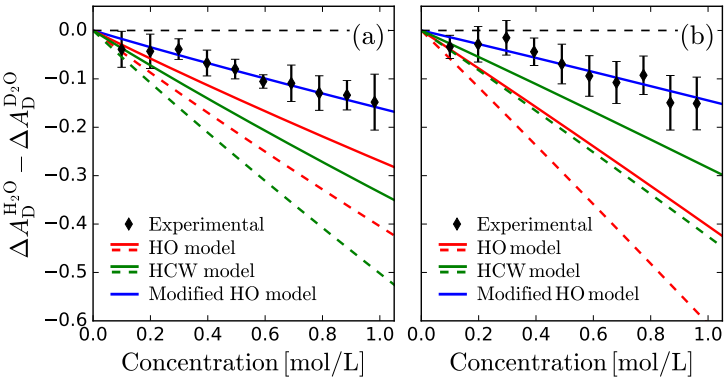

Figure 4.3. (a) Difference between the depolarization of NaCl in H_2O and the depolarization of NaCl in D_2O as a function of concentration. (b) Difference between the depolarization of CsCl in H_2O and the depolarization of CsCl in D_2O as a function of concentration. The experimental results are represented by the diamonds. The solid lines represent calculations of the depolarization difference with different models for the kinetic depolarization using $p = 2/3$ (solid lines) and $p = 1$ (dashed lines). The solid blue line represents a fit to the data with the modified Hubbard-Onsager model of Eq. 4.8.

served kinetic depolarization can be explained if the water surrounding the ions exhibits a smaller dielectric response than bulk water. In neat water, the highly organized hydrogen-bond structure leads to highly cooperative reorientational motion of water molecules. As a consequence, the theory for the dielectric response of a liquid consisting of randomly moving dipoles (originally derived by Onsager[140]) predicts a dielectric constant that is much smaller than observed. This is phenomenologically corrected in the Kirkwood-Fröhlich equation:

$$\frac{(\epsilon_s - \epsilon_\infty)(2\epsilon_s + \epsilon_\infty)}{\epsilon_s(\epsilon_\infty + 2)^2} = \frac{\rho\mu^2 g_K}{9\epsilon_0 k_B T} \qquad \Rightarrow \qquad \epsilon_s \approx \frac{\rho\mu^2 g_K}{18\epsilon_0 k_B T}(\epsilon_\infty + 2)^2, \tag{4.7}$$

where ρ is the density of water molecules, k_B Boltzmann's constant, μ the molecular dipole moment, and g_K the Kirkwood correlation factor (see Section 2.3.3). The limit $g_K = 1$ corresponds to completely uncorrelated motion of the molecules, and $g_K > 1$ to correlated motion. For bulk liquid water, the experimentally determined value is $g_{K,bulk} = 2.7$. As can be seen in Eq. 4.7, the Kirkwood factor effectively scales up the dielectric response with respect to its theoretical value in the case of completely uncorrelated orientational motion.

The Hubbard-Onsager expression for the kinetic depolarization assumes that the dielectric response of water surrounding ions is the same as that of bulk water, i.e. that it has a Kirkwood factor of 2.7. However, ions tend to disrupt the hydrogen-

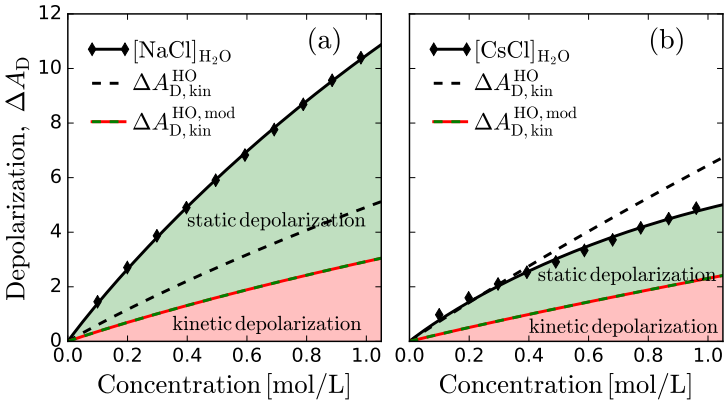

Figure 4.4. Experimentally observed total depolarization (corrected for dilution) of NaCl (a) and CsCl (b) in H_2O, and its decomposition into the static and the kinetic depolarization using the modified Onsager-Hubbard model (Eq. 4.8). The dashed black curve shows the kinetic depolarization predicted by the conventional Hubbard-Onsager equation. In the case of CsCl the conventional Hubbard-Onsager equation predicts a kinetic depolarization that is larger than the observed total depolarization, which would imply a negative static depolarization, and thus a negative hydration number.

bond structure of liquid water, and thus the reorientation of the water molecules surrounding the ions will be less correlated than that of the molecules in bulk water. To account for this effect, we modify the Hubbard-Onsager expression as follows:

$$\Delta A^{\mathrm{HO,mod.}}_{\mathrm{D,kin.}} = \frac{p\sigma(c)\tau_{\mathrm{D}}}{\epsilon_0}\frac{g_{\mathrm{K,ion}}}{g_{\mathrm{K,bulk}}}\left[\frac{\epsilon_s - \epsilon_\infty}{\epsilon_s}\right], \tag{4.8}$$

where we have introduced an effective Kirkwood factor $g_{\mathrm{K,ion}}$ for the water surrounding the ions. The value of $g_{\mathrm{K,ion}}$ can be determined by fitting the above equation to the experimental data (and using the known value of $g_{\mathrm{K,bulk}}$), see the blue lines in Figure 4.3. We find $g_{\mathrm{K,ion}}$ values of 1.6±0.1 and 1.0±0.2 for Na^+ and Cs^+, respectively. The smaller value for Cs^+ compared to Na^+ is due to a stronger propensity to break up the hydrogen-bond structure of water. This result is in line with previous investigations of the relation between water structure and ionic mobility,[142–145] which showed faster ionic diffusion in less structured hydrogen-bond environments. At high concentrations, the Hubbard-Onsager theory will also overestimate the amplitude of the kinetic depolarization because this theory does not include the Debye screening of the potential of the moving charge due to the dynamic repositioning of the other ions in the medium. We will not consider this effect here, but we hope that our experiments will stimulate further

experimental and theoretical work in this direction.

Using the modified Hubbard-Onsager equation, we can now decompose the observed (dilution-corrected) depolarization into its static and kinetic contributions in a well-defined manner. The result is shown in Figure 4.4, which also displays the kinetic depolarization predicted by the conventional Hubbard-Onsager equation (Eq. 4.5). Note that by subtracting the latter from the total depolarization one obtains a negative static depolarization for CsCl, which is not physically meaningful. Using the modified Hubbard-Onsager equation we obtain a positive (physically meaningful) static depolarization.

4.5 Discussion and conclusion

From the amplitude of the static depolarization we can directly estimate the number of water molecules that are rotationally immobilized per ion, i.e. the hydration number.[106] We obtain hydration numbers of 8.1±0.9 for Na^+ and 3.1±1.0 for Cs^+. These numbers agree well with previous estimates obtained using more indirect measurements.[152] Both for Na^+ and Cs^+ the hydration number (the number of rotationally immobilized water molecules) is different from the coordination number (the number of water molecules that in the first solvation shell: 6 and 8 for Na^+ and Cs^+ respectively).[18,153–156] This difference is a general phenomenon[106] which illustrates the importance of experimentally determining the hydration number.

To conclude, the observed isotope effect in the depolarization of ionic solutions indicates that water molecules surrounding ions reorient in a much less cooperative manner than in neat bulk water, with Kirkwood factors close to unity. Based on our observations we propose a modified Hubbard-Onsager equation that takes the locally reduced Kirkwoord factor into account, and that makes it possible to analyze the depolarization of ionic solutions in an unambiguous manner. This modified Hubbard-Onsager equation provides meaningful hydration numbers, which the conventional Hubbard-Onsager equation fails to do (in some cases even leading to unphysical results) because this expression overestimates the collective nature of water reorientation near ions. Our results thus provide new insights into the effect of ions on water cooperativity. The approach presented here enables a reliable determination of hydration numbers, which is of broad physical relevance, since hydration numbers are widely used to quantify the physical and chemical properties of aqueous solutions.

5

Accurate hydration numbers of alkali-metal ions using isotope-dependent dielectric relaxation

We measure the isotope-dependent dielectric deficiency (depolarization) in a series of alkali-metal chloride solutions to experimentally separate static and kinetic effects. The static depolarization is used to estimate hydration numbers. We obtain good agreement with the Hofmeister trend: Na^+, which is a small ion, forms a strong hydration complex that extends partially to its second coordination shell, whereas larger cations are poorly hydrated even in their first solvation shell. Using the amplitude of the kinetic depolarization, we observe that the cooperative character of water is reduced in the vicinity of ions. We find that water molecules near Cs^+ (structure breaker) behave in an uncorrelated manner as the result of a strong hydrogen-bond breaking effect. With decreasing the ion size, the system recovers its cooperative behavior, meaning more structured hydrogen-bond environments.

5.1 Introduction

The interaction between ions and water plays a key role in chemistry and (bio)physics, with examples ranging from ion transport in fuel cells and through membranes to the stability of protein solutions.[11,12,157–161] The hydration number is a frequently used, well-defined way to quantify the interaction between water and ions.[18] While the coordination number is the number of water molecules that fit in the first solvation shell, the hydration number is the number of water molecules that are tightly bound to an ion, more specifically the number of water molecules with residence times longer than the Debye relaxation time τ_D of water.[105,162] In spite of their appealing conceptual simplicity, hydration numbers are surprisingly difficult to determine experimentally, and the reported values vary significantly.

Dielectric-relaxation spectroscopy is perfectly suited to determine hydration numbers, as it is particularly sensitive to the immobilization of water molecules that hydrate ions.[33,163,164] The dielectric spectrum of water and aqueous solutions is dominated by the Debye relaxation of water,[93] and in electrolyte solutions the amplitude A_D of this Debye relaxation is reduced due to the rotational immobilization of water that is bound to ions. However, the observed decrease in amplitude (the depolarization, ΔA_D) cannot be translated directly into a hydration number, because it is due not only to the immobilization of ion-bound water (static depolarization[106]) but also to a kinetic effect:[93] ions moving in an externally applied electric field tend to reorient the surrounding water dipoles in a direction opposite to the applied field.[109,110,112,114] The observed depolarization is the sum of these two contributions: $\Delta A_D = \Delta A_{D,sta.} + \Delta A_{D,kin.}$ To determine the hydration number one needs $\Delta A_{D,sta.}$, but to separate the two contributions unambiguously is generally not straightforward. In Chapter 4, we showed that this problem can be addressed by using the isotope effect in ΔA_D. Here, we apply this method to obtain reliable experimental values for the hydration numbers of four alkali ions.

5.2 Experimental approach and results

We investigated MCl solutions (M = Na^+, K^+, Rb^+ and Cs^+) in the concentration range from 0 to 1 mol/l (see Appendix for details of the experiments and data analysis), and we determine the ionic conductivity σ and the depolarization ΔA_D (corrected for the decrease in water volume fraction with increasing concentration, see Appendix) for all solutions as a function of the ion concentration c. Figure 5.1 shows the results for the solutions in H_2O and D_2O. As expected, both the ionic conductivity and depolarization increase with increasing concentration. As observed previously,[36,45] $\sigma(c)$ and $\Delta A_D(c)$ are well described by $Dc - Ec^{3/2}$, the same functional form as Kohlrausch's law for dilute solutions.

For all solutions we observe significant isotope effects in σ and ΔA_D. Since

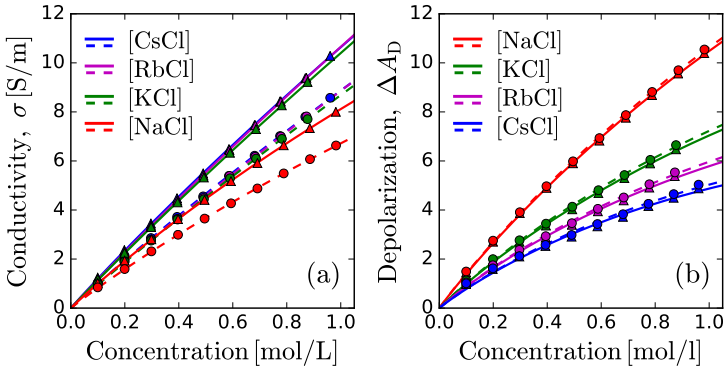

Figure 5.1. a) Conductivity σ as a function of concentration for four different alkali metal chloride solutions in H_2O and D_2O. b) Depolarization ΔA_D (corrected for the decrease in water volume fraction with increasing concentration, see Appendix) as a function of concentration for the same four solutions in H_2O (solid curves and triangles) and D_2O (dashed curves and circles).

$\Delta A_D = \Delta A_{D,sta.} + \Delta A_{D,kin.}$, this isotope effect arises from two contributions, one contribution arising from an isotope dependence in $\Delta A_{D,sta.}$ and the other from $\Delta A_{D,kin.}$ As explained in Chapter 4, the static contribution to the isotope effect in ΔA_D is negligible since the dipole moment of D_2O differs by only 0.06% from that of H_2O,[151] and so we have

$$\Delta A_D^{H_2O} - \Delta A_D^{D_2O} = \Delta A_{D,kin.}^{H_2O} - \Delta A_{D,kin.}^{D_2O} \tag{5.1}$$

Hence, the experimentally observed isotope effects in ΔA_D can be used to obtain reliable estimates for $\Delta A_{D,kin.}$[19] To do so, we adopt the analysis of the kinetic depolarization derived by Hubbard and Onsager[109,110] by including the effect of the ions on the hydrogen-bond cooperativity in their surroundings, as discussed in Chapter 4. This procedure allows us to determine not only the kinetic depolarization, but also to characterize the local hydrogen-bond cooperativity around the ions (which we will discuss in more detail below).[19] Using the values obtained for the kinetic depolariation, we determine the static depolarization by subtraction from the total depolarization. Figure 5.2a shows the concentration-dependent static depolarization for all solutions. The nonlinearity in the static depolarization as a function of concentration is due to the overlap of hydration shells at high concentrations.

From the amplitude of static depolarization, we obtain the hydration number

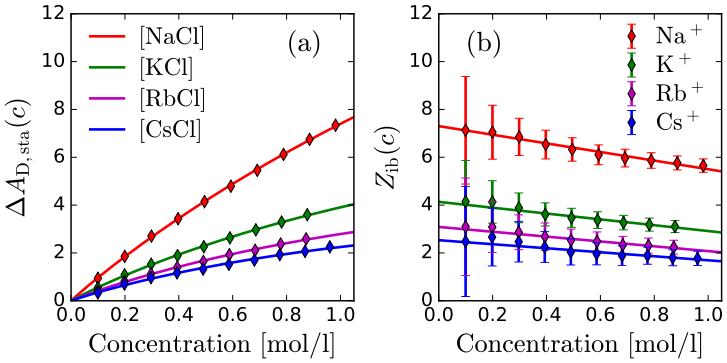

Figure 5.2. a) Static depolarization $\Delta A_{\mathrm{D,sta.}}$ as a function of the ionic concentration for four different alkali metal chloride aqueous solutions. b) Concentration dependence of the hydration number, Z_{ib}, for four alkali ions determined using Eq. 5.2.

Z_{ib} of the cations using (see Section 2.5):

$$Z_{\mathrm{ib}}(\mathrm{M}^+, c) = \frac{c_{\mathrm{w},0}}{A_{\mathrm{D},0}} \frac{\Delta A_{\mathrm{D,sta.}}(c)}{c}, \tag{5.2}$$

where $c_{\mathrm{w},0} = 55.32$ mol/l and $A_{\mathrm{D},0} = 73.17$ are the water concentration and the amplitude of the Debye dipole relaxation of neat water, respectively.[45] As discussed in Section 2.5, the contribution of the anions to the static depolarization is negligible.

Figure 5.2b shows effective hydration numbers obtained in this way for different concentrations. We find that the effective hydration number is slightly concentration-dependent, an effect that has been observed before and is extensively discussed in Ref. 165. From the limit of Z_{ib} as $c \to 0$ obtained from a least-squares fit to a linear relation between Z_{ib} and c, the hydration number can be determined.

5.3 Discussion

The hydration numbers obtained in this way are given in Table 5.1, together with the coordination numbers and the effective Kirkwood factors. Our values for the hydration numbers agree reasonably well with the values obtained previously using other methods (see the third column of Table 5.1).[152,162] The extent of hydration varies considerably with the ionic radius: for Na^+ we have $Z_{\mathrm{ib}}(7) \geq \bar{n}(6)$, so even some water molecules in the second coordination shell are immobilized by the ion,

Ion	$\bar{n}$	$Z_{\mathrm{ib,lit}}$	$Z_{\mathrm{ib}}(c=0)$	g_{ion}
Na^+	6	7–13	7.3(0.5)	1.62 ± 0.14
K^+	8	4	4.1(0.5)	1.28 ± 0.08
Rb^+	8	3	3.1(0.6)	1.18 ± 0.11
Cs^+	8	4	2.6(0.6)	0.97 ± 0.16

Table 5.1. Coordination numbers $\bar{n}$ [18,153,154,156,167] and hydration numbers $Z_{\mathrm{ib,lit}}$ [152,162] for alkali-metal ions in water reported in previous literature. Hydration numbers at infinite dilution Z_{ib} and effective Kirkwood correlation factors g_{ion} obtained in the present study.

whereas for Cs^+ we have $Z_{\mathrm{ib}}(3) < \bar{n}(8)$, so only part of the water molecules in the first coordination shell is immobilized. The hydration number increases with decreasing ionic radius, a well-known trend[40,152,166–168] that can be explained from the higher charge density of the small ions, which leads to stronger electrostatic attraction between the ion and the electronegative oxygen atom of the water molecules in the coordination shell.

For all ions, we observe an effective Kirkwood factor g_{eff} that is less than that of neat water, indicating a locally reduced cooperativity of the water reorientation dynamics. This is to be expected since the ions locally disrupt the tetrahedral hydrogen-bond network of water. Interestingly, the value of the effective Kirkwood factor increases with decreasing ionic radius, *i.e.* small cations reduce the cooperativity of water reorientation dynamics less strongly than large cations. This difference might be due to a strengthening of the water-water hydrogen bonds surrounding the smaller cations: by drawing electron density toward the oxygen atoms of the coordinating water molecules, cations polarize the coordinating water molecules, such that their dipole moment increases. As a consequence, the water molecules in the first coordination shell form hydrogen bonds to water molecules in the second solvation shell that are stronger than the hydrogen bonds between bulk water molecules. This effect can partly compensate the reduction in the Kirkwood factor due to the breaking up of the local tetrahedral hydrogen-bond structure by the cation; and since it will be stronger for the smaller cations (which have larger charge density), it could explain why for these cations the effective Kirkwood factor is less reduced than it is for the larger cations. Small cations thus show both a relatively large static depolarization and a relatively large kinetic depolarization effect in comparison to large cations, the latter because of the smaller reduction of the effective local Kirkwood factor.

5.4 Conclusion

To conclude, a systematic analysis of the isotope-dependent depolarization in electrolyte solutions has been performed to determine the solvation properties of alkali ions. We use the isotope effect to unambiguously separate the kinetic and static components of the depolarization, and then estimate hydration numbers. According to our observations, Na^+ has a well-defined hydration shell and forms a hydration complex that includes part of the second coordination shell. In contrast, larger cations are only partially hydrated even in their first solvation shell, which is apparently rather labile. Our work also provides experimental confirmation of the hydrogen-bond breaking effect in solvation shells, since we find that around an ion the cooperativity of the water dynamics is reduced. A complete description of this "structure-breaking" effect is challenging and goes beyond the scope of this experimental study. However, the effective Kirkwood factor introduced here may serve as a convenient parameter to quantify the "structure-breaking" capacity of an electrolyte.

6

Solvation structure and dynamics of hydronium and hydroxide in water investigated with isotope-dependent dielectric relaxation spectroscopy

We investigate the hydration of H_3O^+ and OH^- using the effect of these ions on the dielectric response of water. The presence of ions causes a reduction in the dielectric response (depolarization) of water due to a combination of static and kinetic effects. Using isotope-dependent measurements, we can separate these two contributions. From the static part of the depolarization, we estimate the number of water molecules immobilized by each dissolved H^+ (the hydration number) to be 4.9 ± 0.6. From the kinetic part, we obtain an estimate for the number of water molecules that reorient their dipole moment against the applied electric field as a consequence of the field-induced ion drift, a number that provides a lower bound to the number of water molecules involved in the ion transport. Interestingly, the kinetic depolarization is about three times larger for H_3O^+ than for OH^-, and the observed values correspond to 16 ± 2 and 5.5 ± 0.2 water molecules involved in the ion transport for H_3O^+ and OH^-, respectively.

6.1 Introduction

Since hydronium (H_3O^+) and hydroxide (OH^-) are ubiquitous in aqueous chemistry and play a role in nearly any biochemical process, the solvation and transport properties of these two ions in water form an active field of experimental and theoretical research.[73–81,169–171] In comparison with alkali and halide ions, H_3O^+ and OH^- exhibit anomalously high mobilities in aqueous solution. It is generally agreed that this mobility can be explained with the Grotthuss mechanism, in which the ions do not move as particles but only their charge is transferred via an interconversion of hydrogen and covalent bonds.[172–177] Although the concept of the Grotthuss mechanism is now well understood, many details of the solvation structure and the transfer dynamics of the protons and hydroxide ion in water, such as the number of water molecules involved in the solvation and transport, are still unclear.

Previous work has shown that dielectric relaxation spectroscopy is well suited to study the solvation of ions in water.[19,27,33,36,44,45,101,163,178] Upon the addition of ions to water, the amplitude of the dielectric response decreases (an effect referred to as depolarization). A trivial (and small) contribution to this effect arises from the dilution of the solvent,[93] but the main cause of the depolarization is the strong interaction of ions with water. Ions affect the orientational motion of the surrounding water molecules in two different ways: (i) the electrostatic interaction between the ionic charge and the dipole moments of the solvating water molecules causes irrotational binding of water molecules to the ions (referred to as static depolarization);[106] (ii) the drift of the ions due to the externally applied field causes a rotational response of the water molecules surrounding the ions, a process in which the water molecules reorient their dipole moments in a direction opposite to the applied field, thereby decreasing the overall dielectric response (referred to as kinetic depolarization).[109,110,112–114]

Separating the experimentally observed depolarization into its static and kinetic components is not straightforward. Often this separation is done by taking a calculated value for the kinetic depolarization, typically obtained with the Hubbard-Onsager (HO) model (or more sophisticated versions of this model).[110,112,116] However, this approach has its limitations, as illustrated by cases where the HO model predicts a kinetic depolarization that is larger than the experimentally observed total depolarization.[47] In these cases the kinetic depolarization is clearly overestimated by the HO model. In Chapter 4, we presented a solution to this problem: by using the isotope dependence of the dielectric spectrum, combined with an adaptation of the HO model to account for the reduced cooperativity (Kirkwood factor) of the water surrounding ions, we were able to obtain an experimental determination of the kinetic depolarization,[19] and thus to separate the depolarization into its static and kinetic parts in an unambiguous manner.

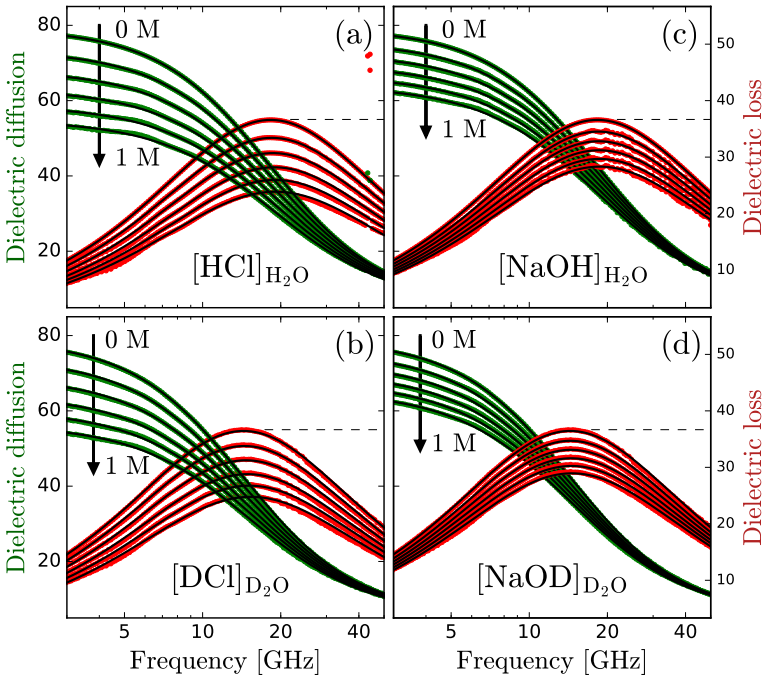

Figure 6.1. Complex dielectric spectra of $HCl:H_2O$ (a), $DCl:D_2O$ (b), $NaOH:H_2O$ (c) and $NaOD:D_2O$ (b) solutions in the concentration range of 0–1 M at 23°C. The green and red points represent the experimental data measured by DRS for dielectric diffusion, $\epsilon'(\omega)$, and dielectric loss, $\epsilon''(\omega)$, respectively. The solid black lines represent fits to the data following Eq.1. The effect of ionic conductivity has been subtracted for visual purposes. Extracted values for $\kappa(c)$ are displayed in Fig.6.2.a.

6.2 Experimental approach

Here, we use again the latter method to investigate the solvation of hydronium and hydroxide in water. We perform dielectric-spectroscopy measurements on a series of $XCl:X_2O$ and $NaOX:X_2O$ solutions (X = H,D), and use again the measurements for different isotopes to determine the static and kinetic depolarizations, which provides important information on the hydration structure and the transfer dynamics, respectively. The samples are prepared in a concentration range of 0–1 M by dilution of two commercially available solutions of 1.0 M NaOH and 40 wt% NaOD (Sigma-Aldrich) in H_2O (deionized water with a conductivity of 5.5 μS/m) and D_2O (99.96%), respectively. The dielectric-relaxation measurements are carried out in the spectral range of 1–50 GHz at 23°C using a gold-coated re-

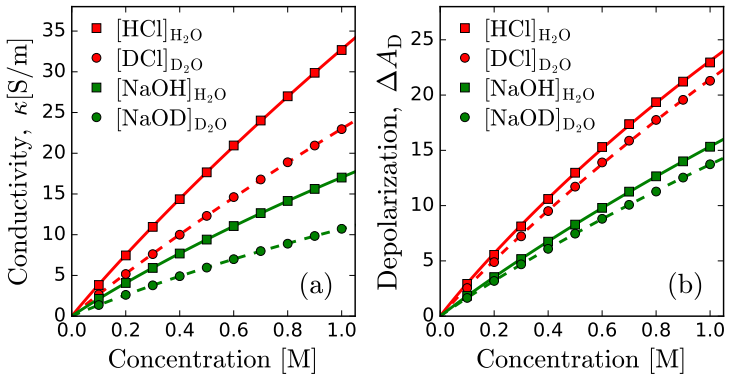

Figure 6.2. a) Ionic conductivity κ and b) depolarization ΔA_{D} both as a function of the solute concentration for four electrolyte solutions. Squares and circles indicate solutions prepared in H_2O and D_2O as solvent; red and green indicate acidic (XCl) and alkaline (NaOX) solutions, respectively, with X = H, D.

flectrometric cell together with a GHz phase-sensitivity vector network analyzer. Details of the experimental setup are presented in Chapter 2.

The complex dielectric spectra are analyzed by least-squares fitting a Cole–Cole relaxation model:

$$\hat{\epsilon}(\nu) = \epsilon_\infty + \frac{\epsilon_{\mathrm{s}} - \epsilon_\infty}{1 + (i2\pi\nu\tau_{\mathrm{D}})^{1-\alpha}} + \frac{\sigma}{i2\pi\nu\epsilon_0}, \tag{6.1}$$

where the amplitude of the dielectric relaxation process is defined as $A_{\mathrm{D}} = \epsilon_{\mathrm{s}} - \epsilon_\infty$, with ϵ_{s} the static permittivity and ϵ_∞ the limiting permittivity at high frequencies. ϵ_0 is the vacuum permittivity, τ_{D} the Debye relaxation time, σ the ionic conductivity, and α describes the broadening of the relaxation mode in the presence of ions. Neat water is well described by $\alpha = 0$, i.e. by a Debye relaxation mode. In the fits, ϵ_∞ is fixed to the value of pure water since it is practically independent of ionic concentration.[86,117]

6.3 Partitioning the experimentally observed depolarization

Figure 6.1 shows the complex dielectric spectra of the investigated solutions. The conductivity contribution has been subtracted for clarity, and the observed values for $\sigma(c)$ are shown in Figure 6.2a. The solid black lines in Figure 6.1 represent fits of Eq. 6.1 to the experimental data. Figure 6.1 shows that the addition of ions reduces the amplitude of the dielectric response as compared to that of the pure

solvent. The dilution-corrected depolarization is

$$\Delta A_{\mathrm{D}} = A_{\mathrm{D,n}} - A_{\mathrm{D}}, \tag{6.2}$$

where $A_{\mathrm{D,n}}$ is the water-concentration-corrected amplitude of the dielectric response, which is given by

$$A_{\mathrm{D,n}} = \frac{c_{\mathrm{w}}(c)}{c_{\mathrm{w,0}}} A_{\mathrm{D,0}}, \tag{6.3}$$

with $c_{\mathrm{w}}(c)$ the concentration of water (which decreases upon the addition of ions), and $A_{\mathrm{D}}(0)$ the dielectric response of the pure solvent. In this equation it is assumed that the dielectric response scales with the density of molecules which is a valid assumption in the context of the Onsager model for the dielectric response of dipolar molecules and in the limit that $\epsilon_s \gg \epsilon_\infty$ (see Section 2.5). Figure 6.2b shows the dilution-corrected depolarization, which is due purely to the interaction between the ions and the water molecules. The concentration-dependent depolarization has a significant isotope effect, which implies that the kinetic depolarization is large (see below). As was found previously,[45] the depolarization and the ionic conductivity can be well fitted using a function $f(c) = Bc - Cc^{3/2}$, where the C-parameter represents the non-linearities in σ and ΔA_{D} due to the overlap of solvation shells at high concentration.

As discussed in Chapter 4 we can separate the kinetic and static contributions to the depolarization using the isotope difference $\Delta A_{\mathrm{D}}^{\mathrm{H_2O}} - \Delta A_{\mathrm{D}}^{\mathrm{D_2O}}$. Figure 6.3 shows this isotope effect for acidic and alkaline solutions. Since the permanent dipole moments of H_2O and D_2O are identical to within 0.06%,[151] the static contributions to the depolarization are the same in H_2O and D_2O solutions, so we have

$$\Delta A_{\mathrm{D}}^{\mathrm{H_2O}} - \Delta A_{\mathrm{D}}^{\mathrm{D_2O}} = \Delta A_{\mathrm{D,kin}}^{\mathrm{H_2O}} - \Delta A_{\mathrm{D,kin}}^{\mathrm{D_2O}}, \tag{6.4}$$

i.e., the experimentally observed isotope effect is only due to the difference in kinetic depolarization in H_2O and D_2O.

Equation 6.4 allows us to estimate the magnitude of the kinetic depolarization experimentally, in a similar way as in Chapter 4. There, we found that the Hubbard-Onsager equation for the kinetic depolarization (Eq. 2.39 in Chapter 2) overestimates the kinetic depolarization, and that the discrepancy could be resolved by replacing the Kirkwood factor by an effective Kirkwood factor for the water surrounding the ions.

In the experiments of this chapter, the situation is more complicated: the Hubbard-Onsager equation assumes spherical ions, and for H_3O^+ and OH^- this is not correct. However, it turns out that using the reasonable assumption that $\Delta A_{\mathrm{D,\,kin}}$ is still proportional to the conductivity and the water reorientation time:

$$\Delta A_{\mathrm{D,kin}} = \xi \sigma(c) \left[\frac{\tau_{\mathrm{D}}}{\epsilon_0} \left(\frac{\epsilon_s - \epsilon_\infty}{\epsilon_s} \right) \right], \tag{6.5}$$

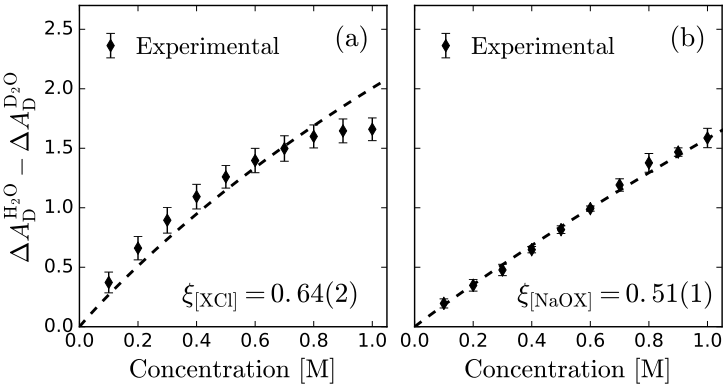

Figure 6.3. Depolarization difference between reciprocal isotope solutions as a function of solute concentration. a) The isotope effect in acidic (XCl) solutions. b) The isotope effect in alkaline (NaOX) solution. The diamonds represent the experimental results. The dashed curves represent the fits using Eqs. 6.4 and 6.5.

we can still obtain quantitative information from our data. In this equation, ξ is a scaling factor which can be different for each cation/anion combination. For solutions in which the cation and anion are both spherical (as in Chapters 4 and 5), we have $\xi = pg_{\text{ion}}/g_{\text{bulk}}$ with $p = 2/3$,[45,106,109,110,112] and $g_{\text{ion}}/g_{\text{bulk}}$ the effective Kirkwood factor which accounts for reduced cooperativity of the water reorientation in the neighborhood of the ions.

Substituting Eq. 6.5 into Eq. 6.4 and least-squares fitting the resulting expression to the experimentally observed $\Delta A_{\text{D}}^{\text{H}_2\text{O}} - \Delta A_{\text{D}}^{\text{D}_2\text{O}}$, we find ξ values of 0.64 ± 0.02 and 0.51 ± 0.01 for HCl and NaOH solution, respectively (see Figure 6.3 for the resulting least-squares fit). As a first application of these numbers, we can decompose the observed total depolarization (corrected for dilution) into its static and kinetic parts. From the static part we can estimate the hydration numbers, in the same way as in Chapters 4 and 5. We find hydration numbers of 4.9 ± 0.6 for H^+ and 6.5 ± 0.2 for Na^+ (assuming that the anions contribute negligibly to the static depolarization).[18,27,45,105,106] The hydration number of Na^+ is similar to that found in Chapter 5, while the hydration number of H_3O^+ agrees with the estimate obtained from Terahertz time-domain spectroscopy,[115] and suggests that the proton in water exists mostly as an Eigen ($H_9O_4^+$) complex, as has also been found in DFT-based molecular dynamics simulations.[179]

Going one step further, we can partition the kinetic depolarization into contributions of the cation and the anion. If we assume that the kinetic depolarization is the sum of a cationic and anionic contribution:

$$\Delta A_{\text{D,kin}} = \Delta A_{\text{D,kin}}^{+} + \Delta A_{\text{D,kin}}^{-}, \tag{6.6}$$

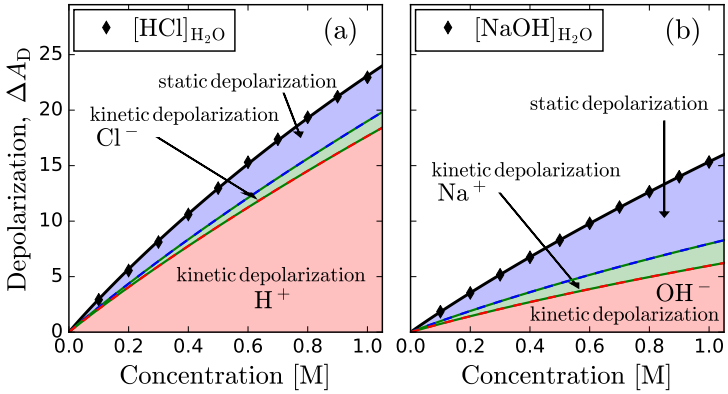

Figure 6.4. Experimentally observed depolarization of HCl:H_2O (a) and NaOH:H_2O (b) solutions. The depolarization is decomposed into its static and kinetic contributions. The kinetic depolarization is partitioned in the independent contributions of cations and anions.

we can obtain the kinetic depolarization of the proton and hydroxide ion by subtracting an estimate of the contributions of the counter ions (Cl^- and Na^+ respectively) from the total kinetic depolarization. In Chapter 4 we found that for solutions of spherical ions we have

$$\Delta A_{\mathrm{D,kin}} = \frac{2}{3}\frac{g_{\mathrm{ion}}}{g_{\mathrm{bulk}}}\sigma(c)\left[\frac{\tau_{\mathrm{D}}}{\epsilon_0}\left(\frac{\epsilon_s - \epsilon_\infty}{\epsilon_s}\right)\right]. \tag{6.7}$$

The factor $g_{\mathrm{ion}}\sigma(c)$ in this expression is due to the cation and anion, and we assume that it can be split up into a term associated with the kinetic depolarization of the cation and a term representing the kinetic depolarization of the anion:

$$g_{\mathrm{ion}}\sigma(c) = g^+_{\mathrm{ion}}\sigma^+(c) + g^-_{\mathrm{ion}}\sigma^-(c), \tag{6.8}$$

with $\sigma^{+/-}$ and $g^{+/-}_{\mathrm{ion}}$ the ionic conductivities and effective Kirkwood factors of the cation and the anion. This is expected to be a reasonable assumption at not too high salt concentrations. It would seem difficult to obtain the individual contributions to the right-hand side of Eq. 6.8, since there are two unknowns, g^+_{ion} and g^-_{ion}. However, the value of g^-_{ion} of Cl^- can be estimated from the results obtained for CsCl. For this solution, the observed g_{ion} is extremely low, and the fact that g cannot be less than 1 can be used to obtain a unique solution as follows. Using the transport number λ (the fraction that an ion contributes to the total ionic conductivity of a solution) of each of the ions,[180,181] we can calculate the individual ionic conductivities as $\sigma^{+/-} = \lambda^{+/-}\sigma$. In CsCl solution, the effective

correlation factor is $g_{\text{ion}} = 1.0 \pm 0.2$ (see Chapter 4) and the transport numbers are $\lambda_{\text{Cs}} \approx \lambda_{\text{Cl}} \approx 0.5$, leading to $g_{\text{ion}}^{\text{Cs}^+} \approx g_{\text{ion}}^{\text{Cl}^-} \approx 1$. Note that this solution is unique, since all other mathematically possible solutions have one g value below 1, which is unphysical. The value $g_{\text{ion}}^{\text{Cl}^-} \approx 1$ can now be used to determine $g_{\text{ion}}^{\text{Na}^+}$ from the experimentally observed effective correlation factor $g_{\text{ion}} = 1.6$ of NaCl solution (see Chapter 4). We again split up g_{ion} as in Eq. 6.8, and use the known transport numbers λ of Na^+ and Cl^- to calculate $\sigma^{\text{Na}^+}(c)$ and $\sigma^{\text{Cl}^-}(c)$; since we know $g_{\text{ion}}^{\text{Cl}^-}$ the only unknown is $g_{\text{ion}}^{\text{Na}^+}$, and solving the equation we obtain $g_{\text{ion}} = 2.6$ for Na^+. The values of $g_{\text{ion}}^{\text{Cl}^-}$ and $g_{\text{ion}}^{\text{Na}^+}$ can now be used to calculate the contribution of Cl^- and Na^+ to the total kinetic depolarization in HCl and NaOH solution. Figure 6.4 shows the resulting decomposition of the total depolarization into its individual contributions.

6.4 Discussion and conclusion

The kinetic depolarization contributions of H^+ and OH^- reflect the number of water molecules participating in the depolarization induced by the motion of these ions (just as the magnitude of $\Delta A_{\text{D,sta.}}$ can be translated to a the number of water molecules immobilized by an ion). The large kinetic depolarization caused by H^+ ions indicates that a large number of water molecules are affected by proton transport through water, in line with previous theoretical investigations on proton transport.[182] From the amplitude of the kinetic depolarization caused by H_3O^+, we estimate that ∼16 water molecules are affected due to H^+ charge diffusion. This result is in line with previous theoretical investigations on proton transport that reported that H^+ has a strong influence over water molecules beyond its first solvation shell.[182] Similarly, we find that the charge diffusion of OH^- affects at least 5 water molecules, which is significantly smaller than the number of water molecules affected by the diffusion of the proton.

To conclude, we have shown that the isotope effect in the dielectric depolarization of aqueous H_3O^+ and OH^- solutions can be used to investigate their solvation properties. From the static depolarization of H_3O^+ solution, we obtain an estimate for the number of water molecules that are rotationally immobilized by this ion. From the kinetic depolarizations, we can estimate a lower bound for the number of water molecules that are involved in the transport of H_3O^+ and OH^-. Interestingly, this number is much higher for H_3O^+ than for OH^-. It should be possible to predict these numbers from DFT-based simulations, and we hope that our results will stimulate work in this direction.

7

Slowing down of the molecular reorientation of water in alkaline solutions*

It is generally accepted that the hydroxide ion (OH^-) is a strong hydrogen bond acceptor and that its anomalously high diffusion in water results from a Grotthuss-like structural diffusion mechanism. However, the extent over which OH^- ions influence the dynamics of the hydrogen-bond network of water is not yet clear. Here we measure the ultrafast dynamics of OD/OH groups of HDO molecules interacting with OH^-/OD^- ions. For solutions with OH^-/OD^- concentrations up to 4 M, we find that HDO molecules that are not directly interacting with the ions, have a reorientation time constant of ~ 2.6 ps, similar to pure liquid water. When the concentration of OH^-/OD^- ions is increased, the reorientation time constant increases, indicating a slowing down of the structural dynamics of the solution.

This chapter is based on: Roberto Cota, Eliane P. van Dam, Sander Woutersen and Huib J. Bakker, *Slowing down of the molecular reorientation of water in concentrated alkaline solutions*, J. Phys. Chem. B **2020**, Accepted for publication.

7.1 Introduction

Proton transfer via hydronium (H_3O^+) and hydroxide ions (OH^-) is of fundamental and technological relevance in many chemical and physical processes, ranging from acid-base reactions to proton conducting membranes.[2,34,183–192] Compared to other ions that are well described by a Stokes mass diffusion mechanism, H^+ and OH^- ions exhibit an anomalously high mobility in aqueous solutions. This high mobility has been explained from an ongoing exchange between hydrogen bonds and covalent bonds, leading to charge transfer, the so-called Grotthuss mechanism.[173] The molecular-scale details of this mechanism remains an active field of experimental and theoretical research to date.[64,73,81,169–171,179,193–197]

Interestingly, the hydrated proton (H_3O^+) has been the subject of many experimental investigations,[74] whereas experiments on aqueous hydroxide ions are scarce. One reason for this apparent lack of interest is the notion that the diffusion of aqueous hydroxide ions has long been believed to be the mirror image of that of aqueous H_3O^+ ions, showing similar structural solvation topologies such as the Eigen structure $H_7O_4^-$ ($HO^- \cdots 3H_2O$) and the Zundel structure $HO^- \cdots H \cdots OH$.[198,199]

However, over the last decades many molecular dynamics simulations indicated that the transfer of aqueous hydroxide ions involves mechanisms that differ from those of the aqueous proton.[75–81] For instance, these simulations have shown that hydroxide ions can form hypercoordinated structures in which the oxygen atom of OH^- is coordinated by four water molecules. This structure was found to be quite stable thereby impeding the further transfer which could be part of the reason why OH^- ions diffuse slower than H_3O^+ ions.[81] Up to now, conclusive experimental evidence for this hypercoordinated structure has not been provided.

Ultrafast mid-infrared spectroscopy is a powerful technique to study molecular structures and inter- and intra-molecular interactions with a time resolution down to tens of femtoseconds, thus very well suited to investigate hydrogen-bond dynamics that occur on time scales on the order of (sub)picoseconds. Recently, this technique has been used to study the diffusion and structural rearrangement of OH^- ions in NaOH (and NaOD) solutions.[69–72] By probing the dynamics of OH groups that directly interact with the OH^- ions, it was found that the transfer of the hydroxide charge is relatively slow, with a lower bound of 3 ps, compared to the time scale <2 ps that has been observed for H_3O^+ ions.[171,194] While these experimental studies provided information on the rate and mechanism of the OH^- ions transfer in aqueous media, the influence of the OH^- ions on the dynamics of the hydrogen-bond network of water remains practically unexplored.[28,200]

The reorientation dynamics of water molecules in aqueous solution can be well studied with polarization-resolved femtosecond vibrational spectroscopy.[59,60,115,201,202] In this technique, the reorientation dynamics of a vibrationally excited OH or OD group of a HDO molecule in isotopic dilution (OD in H_2O or OH in D_2O) is measured. Irrespective whether the OH or OD group is probed, the measured

reorientation dynamics are representative for the dynamics of all water molecules present in solution. For the study of the dynamics of water in hydroxide solutions, the two isotopic alternatives both have their advantages and disadvantages. The OD vibration of HDO dissolved in H_2O has as an advantage that its excitation lifetime, $T_{1,\mathrm{OD}} = 1.8$ ps, is significantly longer than that of OH, $T_{1,\mathrm{OH}} = 0.7$ ps.[25,26,203] However, probing the OD vibration has as a disadvantage that its OD stretch vibration (~ 2500 cm^{-1}) overlaps with the broad continuum absorption of OH of H_2O that have strong solvation interactions with the hydroxide ions. As shown by Figure 7.1 this continuum starts to dominate over the absorption of the OD stretch vibration at OH^- concentrations above 3 M. In this respect, the OH vibration in D_2O is the best choice since it is spectrally well isolated from the continuum that results from the interaction of D_2O with OD^-. On the other hand, its relatively fast relaxation implies that its reorientation can only be followed over a limited time interval ($\approx$5 times T_1). Here, we present a complementary study of the reorientation dynamics of water molecules in a series of sodium hydroxide solutions both measuring the dynamics of OD in H_2O or OH in D_2O.

7.2 Experimental

We performed polarization-resolved femtosecond mid-infrared transient absorption measurements on the OD- and OH-stretch vibration of HDO molecules isotopically diluted in aqueous NaOH and NaOD solutions. The pump-probe setup used for these experiments is described in Chapter 3. As has been described in Section 3.5, we use the experimentally obtained parallel and perpendicular transient absorption signals to construct the anisotropy:

$$R = \frac{\Delta\alpha_{\parallel} - \Delta\alpha_{\perp}}{\Delta\alpha_{\parallel} + 2\Delta\alpha_{\perp}}, \tag{7.1}$$

where the denominator is the isotropic signal:

$$\Delta\alpha_{\mathrm{iso}} = \frac{1}{3}\left[\Delta\alpha_{\parallel} + 2\Delta\alpha_{\perp}\right]. \tag{7.2}$$

7.3 Results

7.3.1 Linear infrared spectra

We prepared hydroxide solutions by diluting commercially available solutions of 50 wt% NaOH and 40 wt% NaOD (Sigma-Aldrich products) in H_2O (deionized water with a conductivity of 5.5 μS/m) and D_2O (99.96%), respectively. We added HDO keeping the OD:OH (or OH:OD) ratio constant at 4% for all studied solutions. The

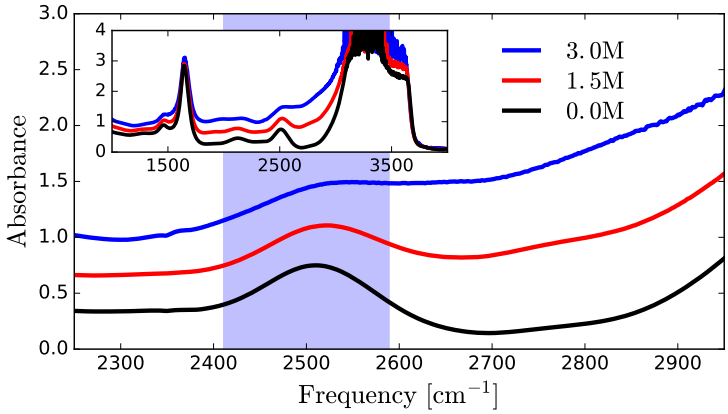

Figure 7.1. Linear IR spectra of 8% HDO isotopically diluted in NaOH:H_2O solutions at three different concentrations. The peak centered at 2500cm^{-1} corresponds to the OD stretch vibration of HDO molecules which donate hydrogen bonds to other HDO or H_2O. This vibration is referred as bulk-like water. The high frequency wing is assigned to H_2O molecules that form strong hydrogen bonds with OH^- ions. The background-like absorption increase, shown in the inset, is caused by the concentration-dependent broadband continuum spectrum of the hydrated hydroxide ions. The purple shaded bar indicates the region where transient absorption was recorded.

sample cell consists of two parallel CaF_2 windows separated by a Teflon spacer of 25 μm (1–3 mol/l NaOH solutions), 10 μm (4–6 mol/l NaOH solutions) and 50 μm (1–10 mol/l NaOD solutions).

In Figure 7.1 we present linear IR spectra of NaOH:H_2O solutions. All spectra show an absorption band at 2510 cm^{-1} corresponding to the OD stretch vibration of HDO molecules. At higher frequency a broad red wing of the absorption of the OH-stretch band centered at 3400 cm^{-1}. This wing overlaps with the absorption band of the OD stretch vibration. This broad response is assigned to hydroxide-associated OH groups of HDO and H_2O molecules, and will be referred to as hydrated complexes. The inset in Figure 7.1 shows the complete infrared absorption spectrum, illustrating the rise hydroxide continuum with increasing OH^- concentration. Notice that the OH stretch vibration is negligibly affected by Na^+ ions since water molecules do not form hydrogen bonds with cations.

Figure 7.2 displays the linear absorption spectra of NaOD:D_2O solutions. The main band around 3400 cm^{-1} is assigned to the OH stretch vibration. With increasing OD^- concentration, a shoulder at lower frequencies rises that is assigned to OH groups of HDO molecules forming strong hydrogen bonds to OD^- ions. There is also a weak shoulder in the blue wing at 3600 cm^{-1} that also rises with

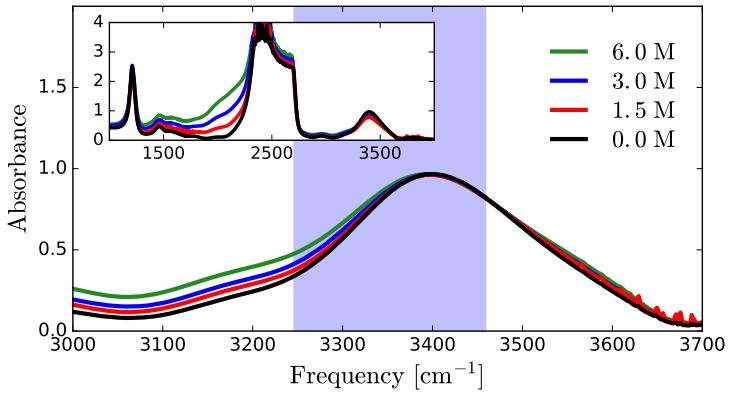

Figure 7.2. Linear IR spectra of 8% HDO isotopically diluted in NaOD:D_2O solutions at four different concentrations. The spectra are normalized to the maximum of the OH stretch peak at 3400 cm^{-1} in neat D_2O. The low frequency shoulder is assigned to OH groups of HDO molecules that form strong hydrogen bonds with OD^- ions, while the high frequency shoulder OH^- ions that are weak hydrogen-bond donors. The inset shows a deuteroxide continuum far from the OH spectral region. The purple shaded bar indicates the region where transient absorption was recorded.

increasing OD^- concentration. This shoulder is attributed to the stretch vibration of OH^- ions that are weak hydrogen-bond donors. The inset in Figure 7.2 shows that the vibrations around 3400 cm^{-1} are all spectrally well isolated from the continuum arising from the interactions of the abundant D_2O molecules with OD^- ions.

7.3.2 Vibrational relaxation dynamics

Figure 7.3 shows isotropic transient absorption spectra measured for the OD (left) and OH (right) stretch vibrations at different delays for different OH^-/OD^- concentrations. We only show spectra from delays of 0.4 ps onwards as the earlier time spectra show effects of spectral diffusion[204] and coherent coupling effects of the pump and probe pulses. The transient spectra are dominated by the bleaching of the fundamental $|0\rangle \rightarrow |1\rangle$ transition. The induced absorption of the $|1\rangle \rightarrow |2\rangle$ transition is only observed for a few experimental points at low frequencies.[25] The NaOD solutions (right panel of Figure 7.3) show significantly faster relaxation dynamics than the NaOH solutions (left panel of Figure 7.3), as could have been expected from the faster relaxation of the OH stretch vibration of HDO, compared to that of the OD stretch vibration of HDO.

At long delay times, the vibrational excitation has relaxed and has thermalized over the focus of the sample leading to a heating effect. This heating leads to

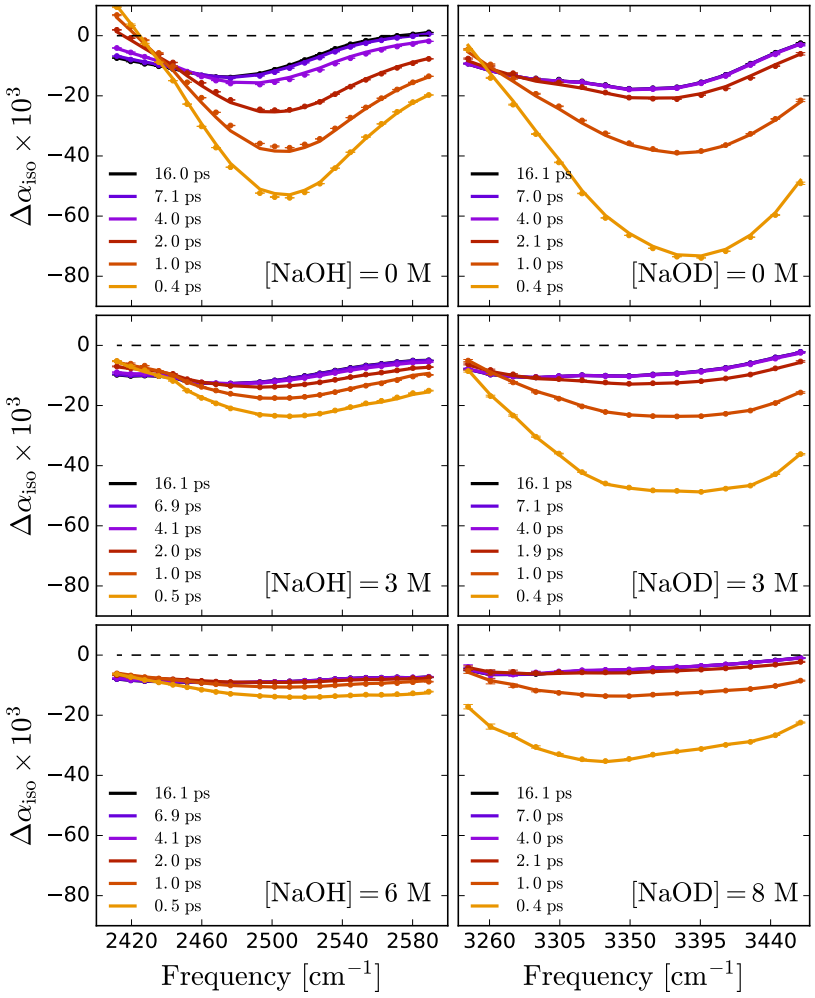

Figure 7.3. Transient spectra of aqueous solutions of NaOH in H_2O (left) and NaOD in D_2O (right) at 0, 3 and 6 mol/l concentrations. All samples contain 8% HDO. The dots indicate the experimental data, while solid lines are fits to the relaxation models described in the text.

a decrease and blueshift of the absorption spectrum of the OD/OH vibration, which corresponds to a long-living bleaching effect in the red wing of the transient absorption spectra of Figure 7.3.

To model the vibrational dynamics of NaOH:H_2O solutions, shown in the left

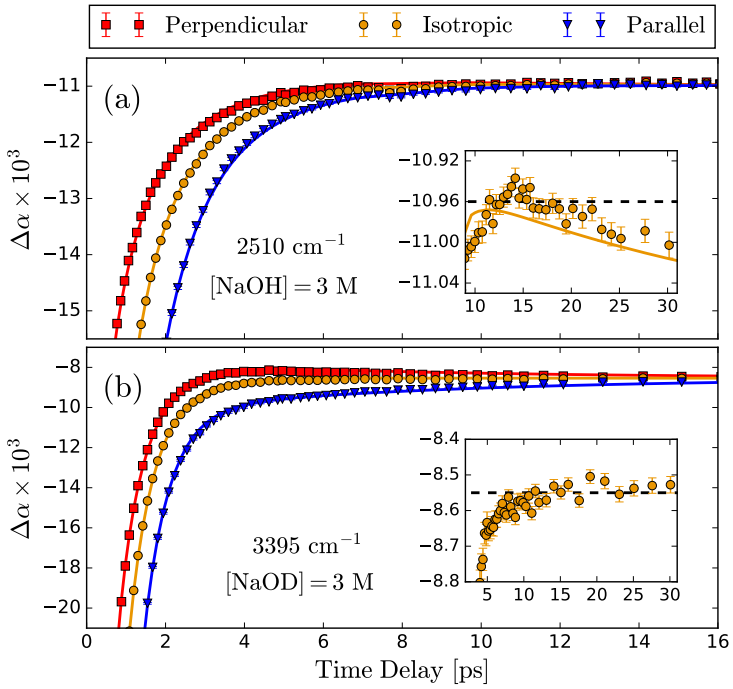

Figure 7.4. Parallel (blue), isotropic (yellow) and perpendicular (red) absorption change $\Delta\alpha$ as a function of delay time following the excitation of the OH vibration of HDO in 3 M [NaOD]:D2O and [NaOH]:H2O solutions. The insets zoom in the isotropic signal at long delay times. The solid lines are fits to the models presented in the text.

panel of Figure 7.3, it has to be realized that at $t = 0$ ps both bulk and ion-associated hydroxyl groups are excited. The first species, the OD groups in the bulk, is described with a monoexponential decay to a hot ground state, as shown in recent studies on salt solutions.[31,59] For the second species, we make use of the acquired knowledge from previous research on the dynamics of OH^- complexes.[205] This study showed that the transient signal of OH^- complexes can be well modeled with a 3-state consecutive kinetic model in which the excited state decays rapidly ($T_{1,\text{ion}}$ ~200 ps) leading to a locally heated hydration complex. Subsequently, the energy is homogeneously distributed, i.e. the locally hot state relaxes to the hot ground state. An interesting aspect in our experimental data is the (anomalous) behavior of the transient signal as from 15 ps, as displayed in the inset of Figure 7.4.a. The (negative) transient absorption signal reaches a minimum at a delay of ~15 ps and then increases by ~1.5% to reach its final amplitude at late

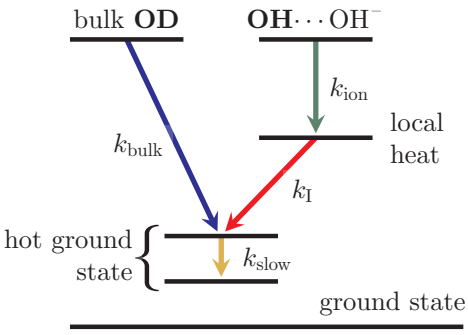

Figure 7.5. Schematic energy level diagram of the model that describes the vibrational dynamics of hydroxyl groups around 2500 cm^{-1}. Solid arrows indicate the channels for vibrational relaxation, while dashed arrow represent the additional channels that resonant energy transfer lead. The features of the model are described in the main text.

delays. This effect is probably due to a slow restructuring of the solution. We describe this process as an exponential decay.

Based on the above considerations we construct the kinetic model shown in Figure 7.5, comprising the different states described above. The populations of the different states, $N(t)$, depend on the transitions between the different components, and are constructed through a set of differential equations given by

$$\frac{d}{dt}N_j(t) = K_{ji}N_i(t), \tag{7.3}$$

where the rate matrix K_{ji} contains the transition rates and portrays the governing kinetic model.

The kinetic model has two parallel pathways that decay at different rates k_{bulk} and k_{ion}, respectively, and an intermediate state with decay rate k_{I} associated with the locally hot complexes. The final slow increase of the hot ground state response by $\sim$1.5% is described with a rate constant k_{slow}. The rate matrix is written as:

$$K_{ji}^{\text{OD}} = \begin{bmatrix} -k_{\text{bulk}} & 0 & 0 & 0 & 0 \\ 0 & -k_{\text{ion}} & 0 & 0 & 0 \\ 0 & +k_{\text{ion}} & -k_{\text{I}} & 0 & 0 \\ +k_{\text{bulk}} & 0 & +k_{\text{I}} & -k_{\text{slow}} & 0 \\ 0 & 0 & 0 & +k_{\text{slow}} & 0 \end{bmatrix}, \tag{7.4}$$

with each k associated with a time constant T, i.e. $T = 1/k$.

To compare the model with the data we need to associate a transient spectral

response $\Delta\sigma_i(\omega)$ with each level:

$$\Delta\alpha_{\mathrm{iso}}(t,\omega) = \sum_{i=1}^{m} N_i(t) \cdot \Delta\sigma_i(\omega), \tag{7.5}$$

where m is the number of levels.

By combining Eqs. 7.3–7.5 the rate constants and the spectral components can be calculated via a least-square minimization process. To restrict the number of free parameters we investigate some aspects in a independent experiment. For the description of NaOH:H_2O solutions, shown in Figure 7.3-left, we first perform experiments where no HDO was added. We find that the relaxation time, $1/k_{\mathrm{ion}} = T_{\mathrm{ion}}$ ~150 fs, and the spectral component, $\Delta\sigma_{\mathrm{ion}}$, of the initially excited ion-associated OH vibration shows no concentration dependence, as reported previously.[205] For all the solutions, the spectrum of the hot ground state is extracted at late delay times, $t \gg T_{\mathrm{bulk}}, T_{\mathrm{ion}}, T_{\mathrm{I}}$, where thermal equilibrium is attained. Hence, in the full modeling of our experimental data, three spectra ($\Delta\sigma_{\mathrm{ion}}$, $\Delta\sigma_{\mathrm{hgs}}$ and $\Delta\sigma_{\mathrm{slow}} \approx 1.015 \cdot \Delta\sigma_{\mathrm{hgs}}$) and the fast decay rate k_{ion} are fixed in the iterative least-square fitting process. The fitting yields the two remaining spectral traces, $\Delta\sigma_{\mathrm{bulk}}$ and $\Delta\sigma_{\mathrm{I}}$, and the rate constants, k_{bulk}, k_{I} and k_{slow}, that best fit the experimental data. Figure 7.6 shows the results of the spectral decomposition of the transient absorption spectrum measured at 0.58 ps delay time for a solution of HDO and 3 M NaOH in H_2O. We find that the spectra of the intermediate state $\Delta\sigma_{\mathrm{I}}$, i.e. the spectral response of the locally heated hydration complexes, and the hot ground state $\Delta\sigma_{\mathrm{hgs}}$ are quite similar in shape.

We find that the decay rate of the intermediate hot complexes k_{I} is concentration independent and corresponds to a time constant of 0.5±0.1 ps. This indicates that the vibrational relaxation of the OH group solvating OH^- ions is indeed a local process that is negligibly influenced by the outer hydrogen-bond network. The slow increase of transient signal after 15 ps, corresponds to a time constant of around 40 ps.

The relaxation time constant of the bulk OD vibrations is found to decrease linearly from 1.8±0.2 ps (similar to that reported in neat water) at 1 M to 1.4±0.2 ps for a concentration of 6 M. This acceleration can be explained from the presence of an additional relaxation channel for the OD vibrations resulting from the presence of hydrated hydroxide ions. The OH groups solvating the OH^- ions are in near resonance with the OD vibrations and the excitation energy of the OD vibrations can be taken up by the OH vibrations via Förster energy transfer.[31]

The modeling of the relaxation of the reciprocal system, i.e. HDO dissolved in NaOD:D_2O solutions is somewhat simpler as the OH vibrations of HDO are spectrally well isolated from the OD groups solvating the OD^- ions. However, also in this case two excited and relaxation species can be distinguished, as the addition of OH^- ions gives rise to an additional band centered at 3340 cm^{-1}. This latter

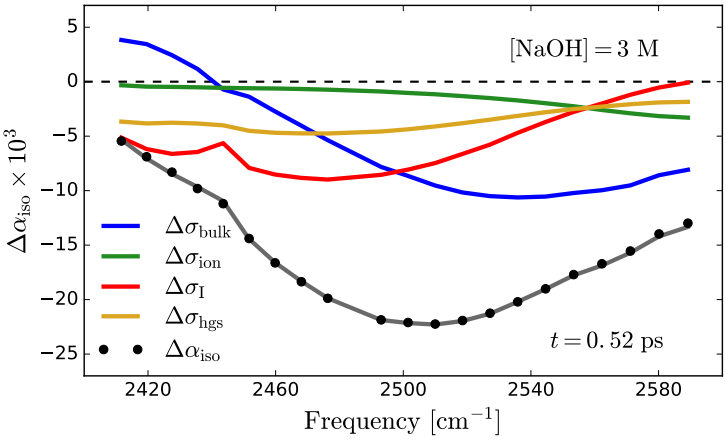

Figure 7.6. Spectral decomposition of the transient absorption spectrum measured at 0.58 ps delay time for a solution of HDO and 3 M NaOH in H_2O. The black circles represent the raw experimental data, and the gray curve results from a least-square optimization of the model given by Eqs. 7.3–7.5 to the data. The different spectral components are indicated with colors.

band can be assigned to OH groups solvating OD^- ions. We thus consider the excitation and relaxation of bulk-like OH vibrations and of OH vibrations solvating OD^- ions. Previous studies have shown that the thermal effect that follows the relaxation of the OH stretch vibration is often somewhat retarded.[26,206] This delay has been explained from the relatively slow adaptation of the hydrogen-bond network to the fast local energy dissipation induced by the vibrational relaxation. In contrast to the experiments on the OD vibrations the isotropic signal shows a negligible further evolution after 5 ps, as shown in the inset of Figure 7.4.b. This notion implies that there is no further slow structural relaxation affecting the transient absorption signal.

Based on the above considerations we arrive at the kinetic model shown in Figure 7.7. This model comprises two initially excited OH species that relax via an intermediate state to a hot ground state. The corresponding rate matrix is:

$$K_{ji}^{\mathrm{OH}} = \begin{bmatrix} -k'_{\mathrm{bulk}} & 0 & 0 & 0 \\ 0 & -k'_{\mathrm{ion}} & 0 & 0 \\ +k'_{\mathrm{bulk}} & +k'_{\mathrm{ion}} & -k_* & 0 \\ 0 & 0 & +k_* & 0 \end{bmatrix}, \tag{7.6}$$

with k'_{bulk} and k'_{ion} the decay rates of bulk and ion-associated OH vibrations, respectively. The primed rate constants are used to distinguish the properties of the

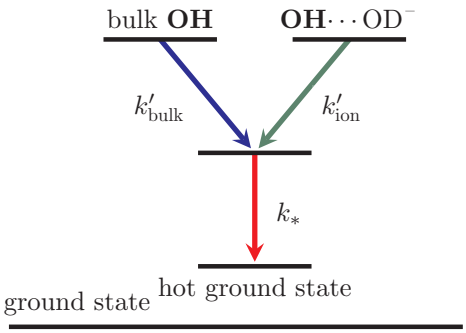

Figure 7.7. Schematic energy level diagram of the model that describes the vibrational dynamics of hydroxyl groups around 3400 cm^{-1}. Solid arrows indicate the channels for vibrational relaxation. The intermediate step represents the delayed adaptation of the hydrogen-bond network to the resulting vibrations from the fast relaxation process. The features of the model are described in the main text.

two isotope compositions. The intermediate component has no associated transient spectrum and k_* thus only serves to describe the retarded rise of the response of the hot ground state.

To model the data of the right panel of Figure 7.3 we combine Eqs. 7.3, 7.5 and 7.6. Again, the spectrum of the thermal ground state is extracted from the spectra at late delay times, and an iterative least-square minimization process is applied to extract the remaining unknown spectral traces, $\Delta\sigma'_{\mathrm{bulk}}$ and $\Delta\sigma'_{\mathrm{ion}}$ and the decay rates. Figure 7.8 shows the results of the spectral decomposition of the transient absorption spectrum measured at 0.45 ps delay time for a solution of HDO and 3 M NaOD in D_2O. The spectral components comprise the well-resolved $\Delta\sigma'_{\mathrm{bulk}}$, and the spectral response of OH vibrations hydrating OH$^-$ with a minimum around 3310 cm^{-1}, corresponding to the low-frequency shoulder observed in the transient absorption spectrum shown in the right panel of Figure 7.3. Interestingly, the fitted decay rates do not depend on concentration, and only the relative magnitude between $\Delta\sigma_{\mathrm{bulk}}$ and $\Delta\sigma_{\mathrm{ion}}$ changes when the OH$^-$ concentration is varied. The fitted decay rates correspond to time constants of 0.75±0.05 ps and 0.27±0.05 ps for the bulk and ion-associated OH vibrations, respectively.

The concentration-independent behavior of T'_{bulk} indicates that the OD$^-$ ions only influence the energy relaxation of the vibrations of water molecules in their immediate solvation shell. This observation is also consistent with the explanation of the concentration dependence of OD vibrations at ∼2500 cm^{-1} as the result of Förster energy transfer to vibrations of OH groups solvating OD$^-$ ions. The rate constant of the intermediate state, k_*, expressing the delayed rise of the thermal effect, corresponds to a time constant of 0.9±0.3 ps that slightly increase with

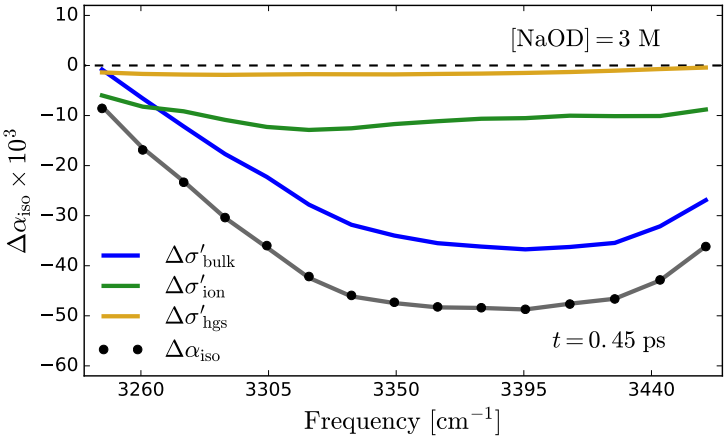

Figure 7.8. Spectral decomposition of the transient absorption spectrum measured at 0.45 ps delay time for a solution of HDO and 3 M NaOD in D_2O solution. The black circles represent the experimental data, and the gray curve results from a least-square optimization of the model given by Eqs. 7.3, 7.5 and 7.6 to the experimental data. The different spectral components are indicated with colors.

concentration, probably as a result of hydrogen-bond network becoming stiffer at high concentrations.

In the above description we did not consider the possibility of energy exchange between the two initially excited OH species. However, recent experiments have shown that the bulk and ion-associated bands can exchange energy with a time constant of ∼9 ps.[207] This energy exchange is much slower than the vibrational relaxation of the bulk and ion-associated OH vibrations, which implies that the energy exchange will indeed have a negligible effect.

7.3.3 Reorientation dynamics

Figure 7.4 shows the parallel and perpendicular absorption change for both complementary solutions at a concentration of 3 M. An interesting observation is that the parallel and perpendicular signals differ at delay times at which the isotropic signal has fully relaxed, i.e. has become full thermal. This residual anisotropy means that the final relaxed state has retained some memory of the orientation of the originally excited state. This result is expected if the vibrational relaxation is fast compared to the characteristic reorientation time of the excited molecules and the global energy redistribution time. In the investigated samples all the relaxation rates, except the OD vibrations in the bulk (1.4–1.8 ps), are significantly faster than the characteristic reorientation time of water of ∼2.6 ps. Increasing

the ion concentration makes the fast ion-associated relaxation pathway become more dominant, which will enlarge the residual anisotropy of the hot ground state, in agreement with the experimental observations.

We use the information obtained from the modeling of the isotropic data to model the anisotropy data. The parallel and perpendicular transient signals can be written in terms of the characteristic reorientation and relaxation mechanisms for each i-component as:

$$\Delta\alpha_{\parallel}(t,\omega) = \sum_{i=1}^{m}[\mathbb{1} + 2R_i(t)]N_i(t)\cdot\Delta\sigma_i(\omega), \tag{7.7}$$

$$\Delta\alpha_{\perp}(t,\omega) = \sum_{i=1}^{m}[\mathbb{1} - R_i(t)]N_i(t)\cdot\Delta\sigma_i(\omega). \tag{7.8}$$

We can now associate an anisotropy dynamics function $R_i(t)$ with each level. We assume that for all levels the anisotropy dynamics follows a mono-exponential decay, as

$$R_i(t) = A_i e^{-t/\tau_{\mathrm{or},i}}. \tag{7.9}$$

We will extract the reorientation dynamics of each level from a global least-squared analysis of the transient absorption data measured in parallel and perpendicular polarization configurations. We employ a few physical considerations to limit the number of free parameters.

The first consideration is that the maximum initial anisotropy $R(0) = 2/5$, and thus the anisotropy of all levels cannot exceed this value. In the description of the anisotropy in NaOH:H_2O solutions we can further neglect the reorientation effect of hydroxide-bounded OH groups since this energy level is no longer significantly populated after 0.4 ps. We assume nevertheless that its anisotropy is fully transferred to the subsequent state, since the molecular reorientation time of hydroxyl groups solvating OH^- ions is expected to be slow.[59,60,202] Under these assumptions we take A_{bulk} and A_{I} equal to a concentration-independent global A_0. In view of the subsequent fast transition, $|\mathrm{I}\rangle \rightarrow |\mathrm{hgs}\rangle$, the hot ground state can conserve some anisotropy, but after the vibrational relaxation is complete (> 6 ps), the remaining anisotropy does not have a significant concentration dependence, as displayed in Figure 7.9.a. We thus assume a concentration-independent reorientation time constant $\tau_{\mathrm{or,hgs}}$, while the initial anisotropy A_{hgs} is concentration dependent and reflects the magnitude of the residual anisotropy that is transferred to the hot ground state.

These assumptions leave us with two global parameters, A_0 and $\tau_{\mathrm{or,hgs}}$, and three concentration-dependent parameters: A_{hgs}, $\tau_{\mathrm{or,I}}$ and $\tau_{\mathrm{or,bulk}}$. The results of the fits are shown with solid lines in Figure 7.4.a and Figure 7.9.a, and offer a good description of the data. The fit delivers an initial anisotropy of $A_0 = 0.39$.

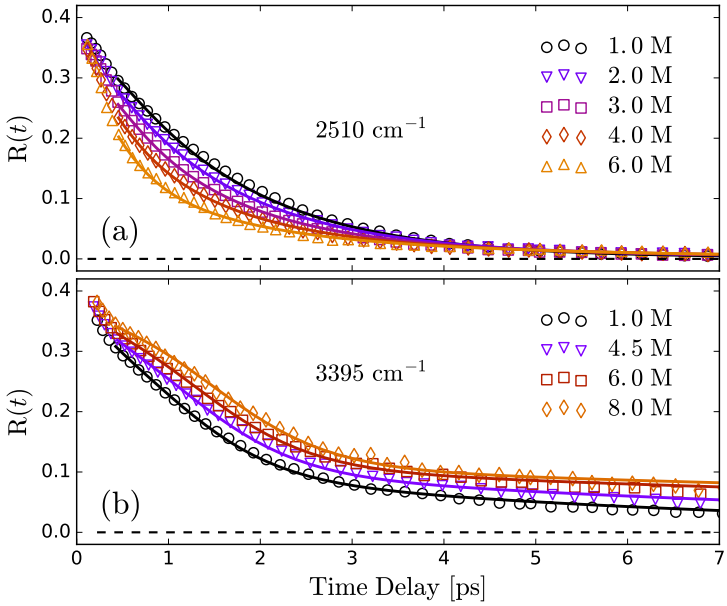

Figure 7.9. Anisotropy as a function of delay time for A) H_2O/OH^- solutions and B) D_2O/OD^- solutions. The solid lines are fits to the experimental data via the models described in the main text.

The hot ground state exhibits an initial anisotropy that increases from 0.0 to a maximum of 0.05 at 4 M. The reorientation time constant of the hot ground state $\tau_{or,hgs}$ is 3.5 ps, and quite independent of the concentration.

We find that the anisotropy decay of the thermally affected complexes becomes faster when the concentration OH^- increases. The time constant $\tau_{or,I}$ decreases from 2.9±0.6 ps at 1 M to 0.9±0.1 ps at 5M. As reported before,[205] $\tau_{or,I}$ represents the energy exchange rate between excited and unexcited complexes. At short delay times the observed signal, $\Delta\sigma_I$, is only due to the heating effect of the solvation complexes that were originally excited. Over time, heat diffusion occurs and the heat will reach other solvation complexes that were not excited, leading to a decay of the anisotropy of the thermal effect. This decay becomes faster at higher OH^- concentrations as the average distance between excited and non-excited complexes decreases with increasing OH^- concentration. The acceleration of the anisotropy decay of the response of the thermally affected complexes explains why the overall anisotropy decay shown in Figure 7.9.a becomes faster with increasing hydroxide concentration.

From the analysis it follows that the reorientation of the bulk-like water molecules decelerates with increasing concentration of OH^- ions. The value of $\tau_{or,bulk}$ in-

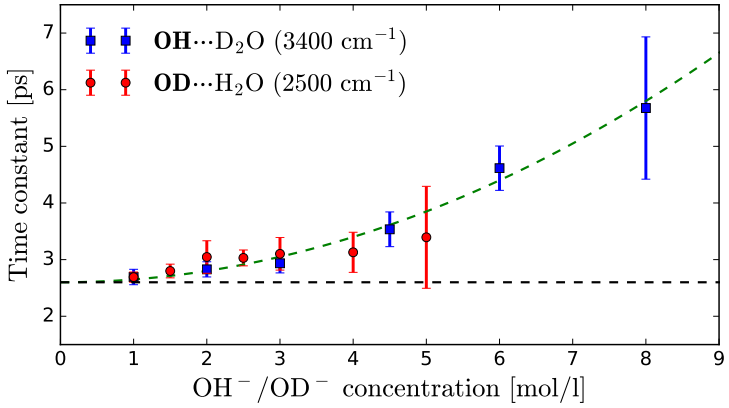

Figure 7.10. Reorientation time constant as a function of the concentration of OH^-/OD^-. The red circles represent the dynamics of HDO molecules in H_2O/OH^- solutions, and the blue squares the dynamics of HDO molecules in D_2O/OD^- solutions. The dashed line shows the molecular reorientation time constant of bulk neat water.

creases from 2.6±0.2 ps at 1 M, similar to τ_{or} of neat water, to 3.4±0.9 ps at 5 M. This increase is illustrated by the red circles in Figure 7.10. This finding shows that the structural dynamics of the hydrogen-bond network slows down with increasing concentration of OH^- ions.

We also analyzed the reciprocal system, i.e. NaOD:D_2O solutions. We assume that the initial anisotropy A'_{bulk} is a concentration-independent global parameter, while fast librations of OH groups in the OD^- structure can possibly affect A'_{ion}. The solid curves in Figure 7.4.b and Figure 7.9.b represent the resulting fits of OH groups in NaOD:D_2O solutions. The curves describe the data well. Similarly to the reciprocal isotope composition, we find that the anisotropy assigned to ion-associated OH groups is negligible from 0.4 ps onwards. For $\tau'_{\text{or,bulk}}$ we observe a significant increase from 2.6±0.2 ps to 6±1 ps, in the concentration range of 1–8 M, as displayed in Figure 7.10 with blue squares. The reorientation time constant $\tau'_{\text{or,hgs}}$ associated with the hot ground state is significantly larger than $\tau'_{\text{or,bulk}}$ over the whole concentration range. It increases from 6.0±0.4 ps at low concentrations to 20±3 ps at a solution of 8 M.

We thus find that the anisotropy decay of the hot ground state is much slower in the experiment on the OH vibration than in the experiment on the OD vibration, for which we found a value of 3.5 ps for $\tau_{or,bulk}$. This difference can be explained from the fact that in the experiment on the OH vibration of HDO in NaOD:D_2O, there is no background absorption of hydrated OD^- complexes at the frequency of the OH vibration. In the experiment on the OD vibration of HDO in NaOH:H_2O,

there is a background absorption of a high concentration of OH groups of hydrated OH^- complexes at the frequency of the OD vibration, and the hot ground state response is dominated by the heating effect on the OH groups of the hydrated OH^- complexes. The anisotropy of this heating effect shows a rapid decay due to the exchange of heat between originally excited hydrated OH^- complexes and non-excited complexes, as expressed in the time constant $\tau_{or,I}$. The hot ground state thus also shows a rapid anisotropy decay in the experiment on the OD vibration of HDO in NaOH:H_2O. As a result, the slowing down of the reorientation dynamics with increasing hydroxide ion concentration is not observable in the anisotropy dynamics of the hot ground state in the experiment on the OD vibration, because in this experiment the heat dissipated by the vibrational relaxation rapidly equilibrates over the focus. In contrast, in the experiment on the OH vibration of HDO in NaOD:D_2O the heating effect remains local for a significant amount of time, and the anisotropy of this response largely decays as a result of molecular reorientation. Hence, in this experiment the hot ground state shows a much slower anisotropy decay that further decelerates with increasing concentration OD^- due to the slowing down of the molecular reorientation.

Figure 7.10 shows that the reorientation time constant of bulk-like OD/OH groups increases with increasing OH^-/OD^- concentration, indicating an effective slowing down of HDO molecules beyond the immediate solvation shell of hydroxide ions. It should be noted that in the modeling it was assumed that the bulk-like OD/OH show uniform reorientation dynamics, which is not necessarily correct. In fact there may be a distribution of reorientation time constants. The values reported in Figure 7.10 should thus be considered as the average reorientation time constants of all the water molecules outside the cores of the hydroxide hydration structures.

7.4 Discussion

As shown in Figure 7.10, the reorientation time constants follow a superlinear dependence on the hydroxide concentration. This behavior differs from that of water in ordinary salt solutions for which it has been observed that the slowing down effect of anions like Cl^-, Br^-, and I^- on the reorientation of water hydroxyl groups tends to saturate at higher salt concentrations.[59,61,208] This saturation has been explained from the fact that at high concentrations the hydration shells start to overlap. This notion also implies that the slowing down effect is dominated by the single hydrogen bonds that are donated by the water hydroxyl groups to the anion, and is hardly affected by other nearby ions. An exception are solutions of salts where both the cation and the anion are strongly hydrated like $MgSO_4$.[208] In this case solvent-separated ion pairs are created with a strong electric field that locks the dynamics of the hydrogen-bonded water in between the ions, thus leading to a much stronger slowing down effect than for the cases where strongly

hydrating ions are combined with weakly hydrating counter ions, as in $Mg(ClO_4)_2$ or $CsSO_4$. However, even in this case there is no superlinear dependence of the slowing down effect on the salt concentration, because the ions are not statistically distributed over the solution, but forming solvent-separated ion pairs already at low concentrations.

The superlinear dependence of the reorientation time constant on the concentration points at a cooperative effect of hydroxide ions on the reorientation dynamics of water molecules. This cooperativity can be explained from the fact that each hydroxide ion induce a strengthening of the hydrogen bonds and an enhancement of the polarization of a number of surrounding water molecules. As a result of this enhanced polarization, these water molecules will interact more strongly with other nearby hydroxide ions, thus leading to a mutual enhancement of the strengthening of the hydrogen bonds and a stiffening of the hydrogen-bond network.

In a recent study of the reorientation of water molecules in aqueous sugar solutions also a superlinear dependence on the concentration was observed.[62,63] The hydroxyl groups of the sugar molecules donate hydrogen bonds to surrounding water molecules, and it was found that the slowing down of the water molecules gets strongly enhanced in case they belong to two or more sugar hydration shells.

7.5 Conclusions

We have investigated the reorientation dynamics of HDO molecules in $NaOH:H_2O$ and $NaOD:D_2O$ solutions with polarization-resolved femtosecond-IR spectroscopy. Thanks to the distinctive red-shifted and fast relaxation of OH/OD stretch vibrations in the core of the OH^-/OD^- hydration structures, we can determine the dynamics of these core OH/OD stretch vibrations and the dynamics of OH/OD stretch vibrations outside this core.

The spectral distinction also enables us to selectively determine the reorientation dynamics of water molecules outside the core of the OH^-/OD^- hydration structures. We find that the reorientation time constant of these bulk-like hydroxyl groups increases very little up to concentrations of 4 M, showing similar dynamics as in bulk neat water ($\tau_{or,bulk}$ ~2.6 ps). However, when the concentration of OH^-/OD^- ions is further increased, the structural dynamics of the solution is increasingly slowed down. This effect finds its origin in the extended influence of OH^-/OD^- ions outside their first solvation shell, caused by the strong directionality of the hydrogen bonds. At high concentrations, a given water molecule can thus be cooperatively affected by several OH^-/OD^- ions, as was similarly observed for hydrophilic sugar molecules. Hence, this work demonstrates that hydroxide ions have little effect on the hydrogen-bond network at low concentrations, i.e. when the OH^-/OD^- ions are sufficiently separated. However, the effect strongly increases with concentration and at high concentrations the hydroxide structure can be referred to as a semi-rigid hydrogen-bond network.

8

Accelerated vibrational energy relaxation of water in alkaline environments

We observe that hydrated hydroxide ions introduce an additional relaxation channel for the vibrational relaxation of the OD vibrations of HDO molecules in aqueous NaOH solutions. This additional relaxation path involves resonant (Förster) vibrational energy transfer from the excited OD vibration to OH stretch vibrations of hydrated OH^- complexes. This energy transfer constitutes an efficient mechanism for dissipation of the OD vibrational energy, as the accepting OH stretch vibrations show an extremely rapid relaxation with a time constant of <200 fs. We find that the Förster energy transfer is characterized by a Förster radius of 2.8±0.2 Å.

8.1 Introduction

Understanding the transfer of energy in water, the most ubiquitous liquid in nature, is of fundamental importance for many chemical and biological processes. In fact, the structural and cooperative characters of water are seen to facilitate a wide range of essential interactions in nature, e.g. protein folding.[12] When energy is locally dissipated in an aqueous environment, the excess energy rapidly equilibrates due to structural rearrangements and intermolecular couplings.[21,29,209,210] One of these couplings is dipole-dipole interaction leading to resonant (Förster) energy transfer.[129] Vibrational Förster energy transfer has been observed for amide vibration of peptides,[211] the CO vibration on metal surfaces,[212,213] and for the stretch vibrations of water and ice.[21,29,31] In pure H_2O, Förster transfer between the OH stretch vibrations takes place on a time scale of <100 fs.[21]

Förster energy transfer can also occur between vibrations of different nature. For instance, in acid water a Förster-type coupling between hydrated protons and OD vibrations has been observed, leading to an accelerated relaxation of the latter vibrations.[31] Here we investigate whether a similar effect can occur in alkaline solutions. Recent theoretical studies showed that hydroxide ions possess a different solvation topology as compared to protons.[75,76,79,81]

We use ultrafast mid-IR pump-probe spectroscopy to measure the vibrational relaxation dynamics of OD stretches of HDO molecules dissolved in aqueous solutions of hydroxide ions of different concentration.

8.2 Experimental methods

Aqueous hydroxide solutions were prepared by diluting a commercially available solution of 50 wt% NaOH (Sigma Aldrich) in deionized water (5.5 μS/m, Milli-Q) at concentrations ranging between 1 and 5 M. In addition, D_2O (99.96% D, Eurisotop) is added to obtain an OD:OH ratio of 4% in all studied samples. The samples were kept between two 2-mm-thick CaF_2 windows separated with Teflon spacers of 25 μm for 1–3 M NaOH solutions and 10 μm at higher concentrations.

We perform polarization-resolved transient absorption measurements using femtosecond mid-infrared light pulses centered at a frequency of 2510 cm^{-1} that are resonant with the OD stretch vibration of HDO molecules in aqueous solution. The experimetal aspects of these experiments have been discussed in Chapter 3.

The experimentally obtained parallel and perpendicular transient absorption signals are used to construct the isotropic transient response:

$$\Delta\alpha_{\text{iso}}(\omega,t) = \frac{1}{3}\left[\Delta\alpha_{\parallel}(\omega,t) + 2\Delta\alpha_{\perp}(\omega,t)\right], \tag{8.1}$$

where ω and t are the probe frequency and time delay, respectively. The isotropic

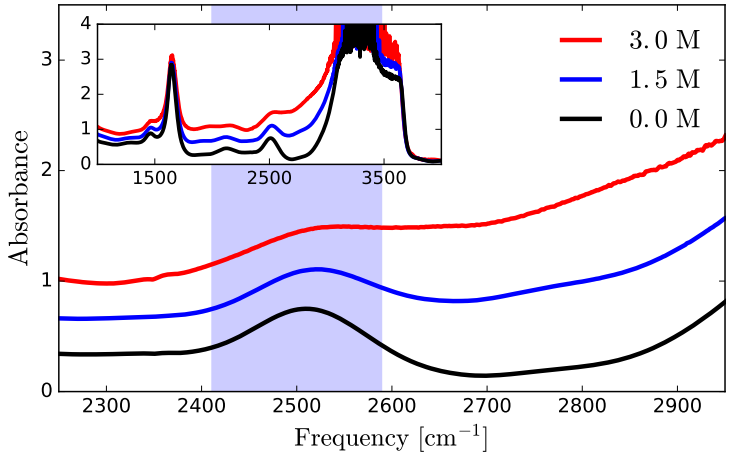

Figure 8.1. Linear IR spectra of 8% HDO and different concentrations of NaOH in H_2O. The blue shaded area indicates the region where transient absorption is recorded.

signal provides information on the rate of vibrational energy relaxation and is insensitive to molecular reorientation.

8.3 Results

8.3.1 Linear IR absorption

Figure 8.1 displays linear absorption spectra of solutions of 8% HDO and different concentrations of NaOH in H_2O. The spectra show a band centered at at 2510 cm^{-1} that is assigned to the OD stretch vibration of HDO molecules that are hydrogen bonded to neighbouring water molecules. With increasing the OH^- concentration, a high-frequency shoulder rises that is attributed to the OH stretch vibrations of H_2O molecules donating strong hydrogen bonds to OH^- ions. The spectral responses of the OD/OH stretch vibrations are negligibly affected by the Na^+ ions.

8.3.2 Isotropic transient spectra

Figure 8.2 shows isotropic transient absorption spectra for neat HDO:H_2O solvent and a solution of 8% HDO and 5 M NaOH in H_2O. In both panels, the isotropic transient spectrum shows a pump-induced bleaching signal around 2510 cm^{-1} due to the excitation of the OD stretch vibration of the HDO molecules. At frequencies

<2420 cm^{-1} the upper panel also shows the high-frequency wing of the $|1\rangle \rightarrow |2\rangle$ induced absorption. The lower panel shows that the amplitude of the bleaching signal of the OD stretch vibration gets smaller upon the addition of NaOH because of the absorption of H_2O molecules hydrating OH^-. The transient spectra of the lower panel show a markedly faster relaxation than those of the upper panel. In addition, the transient spectra in the lower panel at early time delays show a shoulder at the blue side that rapidly relaxes (< 1 ps). This shoulder represents the excitation of hydroxide-associated OH groups that have a relaxation rate of about 200 fs.[205]

To elucidate the transient spectral response of excited OH stretch vibrations of H_2O solvating HO^-, we measure transient absorption spectra of NaOH:H_2O solutions in the concentration range of 1–5 M without the addition of D_2O. Hence, we solely probe the vibrational relaxation dynamics of the ion-associated OH groups. The signal is fitted using a two-step relaxation model, in which the excited OH vibration relaxes rapidly within the solvation structure of the OH^- ion leading to a locally heated hydration complex with an associated intermediate state spectrum $\Delta\sigma_{\mathrm{I}}$. This locally hot state equilibrates with the surroundings due to heat diffusion, thus creating a global hot ground state $\Delta\sigma_{\mathrm{hgs}}$. This relaxation mechanism was observed in a previous study on heat diffusion and molecular reorientation in aqueous hydroxide solutions.[205]

From a least-square fit of the isotropic data, we find that the subsequent relaxation processes take place with time constants of $\sim$ 200 fs and 0.5±0.1 ps, both independent of the concentration. The spectral signature $\Delta\sigma_{\mathrm{OH}}$ of the excited state also does not depend on concentration. The spectral shape of the intermediate state $\Delta\sigma_{\mathrm{I}}$ is very similar to that of the hot ground state $\Delta\sigma_{\mathrm{hgs}}$. The main difference is that $\Delta\sigma_{\mathrm{I}}$ has a much larger amplitude.

8.3.3 Spectral decomposition and population dynamics

Based on the observations, we consider the transient absorption signal to be composed of the responses of two excited states and a thermal spectrum $\Delta\sigma_{\mathrm{therm}}$. This latter spectrum $\Delta\sigma_{\mathrm{therm}}$ represents both the spectral response $\Delta\sigma_{\mathrm{I}}$ of the intermediate state of the relaxation of the OH vibration of H_2O molecules solvating OH^-, and the spectral response $\Delta\sigma_{\mathrm{hgs}}$ of the final hot ground state. The time evolution $\Delta\sigma_{\mathrm{therm}}$ will thus represent the population dynamic of both states. We thus model the experimental data with a linear combination of three states with associated transient spectra $\Delta\sigma_j$ and time-dependent populations N_j:

$$\Delta\alpha_{\mathrm{iso}} = \sum_{j=1}^{3} N_j(t) \cdot \Delta\sigma_j(\omega). \tag{8.2}$$

To determine the relaxation dynamics of the OD stretch vibration, we perform

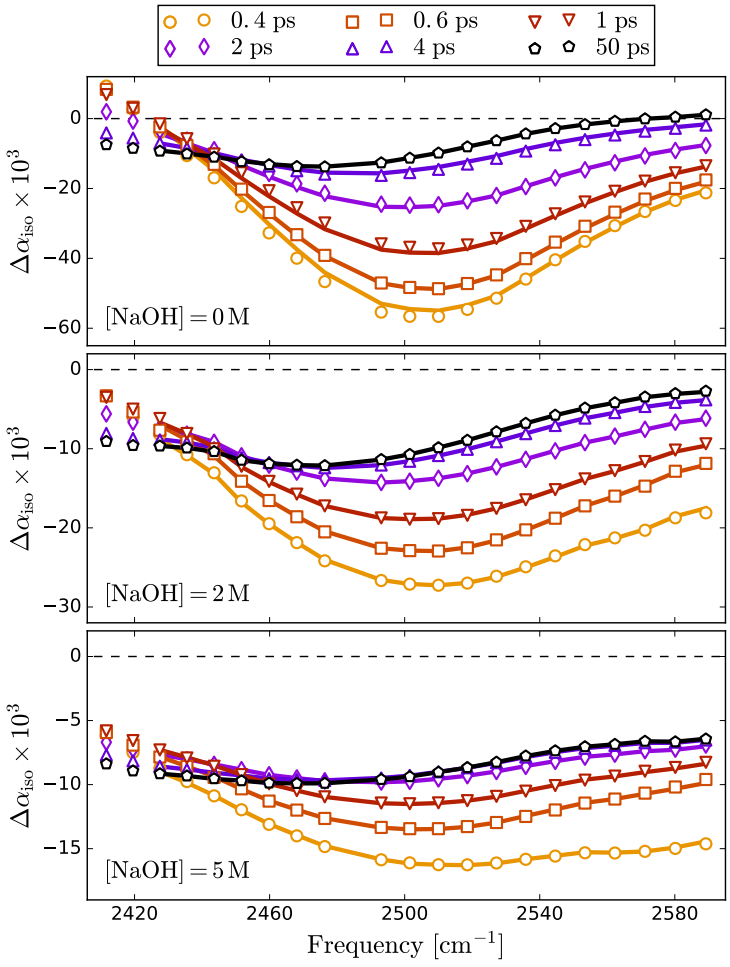

Figure 8.2. Isotropic transient absorption spectra for neat HDO:H_2O (upper panel), and HDO dissolved in 2 M (middle panel) and 5 M (lower panel) NaOH:H_2O solutions. The solid lines represent the results of a fit using the kinetic model described in the text.

a spectral decomposition of the transient absorption spectra at all delay times and all concentrations. In this analysis we fix the shape of the independently measured concentration-independent $\Delta\sigma_{\mathrm{OH}}$ band, and we fix the shape of the thermal spectrum $\Delta\sigma_{\mathrm{therm}}$ at each studied OH^- concentration to the transient absorption spectrum measured at late delay times. We treat the spectral shape of the excited OD vibration $\Delta\sigma_{\mathrm{OD}}$ as a global fit parameter across all OH^- concentrations. The

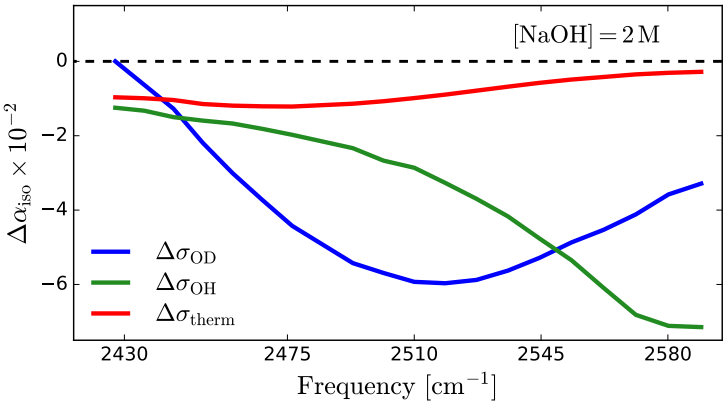

Figure 8.3. Spectral decomposition of the transient absorption spectrum of a solution of HDO and 2 M NaOH in H_2O. The spectra $\Delta\sigma_{OH}$ and $\Delta\sigma_{therm}$ have been fixed in a least-squares optimization process of Eq. 8.2 to the data, while the spectral shape $\Delta\sigma_{OD}$ of the OD vibrations is fitted as a global parameter across all OH^- concentrations.

global fit yields the spectral shape of $\Delta\sigma_{OD}$ and the time-dependent population dynamics $N_j(t)$ of all three states without any assumption about the relaxation mechanism. For a 2 M NaOH:H_2O solution, the minimization process yield the spectral components shown in Figure 8.3 and the population dynamics displayed in Figure 8.4. The solid red line in Figure 8.4 shows the dynamics of the thermal state, which represents the decay of the intermediate state of the relaxation of the OH vibration of H_2O molecules solvating OH^- at short delay times, and the ingrowing signal of the hot ground state at late delay times (>2 ps). The solid curves in Figure 8.2 show that the spectral components shown in Figure 8.3 fit well our experimental data, even at the highest OH^- concentration of 5 M.

In Figure 8.5 we show the normalized population dynamics of the excited OD vibration for 5 different NaOH concentrations. We observe that the relaxation becomes faster and increasingly non-exponential with increasing ion concentration. This ion-induced change of the relaxation can be explained with two possible scenarios: i) hydroxide ions affect the binding dynamics of the hydrogen-bond network, which in turn changes overall the vibrational relaxation process. ii) The spectral overlap between the OD band and the hydroxide continuum enables resonant Förster energy transfer from excited OD vibrations to unexcited hydroxide complexes.

To identify the correct scenario of the ion-induce change in the relaxation rate, we performed the same experiment on reciprocal isotope solutions. We thus measure transient spectral response of solutions of HDO and OD^- in D_2O, following

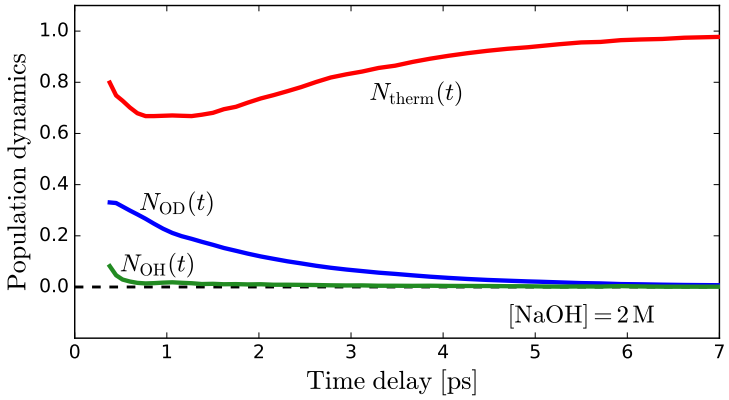

Figure 8.4. Fitted population dynamics of the different spectral components of Figure 8.3 of a solution of HDO and 2 M NaOH in H_2O. The population dynamics of the thermal spectrum represents both the decay of the intermediate state of the relaxation of the OH vibration of H_2O molecules solvating OH^-, and the ingrowing signal of the hot ground state.

excitation of the OH stretch vibration of the HDO molecules near 3400 cm^{-1}. Since the OH stretch vibration band does not overlap with the deuteroxide-induced continuum, as the inset in Figure 8.6 shows, the possibility of Förster energy transfer can be ruled out for these samples. Using a similar temporal decomposition fit, we determine the time-dependent traces that describe the relaxation dynamics of OH stretch vibrations. The results for 5 different OD^- concentrations are displayed in Figure 8.6. With increasing OD^- concentration, we observe a negligible change in the relaxation rate. At all concentrations the relaxation can be well described with an exponential function with a decay time constant of 0.75 ps. This relaxation time is similar to the previously reported time constant of 0.7 ps for the excited OH stretch vibration of HDO in neat HDO:D_2O.[26]

8.3.4 Förster energy transfer

The comparison between Figures 8.5 and 8.6 shows a clear difference in the effect on the relaxation of adding OH^- or OD^- ions, respectively. This difference unambiguously shows that the acceleration observed in Figure 8.5 is due to Förster energy transfer from the excited OD vibrations to OH vibrations of H_2O molecules hydrating OH^- ions. This energy transfer is enabled by the spectral overlap of these vibrations. In principle the reverse Förster process from hydroxide complexes to OD vibrations can also occur. However, this interaction will have a negligible effect since vibrationallly excited OH groups of of H_2O molecules hydrating OH^- ions quickly relax with a time constant <200 fs. Hence, the Förster energy transfer

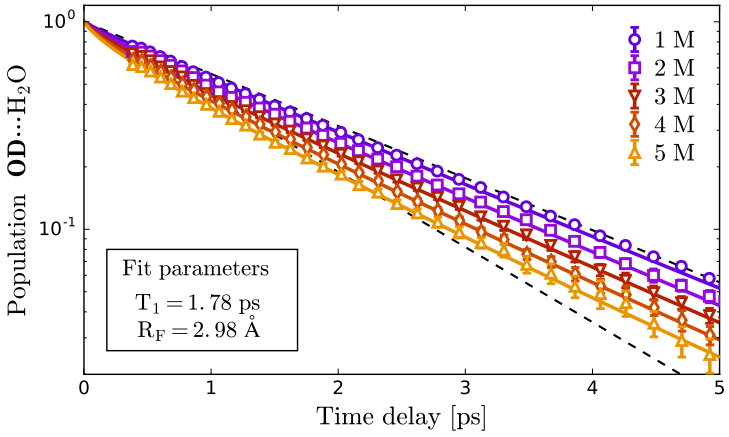

Figure 8.5. Time-evolving population probability of excited OD stretch vibrations at 5 different NaOH concentrations. The markers show the temporal decomposition described in the main text. The solid lines show the least-square fit of Eq. 8.5 which results in 1.78 ps for the OD vibrational lifetime and 2.98 Å for the Förster radius. The dashed lines offer guides of two mono-exponential decays with time constants of 1.75 and 1.2 ps.

to the hydrated OH^- complexes serves as an effective additional relaxation channel for the excited OD vibrations. In the following we will model the effect of this additional channel using the Förster formalism.

Within the Förster model, the rate of energy transfer between two dipoles is given by

$$k_{\mathrm{F}}(r) = \frac{1}{T_1}\left(\frac{R_{\mathrm{F}}}{r}\right)^6, \tag{8.3}$$

with T_1 the intrinsic lifetime of the excited state and r the distance between the two interacting oscillators. The Förster radius R_{F} determines the distance at which 50% of the excitation energy is transferred via the Förster mechanism within the lifetime T_1 of the excitation. It thus follows that the Förster process becomes significant if the mean donor-acceptor distance is comparable or smaller than R_{F}, as will be the case at high OH^- concentrations. Using Eq. 8.3 and assuming a radially uniform distribution of receiving oscillators, the survival probability of donors is given by:[129]

$$S(t,\rho) = \exp\left(-4\pi\rho\int_{a_0}^{\infty} dr r^2\left[1 - e^{-k_{\mathrm{F}}(r)t}\right]\right), \tag{8.4}$$

with ρ the density number of OH^- ions and a_0 the minimal approach distance,

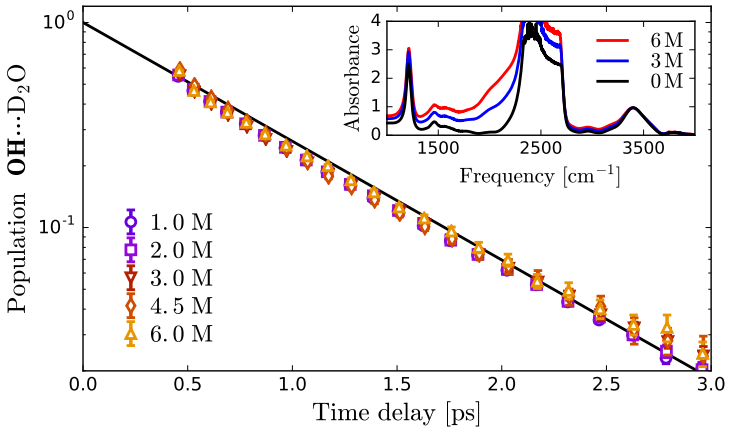

Figure 8.6. Time-evolving population probability of excited OH stretch vibrations at 5 different NaOD concentrations. The markers show the temporal decomposition described in the main text. The solid line represents a mono-exponential decay with time constant of 0.75 ps, similar as in neat HDO:D_2O solvent.[26]

which is the excluded volume of a water molecule (in the limit of $a_0 = 0$, we recover the original formula reported by Förster).

Assuming that the intrinsic vibrational relaxation process and the Förster energy transfer are independent of each other, the time dependence of the excited population is given by:

$$N(t,\rho) = \exp\left(-\frac{t}{T_1} - 4\pi\rho\int_{a_0}^{\infty} dr r^2\left[1 - e^{-k_F(r)t}\right]\right). \tag{8.5}$$

We fit this expression to the experimental data shown in Figure 8.5 with T_1 and R_F as global parameters. We fix a_0 to the previously reported value of 1.5 Å for OD vibrations in aqueous solutions.[31] The resulting fits are represented by the solid curves in Figure 8.5. The intrinsic vibrational lifetime T_1 of the OD vibration obtained from the fit is 1.78±0.05 ps, which agrees well with the results of previous studies.[25,29] We find a Förster radius of 2.8±0.2 Å, which is similar to the intermolecular distance of ∼3 Å in liquid water.[214,215]

8.4 Discussion

We find that the hydration complexes of OH^- can act as antennae receiving energy from nearby excited vibrations. Because of their large, nearly continuous absorption bandwidth, we can expect that hydrated hydroxide ions can quench the energy

of any IR-active vibration between 1000 and 3400 cm^{-1}, like amide vibrations and carbonyl groups ($\sim$1700 cm^{-1}) that are widely observed in nature. As such, hydrated hydroxide ions can act as effective dissipators of excess vibrational energy in aqueous chemical reactions.

Our findings are in line with previous observations for protonated aqueous solutions.[31] The hydrated proton shows a similar continuum absorption band as the hydrated hydroxide ion,[216] and is also observed to accept energy from excited OD vibrations, thereby accelerating their relaxation.[31] For the coupling between OD vibrations and hydrated protons, a larger Förster radius of $\sim$4 Å was found, showing that hydrated protons are even more efficient acceptors of vibrational energy than hydrated hydroxide ions.

8.5 Conclusion

We studied the vibrational relaxation mechanism of OD vibrations of HDO molecules in NaOH:H_2O solutions using femtosecond mid-infrared transient absorption spectroscopy. We decomposed the measured transient spectra into spectral components corresponding to the excited OD stretch vibration of the HDO molecules, the excited OH stretch vibrations of H_2O molecule hydrating OH^- ions, and the hot ground state that results after the vibrational relaxation is complete. This analysis yielded the population dynamics of all three states without any assumption about the relaxation rate and mechanism. With increasing the concentration OH^- ions in solution, we found the decay of the excited OD vibration to become faster and to deviate increasingly from a single exponential decay. These observations indicate the presence of an additional relaxation channel for the OD vibrations. This additional path is well described as the effect caused by Förster resonance energy transfer from OD stretches to the OH stretch vibrations of hydrated OH^- complexes. From a global analysis of the relaxation dynamics at different OH^- concentrations we determined the intrinsic vibrational lifetime of the OD stretch vibration to be 1.78$\pm$0.05 ps and the Förster radius to be 2.8$\pm$0.2 Å. Our results show that hydrated OH^- complexes can serve as effective antennae and dissipators of excess vibrational energy in aqueous chemical reactions.

9

Long-range solvation interaction in aqueous phenolate solution*

We investigate the orientational dynamics of water molecules solvating phenolate ions using ultrafast vibrational spectroscopy and density-functional-theory-based molecular dynamics simulations. To assess the roles of the hydrophobic and hydrophilic parts of the anion, we also perform experiments and simulations on solutions of phenol. The experiments show that phenolate immobilizes (τ_{or} >10 ps) 6.2±0.5 water molecules beyond the first solvation shell of its oxygen atom, whereas phenol immobilizes only 2 water molecules, including the water molecules in its first solvation shell. The simulations reproduce the experiments very well, and show that phenolate causes a local ordering of the hydrogen-bond structure that extends beyond the first solvation shell, thus explaining the experimental observations. The comparison with phenol shows that the long-range solvation interaction of phenolate is due to the high charge density of its negatively charged oxygen atom.

* *This chapter is based on:* Roberto Cota, Ambuj Tiwari, Bernd Ensing, Huib J. Bakker and Sander Woutersen, *Hydration interactions beyond the first solvation shell in aqueous phenolate solution*, Phys. Chem. Chem. Phys. **2020**, 22, 19940–19947.

9.1 Introduction

Ions dissolved in water modify the hydrogen-bond structure and give rise to local structural ordering in the form of solvation shells. These structures play an important role in many biological, chemical and physical processes, such as the ion selectivity of ionic transmembrane channels and the salting in or out of proteins as exemplified in the Hofmeister series.[11,34,185,189,192,217,218] For this reason numerous experimental and theoretical studies have been carried out to investigate the interactions between ions and water.[14,161,219]

As has been discussed in Chapter 3, time-resolved vibrational spectroscopy is very well suited for investigating aqueous solvation, because the hydrogen bonds between a solute and the OH groups of solvating water molecules can be probed in a direct manner by tracking the dynamics (frequency fluctuations and orientational diffusion) of the OH-stretch mode. Up to now, time-resolved OH-stretch (and OD-stretch) spectroscopy studies of anion solvation have focused mostly on single-atom anions, notably the larger halides.[58,201] These experiments have shown that the local restructuring of the hydrogen-bond network by the anions leads to a slowing down of the dynamics of the water molecules in the first solvation shell: for some anions, the correlation time of the random orientational motion of the OH bonds involved in the water-anion hydrogen bonds is more than an order of magnitude slower than in bulk water.[201] Whereas the halide anions have been extensively investigated with time-resolved vibrational spectroscopy, much less is known about the oxygen-containing anions.

Here, we investigate the solvation of the molecular anion phenolate. In this anion oxygen has a single negative charge, which renders its ionic radius comparatively small. In addition, phenolate is of particular interest since simulations show that the negatively charged oxygen of this anion can form multiple hydrogen bonds with surrounding water molecules, while the phenyl ring is only weakly solvated.[220,221] It is not clear how these opposing effects influence the dynamics of the solvating water. Phenolate ions and phenol are also the subject of active research because they are widely observed in nature as organic pollutants,[222,223] and can function as precursors in organic syntheses.[224,225] Previous studies suggest that phenol and the phenolate ion (and their corresponding derivatives) can have a strong impact on the chemical reactivity of aqueous solutions, in particular at the water-air interface due to their amphiphilic character.[226–229]

We investigate the influence of phenolate ions on the reorientation dynamics of solvating water molecules using two complementary methods: time-resolved vibrational spectroscopy and density-functional-theory-based molecular dynamics simulations (DFT-MD). To distinguish the effects of the hydrophobic and hydrophilic parts of the anion, we also perform experiments and simulations on solutions of phenol. The experiments show that the local water dynamics is much more affected by phenolate than by phenol. This difference finds its origin in the strong

hydrogen bonding between water and the negatively charged oxygen of phenolate. The simulations confirm this observation, and show that phenolate has a long-range effect on the hydrogen-bond structure and dynamics of water, that extends beyond the first solvation shell.

9.2 Materials and Methods

9.2.1 Sample preparation

Commercially purchased phenol PhOH (≥99.5%, Sigma Aldrich) and PhONa (99%, Sigma Aldrich) were used to prepare solutions in isotope-diluted water (HDO:H_2O fraction 8%) prepared by mixing D_2O (99.96% D, Eurisotop) and deionized H_2O (conductivity 5.5 μS/m). Phenol was investigated in a solution of 0.84 molal (close to its maximum solubility of 0.88 m), while sodium phenolate solutions were prepared with concentrations of 0.84, 1, 2 and 3 m. For pump-probe experiments, samples were kept in a CaF_2 sample cell with a 50 μm path length, while the path length was set to 25 μm for linear IR spectra.

9.2.2 Vibrational pump-probe experiments

We perform polarization-resolved infrared transient-absorption measurements using pulses resonant with the OD-stretch mode (2510 cm^{-1}). The pump-probe setup used in these experiments is described in Section 3.6.

We use the parallel and perpendicular transient absorption changes to construct the isotropic transient signal as has been described in Section 3.5:

$$\Delta\alpha_{\text{iso}}(\omega,t) = \frac{1}{3}\left[\Delta\alpha_{\parallel}(\omega,t) + 2\Delta\alpha_{\perp}(\omega,t)\right], \tag{9.1}$$

where ω is the probe frequency and t the delay between pump and probe pulses. The isotropic signal provides information on the population dynamics of the vibrationally excited OD-stretch mode. Since vibrations aligned along the pump polarization are preferentially excited, the parallel transient signal is initially larger than the perpendicular signal. This anisotropy decays due to random reorientation of the excited molecules, and the anisotropy decay function provides direct information on the orientational diffusion of the water molecules.[25,26] The rotational anisotropy is defined by the normalized difference between parallel and perpendicular transient signals:

$$R(\omega,t) = \frac{\Delta\alpha_{\parallel}(\omega,t) - \Delta\alpha_{\perp}(\omega,t)}{\Delta\alpha_{\parallel}(\omega,t) + 2\Delta\alpha_{\perp}(\omega,t)}, \tag{9.2}$$

and is independent of the population relaxation of the excited OD-stretch mode.

The decay time of this anisotropy represents the orientational dynamics of water molecules.

9.2.3 Simulations

All DFT-MD simulations were performed with the CP2K package[230] using the combined Gaussian and plane-wave method as implemented in the Quickstep module.[231] We used the BLYP[232,233] functional in conjunction with Grimme's D3 correction for van der Waals interactions[234] with a TZVP basis set[235] and a 300 Ry plane-wave cutoff. Core electrons were represented by GTH pseudopotentials[236]. A CSVR thermostat[237] maintained a temperature of $T = 325$ K. The systems contained a single solute molecule and 63 water molecules in a cubic supercell subject to periodic boundary conditions. The number of water molecules are calculated to match the experimental density with a cubic box that has an edge length of 12.43 Å. The trajectory was saved every 50 fs.

To calculate the orientational autocorrelation function we first calculate the vector $\vec{u}$ along the OH bond associated with each water molecule. Next, the time evolution of this vector $\vec{u}$ is determined by calculating the autocorrelation function $C_2(t)$ defined as

$$C_2(t) = \langle P_2[\hat{u}(0) \cdot \hat{u}(t)] \rangle, \tag{9.3}$$

where P_2 is the second-order Legendre polynomial, and $\hat{u}(t)$ is the unit vector that describes the orientation of a given OH bond at any time t. This $C_2(t)$ can be directly compared to the experimentally observed anisotropy decay. The long-range structure is explored by calculating the radial distribution function g_{OH}. This function is the probability to find a H atom at a distance r from the center of a solute oxygen atom, described as

$$g_{\mathrm{OH}} = \frac{\rho_{\mathrm{H}}(r)}{\rho_{\mathrm{H,bulk}}}, \tag{9.4}$$

where $\rho_{\mathrm{H}}(r)$ is the number density of H atoms at a distance r and $\rho_{\mathrm{H,bulk}}$ is the density of H atoms in the bulk.

9.3 Results

9.3.1 Linear absorption spectra

Figure 9.1 shows linear absorption spectra of PhOX (X = H^+, Na^+) solutions in isotopically diluted HDO:H_2O, with the OD-stretch band of HDO at 2510 cm^{-1}. Phenol has negligible influence on the OD-stretch spectrum (mainly a decrease in absorption due to water dilution at high concentrations), whereas in phenolate solutions, the OD-stretch band has a low-frequency wing centered at approximately

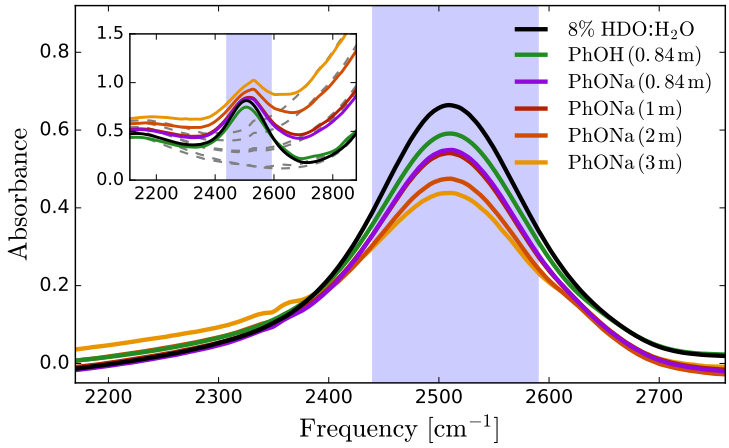

Figure 9.1. Linear IR spectra of PhOX solutions (X = H, Na) in dilute HDO:H_2O. The peak centered at 2500 cm^{-1} is due to the OD-stretch vibration of HDO molecules. In phenolate solutions, the low-frequency shoulder is due to OD groups that donate strong hydrogen bonds to PhO^- ions. The purple shaded bar indicates the region where transient absorption is recorded. The inset shows raw spectra with (solid lines) and without (dashed lines) OD oscillators.

2300 cm^{-1} which we assign to OD groups coordinating to the phenolate O atom. The frequency of these OD vibrations is redshifted compared to neat HDO:H_2O as a result of the strong hydrogen bonding with the negatively charged oxygen atom of phenolate. A similar redshift is observed for the OH-stretch band (centered at ∼2900 cm^{-1}) in crystalline NaPhO·3H_2O due to OH groups coordinated to PhO^-, and for the OH-stretch band of H_2O in NaOH solutions.[71] At high frequencies we observe the low-frequency wing of the OH stretch vibrations coordinated to phenolate. In view of the pK_a value of phenol of 10, the fraction of phenolate that will react to phenol is negligible (∼10^{-2} M) compared to the phenolate fraction.

9.3.2 Time-resolved vibrational spectroscopy

In the time-resolved experiments, the infrared pump pulse excites a small fraction (∼2%) of the OD stretch vibrations from the $|0\rangle$ to the $|1\rangle$ state, and the resulting absorption change $\Delta\alpha$ is measured with the probe pulse as a function of the infrared frequency ω and the delay t with respect to the excitation pulse (see Section 3.4). Figure 9.2 shows the results for neat HDO:D_2O and two of the investigated solutions. The reduced density of absorbers in the $|0\rangle$ state leads to a decrease in absorption ($\Delta\alpha < 0$) at the $|0\rangle \rightarrow |1\rangle$ transition frequencies. The population of the $|1\rangle$ state gives rise to $|1\rangle \rightarrow |0\rangle$ stimulated emission, thus enhancing the bleaching

at the $|0\rangle \rightarrow |1\rangle$ frequencies, and an induced absorption ($\Delta\alpha > 0$) at the $|1\rangle \rightarrow |2\rangle$ frequencies, which constitutes the lowest observed frequencies in Figure 9.2. The relaxation of the vibrationally excited OD-groups is observed as a decay of the signal amplitude on a picosecond time scale. For long time delays (> 10 ps), all the OD groups are back in the $|0\rangle$ state, but there is a residual $\Delta\alpha$ signal due to local heating in the sample: in the relaxation process, the energy is thermalized (transferred from the OD-stretch mode to low-frequency degrees of freedom), and the resulting increase in local temperature gives rise to a blueshift and an intensity decrease of the OD-stretch band.[25] Complete thermalization (diffusion of the locally deposited heat out of the focal volume) takes place on a much slower time scale (hundreds of microseconds).

The transient absorption spectra measured for phenolate and phenol have similar shapes and dynamics. The main difference is that the overall amplitude of the transient signal in the phenolate solution is slightly reduced. This reduction is due to the fact that the pump pulses are partially absorbed by OH groups of water that are strongly hydrogen bonded to phenolate. These OH groups are not visible in Figure 9.2 since they relax on a very fast (∼300 fs)[205] time scale compared to that of the excited OD stretch vibrations, 1.7 ps[25] For the transient absorption spectra of the PhOH solution (Figure 9.2-lower panel), the overall amplitude is the same as that of neat HDO:H_2O. In our analysis of the transient data we only use delay times larger than 0.5 ps for which the contribution of the OH groups that are strongly hydrogen bonded to phenolate is negligible.

Previous work has shown that the vibrational relaxation of the OD-stretch mode in HDO:H_2O (both for the neat liquid and for solutions) occurs in two steps, see Figure 9.3: after the $|1\rangle \rightarrow |0\rangle$ relaxation, the vibrational energy is first redistributed over local low-frequency modes, and subsequently is fully thermalized (typically on a time scale of about 1 ps), leading to a local temperature increase (on the order of a few K).[206] In the thermalized state the OD-stretch spectrum is different from that at $t = 0$ (the OD-stretch spectrum is sensitive to temperature), so that the bimodal relaxation is mirrored in biexponential kinetics of the transient OD-stretch absorption change.[25,26] In our experiments we also observe this two-step relaxation mechanism: a singular value decomposition of the data matrices $\Delta\alpha_{\mathrm{iso}}(\omega, t)$ shows that in all cases the transient signal is well described (99%) by two spectral and temporal components. Hence, we describe our experimental data using the two-step model described in Section 3.7:

$$\begin{aligned} \Delta\alpha_{\mathrm{iso}}(\omega, t) &\propto \Delta\sigma_1(\omega) e^{-t/T_1} \\ &+ \Delta\sigma'(\omega) \left(1 + \frac{T^*}{T_1 - T^*} e^{-t/T^*} - \frac{T_1}{T_1 - T^*} e^{-t/T_1}\right), \end{aligned} \tag{9.5}$$

where $\Delta\sigma_1(\omega) = \sigma_{12} - 2\sigma_{01}$ is the difference spectrum of the pumped OD-stretch with respect to the unpumped spectrum, in which the depletion of the ground state

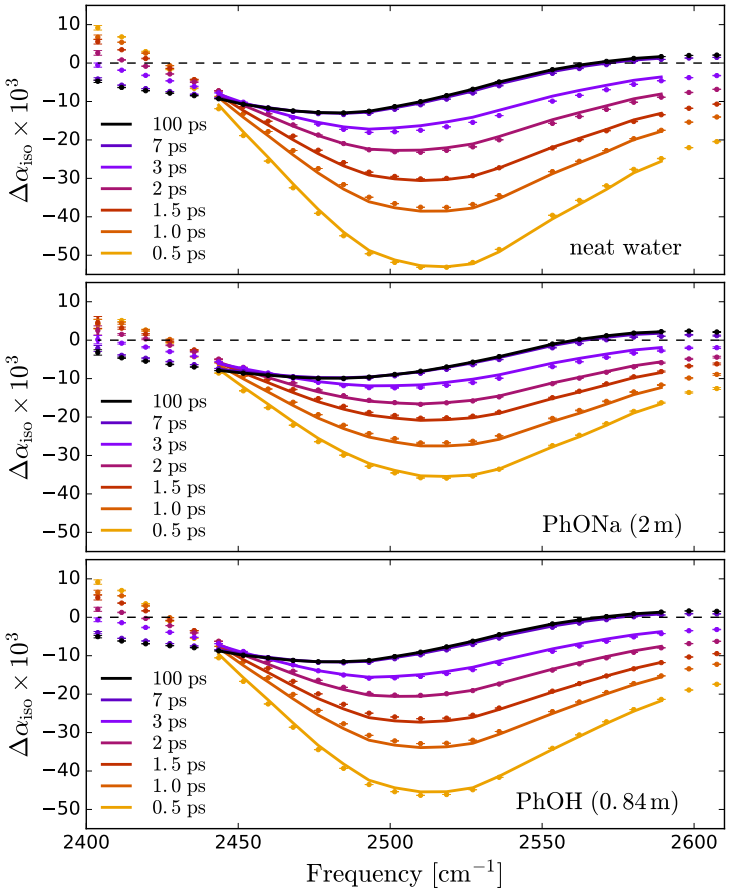

Figure 9.2. Isotropic transient absorption for neat HDO:H_2O solvent (upper panel), a 2 M PhONa solution (middle panel) and a 0.84 M PhOH solution (lower panel). The solid lines represent the fits of a spectral decomposition explained in the main text.

and stimulated emission have the same spectrum σ_{01}, and σ_{12} is the spectrum of the induced absorption. $\Delta\sigma'(\omega) = \sigma'_{01} - \sigma_{01}$ is the difference spectrum of the thermalized state (i.e. the OD-stretch spectrum σ'_{01} at a slightly increased local temperature) with respect to the unpumped spectrum. T_1 is the time constant of the $|1\rangle \rightarrow |0\rangle$ relaxation, and T^* the time constant of the subsequent thermalization (see Figure 9.3). We perform least-square fits of this equation to the experimental $\Delta\alpha_{\mathrm{iso}}(\omega, t)$ data, treating the time constants T_1 and T^* and the spectra $\Delta\sigma_1(\omega)$ and $\Delta\sigma'(\omega)$ as global fit parameters. The solid lines in Figure 9.2 are the resulting

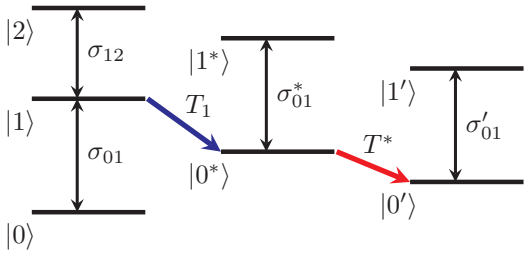

Figure 9.3. Two-step mechanism of the vibrational relaxation of the OD-stretching mode of HDO:H_2O. Eq. 9.5 provides the mathematical representation of this relaxation model, which has been discussed in Section 3.7.

fits. The values obtained for T_1 are the similar for all samples (between 1.6–1.7 ps across the explored solute concentrations), but the equilibration time T^* varies with ion concentration, increasing from 1.2 ps in neat water to 1.5 ps for a 3 m PhONa solution. This slowing down of the thermal equilibration is probably due to an increased rigidity of the hydrogen-bond network induced by the phenolate ions (see below). For the phenol solution the equilibration time constant is similar to that of neat liquid water.

In order to determine the anisotropy of the transient absorption change associated with only the excitation of the OD-stretch vibrations, we must subtract the time-dependent spectral contribution due to the hot ground state (the second term in Eq. 9.5) from both the parallel and perpendicular transient $\Delta\alpha$ signals,[25] Figure 9.4 shows the thermalization-corrected anisotropy for all the samples investigated. In all samples the anisotropy decays on a time scale of about 2 ps, but in the phenolate and phenol solutions there is a residual anisotropy at long delay times. This residual anisotropy, the amplitude of which increases with the concentration of solute, indicates that a fraction of the water OD groups are rotationally immobilized (i.e. have an orientational relaxation time much longer than our accessible time window of 7 ps). We find that we can fit the anisotropy curves very well with a function

$$R(t) = Ae^{-t/\tau} + B, \tag{9.6}$$

where the first term represents the water molecules with bulk-like orientational dynamics, and the offset B the contribution of rotationally immobilized water. The inset in Figure 9.4 shows the offsets extracted from these least-squares fits. The amount of immobilized water scales linearly with the solute concentration, which implies that a fixed number of water molecules is immobilized per solute molecule or ion.

From the residual anisotropy B we can estimate the number of water molecules that are rotationally immobilized by the solute.[?] For phenol this is straight-

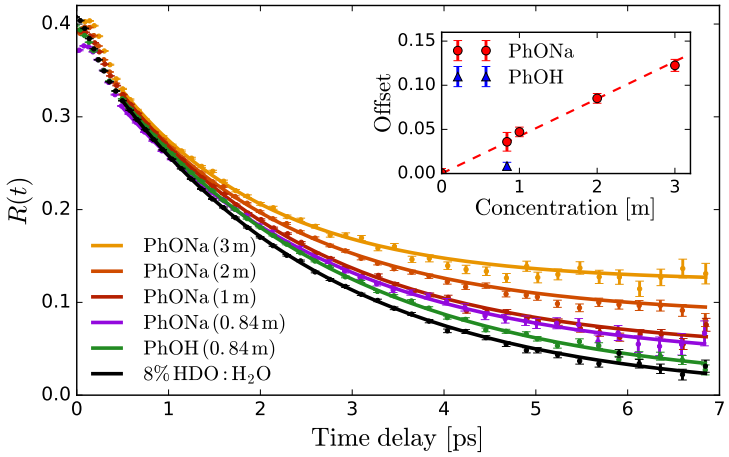

Figure 9.4. Anisotropy decay of the OD stretch vibration of HDO in NaOH:H_2O and NaOH:H_2O. The curves are determined from the averaged anisotropy over the frequency range of 2450–2535 cm^{-1}. The solid lines represent fits of Eq. 9.6 to the data. The inset shows the offset B extracted from the fits as a function of solute concentration.

forward; for phenolate the situation is slightly more complicated. In a 1 m PhONa:H_2O solution there are 55 water molecules per phenolate, of which ∼4 are contained in the first solvation shell. These primary water molecules are not visible in the transient absorption spectra (they absorb at a much lower infrared frequency, see above), and so do not contribute to the anisotropy in Figure 9.4. The experimentally observed residual anisotropy of ∼12±1% thus implies that $0.12 \pm 0.01 \times (55 - 4) = 6.2 \pm 0.5$ water molecules beyond the first solvation shell of the ion are rotationally immobilized. On the other hand, only 1.5±0.7 water molecules are immobilized per phenol molecule, including the first solvation shell.

The significant difference in the number of water molecules immobilized by phenolate and phenol might be due to two effects: (i) a difference in the solvation interaction of these two solutes, or (ii) phenol molecules might form clusters by π stacking (electrostatic repulsion would prohibit this for phenolate), so that the solvent exposed area per phenol molecule might be much smaller than in the case of phenolate. In order to study the latter possibility, we measure the concentration dependence of the UV absorption spectrum of aqueous phenol solution. If phenol would form clusters by π-stacking, excitonic effects should cause a significant change in the $S_0 \rightarrow S_1$ absorption band (at ∼270 nm) of these clusters as compared to monomeric phenol. Since the cluster/monomer ratio should increase with the phenol concentration, any clustering should result in a concentration-dependent shape of the 270 nm absorption band. Hence, we recorded UV absorption spec-

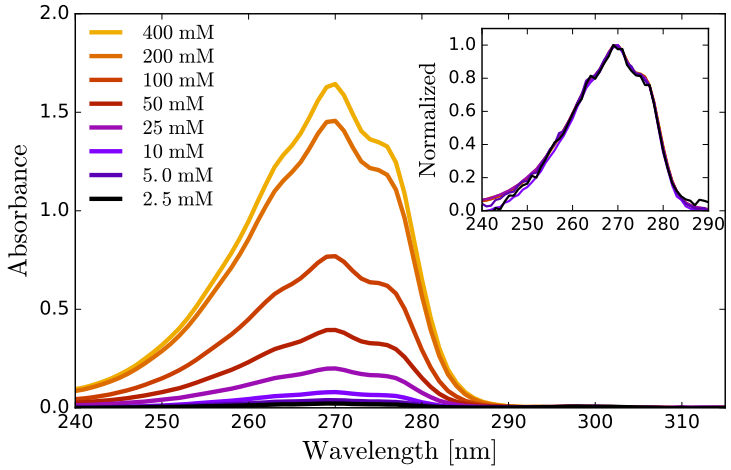

Figure 9.5. UV absorption spectra in the $S_0 \rightarrow S_1$ spectral region of phenol dissolved in water at different concentrations. Samples were kept in a CaF_2 sample cell with a 50 μm path length for samples within the concentration range of 2.5–200 mM, and 25 μm path length at a concentration of 400 mM.

tra of a series of PhOH:H_2O solutions with concentrations ranging from 2.5 to 400 mM. As shown in Figure 9.5, the scaled spectra overlap perfectly, so that clustering of phenol can be ruled out. We conclude that the different numbers of water molecules that are immobilized by phenolate and phenol must be due to a difference in solvation between these two solutes.

9.3.3 DFT-MD Simulations

To investigate the aqueous solvation structure and dynamics of phenolate in more detail, we perform DFT-MD simulations of phenolate and phenol solutions. DFT-MD simulations have been shown to accurately model the aqueous solvation of small solutes[238–240] and to predict the anisotropy decay of water in such solutions reasonably well.[241] Figure 9.6 shows the OH-anisotropy decays of water molecules in phenol and phenolate solutions and in neat water, as obtained from our simulations. As in the experiment, we observe a significant residual anisotropy in the phenolate solution, which is absent in the phenol solution. By partitioning the water molecules, we can study the orientational dynamics of the water molecules in more detail. We distinguish between (1) water molecules (w) in the first solvation shell of the phenolate/phenol (s) oxygen (distance $r_{H_w-O_s} < 2.6$ Å), which we will refer to as solvation water, and (2) the remaining water, denoted as bulk. The solvation water of phenolate shows considerably slower rotational dynamics

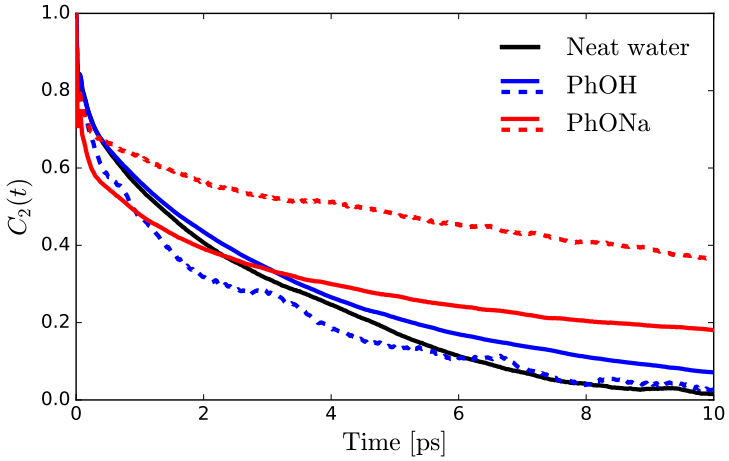

Figure 9.6. OH-orientational correlation function obtained from DFT-MD simulations of phenol and phenolate solutions and neat water. Solid lines: overall correlation function of the water outside the first solvation shell. Dashed lines: orientation correlation function of water molecules in the first solvation shell.

compared to the solvation water of phenol, which is not surprising in view of the strong hydrogen bonds between phenolate and the water molecules in its first solvation shell. In the phenolate solution the rotational dynamics of the water outside the first solvation shell is also found to be significantly slower compared to the rotational dynamics of neat water (red solid line in Figure 9.6). The correlation function of the water molecules beyond the first solvation shell decays to a residual offset of ∼15%, which is similar to the experimental value of 12%. This long-range effect on the water reorientation dynamics, with the ion immobilizing water molecules beyond its first solvation shell, is not present in the phenol solution.

The radial distribution functions obtained from the simulations (Figure 9.7) reveal that there are three to four water H atoms in the first coordination shell of the phenolate oxygen, whereas in the case of the phenol oxygen there is only one. Furthermore, the water molecules are at a much shorter distance from the phenolate oxygen than they are from the phenol oxygen. Both these effects can be attributed to the negative charge on the phenolate oxygen atom. In addition, the radial distribution curve for phenolate shows a well-defined second coordination shell. In contrast, phenol has a rather labile solvation structure, leading to a significant overlap between the first and second coordination shells, as indicated by the lack of a clear minimum in the interval 2–3 Å of the radial distribution. These results show that in the case of phenolate the effect on the hydrogen-bond

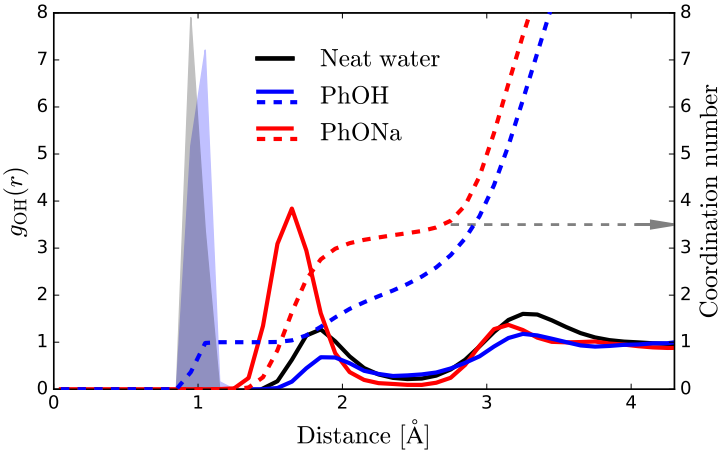

Figure 9.7. Solid red and blue curves: radial distribution function for water H atoms measured from the oxygen of phenol and phenolate. Dashed curves: integral of the distribution curves of phenol and phenolate. The grey arrow shows the number of water molecules in the first coordination shell of phenolate. The shaded blue area represents the H atom of the hydroxyl group of the phenol molecule. The black curve represents the radial distribution function for water H atoms from a central water O atom, where its covalently bonded H atoms are shown by the shaded gray area.

structure and dynamics of water extends over a significantly longer distance than in the case of phenol, in agreement with the experimentally observed larger number of water molecules that are rotationally immobilized by phenolate in comparison to phenol.

9.4 Discussion

Both in the experiments and in the simulations, we observe a residual anisotropy due to water molecules that are rotationally immobilized by the solute. The number of water molecules immobilized by phenolate is surprisingly large, and corresponds to about 6 water molecules beyond its first solvation shell. Comparison with the results obtained on phenol shows that the long-range hydration interaction of phenolate is likely due to its negatively charged oxygen atom. The low-frequency OD-stretch wing observed in the absorption spectrum of the phenolate solution indicates that the negatively charged oxygen of phenolate forms very strong (i.e. short) hydrogen bonds with water, and the simulations show that these phenolate-water hydrogen bonds are sufficiently strong to increase also the hydrogen bond

strength in the second solvation shell, leading to an enhancement of the hydrogen bond structure in the second solvation shell, thus explaining the experimentally observed rotational immobilization of these water molecules.

At first sight the solvation of phenolate may appear similar to the solvation of halide anions, for which also a slowing down of the water reorientation was observed.[59,201] However, the origins of the slowdown are distinctly different: in the case of the halide anions, the solvating water molecules are hydrogen-bonded very weakly to the solute (as reflected by their OD-stretch frequency, which is higher than that of neat water), and the slowdown of the reorientation dynamics is due to the fact that reorienting a water molecule requires breaking and formation of hydrogen bonds, and solvating water molecules in the first hydration shell have less hydrogen-bond acceptors at their disposal than water molecules in the bulk.[242] For this reason the effect of the anions on the hydrogen-bond structure and dynamics is limited to the first solvation shell.

In the case of phenolate, the hydrogen bonds between water and the ions are stronger than in neat water (as reflected by their low OD-stretch frequency), causing an increase in the strength and ordering of the hydrogen-bond network, and thus immobilizing water molecules beyond the first solvation shell. The reason that the negatively charged phenolate oxygen atom forms much stronger hydrogen bonds than the halide anions is its small size: O and O^{2-} have radii of 73 and 126 pm, and O^- will have a radius between these values, whereas Cl^- and Br^- have radii of 167 pm and 182 pm, respectively. Finally, our findings may also shed new light on the solvation of the hydroxide anion, of which the oxygen is isoelectonic with that of phenolate. Our results suggest that the experimentally observed slowdown of water solvating hydroxide (see Chapter 6 and Refs. 200,205) can be explained from the high charge density of its negatively charged oxygen atom, and is not necessarily the result of the delocalized nature of the negative charge in hydroxide solutions.

9.5 Conclusion

We have investigated the solvation of phenolate and phenol in water using a combination of time-resolved pump-probe spectroscopy and density-functional-theory-based molecular dynamics simulations. In the experiments, we probe the reorientation dynamics of the hydroxyl groups of water molecules in the presence of the solute. We find that phenolate rotationally immobilizes ∼6 water molecules beyond its first solvation shell, a surprisingly large number that is confirmed by the simulations. Phenol immobilizes only ∼2 water molecules, including the water molecules in its first hydrations shell. The simulations reveal that the long-range effect of phenolate on the reorientation dynamics of water is due to a local strengthening of the water hydrogen bond network, induced by the high charge density of the negatively charged oxygen atom of phenolate.

References

[1] Russo, J.; Akahane, K.; Tanaka, H. Water-like anomalies as a function of tetrahedrality. *Proc. Natl. Acad. Sci. U. S. A.* **2018**, *115*, E3333–E3341.

[2] Ball, P. Water – an enduring mystery. *Nature* **2008**, *452*, 291–292.

[3] Bernal, J. D.; Fowler, R. H. A theory of water and ionic solution, with particular reference to hydrogen and hydroxyl ions. *J. Chem. Phys.* **1933**, *1*, 515–548.

[4] Soper, A. K. The radial distribution functions of water and ice from 220 to 673 K and at pressures up to 400 MPa. *Chem. Phys.* **2000**, *258*, 121–137.

[5] Wernet, P.; Nordlund, D.; Bergmann, U.; Cavalleri, M.; Odelius, N.; Ogasawara, H.; Näslund, L. Å.; Hirsch, T. K.; Ojamäe, L.; Glatzel, P.; Pettersson, L. G.; Nilsson, A. The Structure of the First Coordination Shell in Liquid Water. *Science* **2004**, *304*, 995–999.

[6] Kumar, R.; Schmidt, J. R.; Skinner, J. L. Hydrogen bonding definitions and dynamics in liquid water. *J. Chem. Phys.* **2007**, *126*, 204107.

[7] Lawrence, C. P.; Skinner, J. L. Ultrafast infrared spectroscopy probes hydrogen-bonding dynamics in liquid water. *Chem. Phys. Lett.* **2003**, *369*, 472–477.

[8] Eaves, J. D.; Loparo, J. J.; Fecko, C. J.; Roberts, S. T.; Tokmakoff, A.; Geissler, P. L. Hydrogen bonds in liquid water are broken only fleetingly. *Proc. Natl. Acad. Sci. U. S. A.* **2005**, *102*, 13019–13022.

[9] Fecko, C. J.; Loparo, J. J.; Roberts, S. T.; Tokmakoff, A. Local hydrogen bonding dynamics and collective reorganization in water: Ultrafast infrared spectroscopy of HOD/D_2O. *J. Chem. Phys.* **2005**, *122*, 054506.

[10] Laage, D.; Hynes, J. T. A molecular jump mechanism of water reorientation. *Science* **2006**, *311*, 832–835.

[11] Ball, P. Water as an Active Constituent in Cell Biology. *Chem. Rev.* **2008**, *108*, 74–108.

[12] Bellissent-Funel, M.-C.; Hassanali, A.; Havenith, M.; Henchman, R.; Pohl, P.; Sterpone, F.; van der Spoel, D.; Xu, Y.; Garcia, A. E. Water determines the structure and dynamics of proteins. *Chem. Rev.* **2016**, *116*, 7673–7697.

[13] Ball, P. Water is an active matrix of life for cell and molecular biology. *Proc. Natl. Acad. Sci. U. S. A.* **2017**, *114*, 13327–13335.

[14] Marcus, Y. Effect of Ions on the Structure of Water: Structure Making and Breaking. *Chem. Rev.* **2009**, *109*, 1346–1370.

[15] Marcus, Y. Effect of ions on the structure of water*. *Pure Appl. Chem.* **2010**, *82*, 1889–1899.

[16] Gurney, R. W. *Ionic Processes in Solution*; McGraw-Hill: New York, 1953.

[17] Marcus, Y. Ionic Radii in Aqueous Solutions. *Chem. Rev.* **1988**, *88*, 1475–1498.

[18] Ohtaki, H.; Radnai, T. Structure and dynamics of hydrated ions. *Chem. Rev.* **1993**, *93*, 1157–1204.

[19] Cota, R.; Ottosson, N.; Bakker, H. J.; Woutersen, S. Evidence for Reduced Hydrogen-Bond Cooperativity in Ionic Solvation Shells from Isotope-Dependent Dielectric Relaxation. *Phys. Rev. Lett.* **2018**, *120*, 216001.

[20] Atkins, P.; de Paula, J. *Physical chemistry*, 9th ed.; W. H. Freeman and Company: New York, 2010.

[21] Woutersen, S.; Bakker, H. J. Resonant intermolecular transfer of vibrational energy in liquid water. *Nature* **1999**, *402*, 507–509.

[22] Buchner, R. In *Nov. Approaches to Struct. Dyn. Liq. Exp. Theor. Simulations*; Samios, J., Durov, V. A., Eds.; Springer Netherlands: Dordrecht, 2004; pp 265–288.

[23] Loparo, J. J.; Fecko, C. J.; Eaves, J. D.; Roberts, S. T.; Tokmakoff, A. Reorientational and configurational fluctuations in water observed on molecular length scales. *Phys. Rev. B* **2004**, *70*, 1–4.

[24] Logsdon, S. D. Soil dielectric spectra from vector network analyzer data. *Soil Sci. Soc. Am. J.* **2005**, *69*, 983–989.

[25] Rezus, Y. L. A.; Bakker, H. J. On the orientational relaxation of HDO in liquid water. *J. Chem. Phys.* **2005**, *123*, 114502.

[26] Rezus, Y. L. A.; Bakker, H. J. Orientational dynamics of isotopically diluted H2O and D2O. *J. Chem. Phys.* **2006**, *125*, 144512.

[27] Buchner, R. What can be learnt from dielectric relaxation spectroscopy about ion solvation and association? *Pure Appl. Chem.* **2008**, *80*, 1239–1252.

[28] Thøgersen, J.; Jensen, S. K.; Petersen, C.; Keiding, S. R. Reorientation of hydroxide ions in water. *Chem. Phys. Lett.* **2008**, *466*, 1–5.

[29] Piatkowski, L.; Eisenthal, K. B.; Bakker, H. J. Ultrafast intermolecular energy transfer in heavy water. *Phys. Chem. Chem. Phys.* **2009**, *11*, 9033–9038.

[30] Prajapati, A. N.; Vyas, A. D.; Rana, V. A.; Bhatnagar, S. P. Dielectric relaxation and dispersion studies of mixtures of 1-propanol and benzonitrile in pure liquid state at radio and microwave frequencies. *J. Mol. Liq.* **2010**, *151*, 12–16.

[31] Timmer, R. L. A.; Tielrooij, K. J.; Bakker, H. J. Vibrational Förster transfer to hydrated protons. *J. Chem. Phys.* **2010**, *132*, 194504.

[32] Vyas, A. D.; Rana, V. A.; Bhatnagar, S. P.; Vashisth, V. M. Dielectric dispersion and relaxation mixtures of 1-butanol and phenol at lower microwave frequencies. *Indian J. Pure Appl. Phys.* **2011**, *49*, 47–52.

[33] Rahman, H. M. A.; Hefter, G.; Buchner, R. Hydration of Formate and Acetate Ions by Dielectric Relaxation Spectroscopy. *J. Phys. Chem. B* **2012**, *116*, 314–323.

[34] Ensing, W.; Hunger, J.; Ottosson, N.; Bakker, H. J. On the orientational mobility of water molecules in proton and sodium terminated nafion membranes. *J. Phys. Chem. C* **2013**, *117*, 12930–12935.

[35] Ermilova, E.; Bier, F. F.; Hölzel, R. Dielectric measurements of aqueous DNA solutions up to 110 GHz. *Phys. Chem. Chem. Phys.* **2014**, *16*, 11256–11264.

[36] Ottosson, N.; Hunger, J.; Bakker, H. J. Effect of cations on the hydrated proton. *J. Am. Chem. Soc.* **2014**, *136*, 12808–12811.

[37] Balos, V.; Bonn, M.; Hunger, J. Quantifying transient interactions between amide groups and the guanidinium cation. *Phys. Chem. Chem. Phys.* **2015**, *17*, 28539–28543.

[38] Baiz, C. R.; Tokmakoff, A. Structural disorder of folded proteins: Isotope-edited 2D IR spectroscopy and markov state modeling. *Biophys. J.* **2015**, *108*, 1747–1757.

[39] Stevenson, P.; Götz, C.; Baiz, C. R.; Akerboom, J.; Tokmakoff, A.; Vaziri, A. Visualizing KcsA conformational changes upon ion binding by infrared spectroscopy and atomistic modeling. *J. Phys. Chem. B* **2015**, *119*, 5824–5831.

[40] Shattuck, J.; Shah, P.; Erramilli, S.; Ziegler, L. D. Structure Making and Breaking Effects of Cations in Aqueous Solution: Nitrous Oxide Pump-Probe Measurements. *J. Phys. Chem. B* **2016**, *120*, 10569–10580.

[41] Zhang, X. X.; Jones, K. C.; Fitzpatrick, A.; Peng, C. S.; Feng, C. J.; Baiz, C. R.; Tokmakoff, A. Studying Protein-Protein Binding through T-Jump Induced Dissociation: Transient 2D IR Spectroscopy of Insulin Dimer. *J. Phys. Chem. B* **2016**, *120*, 5134–5145.

[42] Balos, V.; Bonn, M.; Hunger, J. Anionic and cationic Hofmeister effects are non-additive for guanidinium salts. *Phys. Chem. Chem. Phys.* **2017**, *19*, 9724–9728.

[43] Strudwick, B. H.; Zhang, J.; Hilbers, M. F.; Buma, W. J.; Woutersen, S.; Liu, S. H.; Hartl, F. Excited-State Electronic Asymmetry Prevents Photoswitching in Terthiophene Compounds. *Inorg. Chem.* **2018**, *57*, 9039–9047.

[44] Buchner, R.; Barthel, J.; Stauber, J. The dielectric relaxation of water between 0°C and 35°C. *Chem. Phys. Lett.* **1999**, *306*, 57–63.

[45] Buchner, R.; Hefter, G. T.; May, P. M. Dielectric Relaxation of Aqueous NaCl Solutions. *J. Phys. Chem. A* **1999**, *103*, 1–9.

[46] Buchner, R.; Hefter, G.; May, P. M.; Sipos, P. Dielectric relaxation of dilute aqueous NaOH, $NaAl(OH)_4$, and $NaB(OH)_4$. *J. Phys. Chem. B* **1999**, *103*, 11186–11190.

[47] Chen, T.; Hefter, G.; Buchner, R. Dielectric spectroscopy of aqueous solutions of KCl and CsCl. *J. Phys. Chem. A* **2003**, *107*, 4025–4031.

[48] Buchner, R.; Chen, T.; Hefter, G. Complexity in "simple" electrolyte solutions: Ion pairing in MgSO4(aq). *J. Phys. Chem. B* **2004**, *108*, 2365–2375.

[49] Chen, T.; Hefter, G.; Buchner, R. Ion association and hydration in aqueous solutions of nickel(II) and cobalt(II) sulfate. *J. Solution Chem.* **2005**, *34*, 1045–1066.

[50] Wachter, W.; Kunz, W.; Buchner, R.; Hefter, G. Is There an Anionic Hofmeister Effect on Water Dynamics? Dielectric Spectroscopy of Aqueous Solutions of NaBr, NaI, $NaNO_3$, $NaClO_4$, and NaSCN. *J. Phys. Chem. A* **2005**, *109*, 8675–8683.

[51] Wachter, W.; Fernandez, S.; Buchner, R.; Hefter, G. Ion association and hydration in aqueous solutions of LiCl and Li_2SO_4 by dielectric spectroscopy. *J. Phys. Chem. B* **2007**, *111*, 9010–7.

[52] Schrödle, S.; Rudolph, W. W.; Hefter, G.; Buchner, R. Ion association and hydration in 3:2 electrolyte solutions by dielectric spectroscopy: Aluminum sulfate. *Geochim. Cosmochim. Acta* **2007**, *71*, 5287–5300.

[53] Hunger, J.; Stoppa, A.; Thoman, A.; Walther, M.; Buchner, R. Broadband dielectric response of dichloromethane. *Chem. Phys. Lett.* **2009**,

[54] Tielrooij, K. J.; Hunger, J.; Buchner, R.; Bonn, M.; Bakker, H. J. Influence of concentration and temperature on the dynamics of water in the hydrophobic hydration shell of tetramethylurea. *J. Am. Chem. Soc.* **2010**, *132*, 15671–15678.

[55] Auer, B. M.; Skinner, J. L. Water: Hydrogen bonding and vibrational spectroscopy, in the bulk liquid and at the liquid/vapor interface. *Chem. Phys. Lett.* **2009**, *470*, 13–20.

[56] Bakker, H. J.; Skinner, J. L. Vibrational spectroscopy as a probe of structure and dynamics in liquid water. *Chem. Rev.* **2010**, *110*, 1498–1517.

[57] Omta, A. W.; Kropman, M. F.; Woutersen, S.; Bakker, H. J. Influence of ions on the hydrogen-bond structure in liquid water. *J. Chem. Phys.* **2003**, *119*, 12457–12461.

[58] Omta, A. W.; Kropman, M. F.; Woutersen, S.; Bakker, H. J. Negligible effect of ions on the hydrogen-bond structure in liquid water. *Science* **2003**, *301*, 347–349.

[59] van der Post, S. T.; Scheidelaar, S.; Bakker, H. J. Femtosecond study of the effects of ions on the reorientation dynamics of water. *J. Mol. Liq.* **2012**, *176*, 22–28.

[60] van der Post, S. T.; Bakker, H. J. The combined effect of cations and anions on the dynamics of water. *Phys. Chem. Chem. Phys.* **2012**, *14*, 6280–6288.

[61] van der Post, S. T.; Tielrooij, K.-J.; Hunger, J.; Backus, E. H. G.; Bakker, H. J. Femtosecond study of the effects of ions and hydrophobes on the dynamics of water. *Faraday Discuss.* **2013**, *160*, 171–189.

[62] Groot, C. C. M.; Bakker, H. J. Hydration dynamics of aqueous glucose probed with polarization-resolved fs-IR spectroscopy. *J. Chem. Phys.* **2014**, *140*, 234503.

[63] Groot, C. C.; Bakker, H. J. A femtosecond mid-infrared study of the dynamics of water in aqueous sugar solutions. *Phys. Chem. Chem. Phys.* **2015**, *17*, 8449–8458.

[64] Woutersen, S.; Bakker, H. J. Ultrafast vibrational and structural dynamics of the proton in liquid water. *Phys. Rev. Lett.* **2006**, *96*, 138305.

[65] Moilanen, D. E.; Spry, D. B.; Fayer, M. D. Water dynamics and proton transfer in nafion fuel cell membranes. *Langmuir* **2008**, *24*, 3690–3698.

[66] Peighambardoust, S. J.; Rowshanzamir, S.; Amjadi, M. Review of the proton exchange membranes for fuel cell applications. *Int. J. Hydrogen Energy* **2010**, *35*, 9349–9384.

[67] Liu, L.; Bakker, H. J. Vibrational excitation induced proton transfer in hydrated Nafion membranes. *J. Phys. Chem. B* **2015**, *119*, 2628–2637.

[68] Fournier, J. A.; Carpenter, W. B.; Lewis, N. H.; Tokmakoff, A. Broadband 2D IR spectroscopy reveals dominant asymmetric H5O2+ proton hydration structures in acid solutions. *Nat. Chem.* **2018**, *10*, 932–937.

[69] Roberts, S. T.; Petersen, P. B.; Ramasesha, K.; Tokmakoff, A.; Ufimtsev, I. S.; Martinez, T. J. Observation of a Zundel-like transition state during proton transfer in aqueous hydroxide solutions. *Proc. Natl. Acad. Sci.* **2009**, *106*, 15154–15159.

[70] Roberts, S. T.; Ramasesha, K.; Petersen, P. B.; Mandal, A.; Tokmakoff, A. Proton transfer in concentrated aqueous hydroxide visualized using ultrafast infrared spectroscopy. *J. Phys. Chem. A* **2011**, *115*, 3957–3972.

[71] Mandal, A.; Ramasesha, K.; De Marco, L.; Tokmakoff, A. Collective vibrations of water-solvated hydroxide ions investigated with broadband 2DIR spectroscopy. *J. Chem. Phys.* **2014**, *140*, 204508.

[72] Mandal, A.; Tokmakoff, A. Vibrational dynamics of aqueous hydroxide solutions probed using broadband 2DIR spectroscopy. *J. Chem. Phys.* **2015**, *143*, 194501.

[73] Biswas, R.; Carpenter, W.; Fournier, J. A.; Voth, G. A.; Tokmakoff, A. IR spectral assignments for the hydrated excess proton in liquid water. *J. Chem. Phys.* **2017**, *146*, 154507.

[74] Marx, D.; Chandra, A.; Tuckerman, M. E. Aqueous basic solutions: Hydroxide solvation, structural diffusion, and comparison to the hydrated proton. *Chem. Rev.* **2010**, *110*, 2174–2216.

[75] Tuckerman, M. E.; Marx, D.; Parrinello, M. The nature and transport mechanism of hydrated hydroxide ions in aqueous solution. *Nature* **2002**, *417*, 925–929.

[76] Chen, B.; Ivanov, I.; Park, J. M.; Parrinello, M.; Klein, M. L. Solvation Structure and Mobility Mechanism of OH-: A Car-Parrinello Molecular Dynamics Investigation of Alkaline Solutions. *J. Phys. Chem. B* **2002**, *106*, 12006–12016.

[77] Sun, X.; Yoo, S.; Xantheas, S. S.; Dang, L. X. The reorientation mechanism of hydroxide ions in water: A molecular dynamics study. *Chem. Phys. Lett.* **2009**, *481*, 9–16.

[78] Bucher, D.; Gray-Weale, A.; Kuyucak, S. Ab Initio Study of Water Polarization in the Hydration Shell of Aqueous Hydroxide: Comparison between Polarizable and Nonpolarizable Water Models. *J. Chem. Theory Comput.* **2010**, *6*, 2888–2895.

[79] Hassanali, A.; Prakash, M. K.; Eshet, H.; Parrinello, M. On the recombination of hydronium and hydroxide ions in water. *Proc. Natl. Acad. Sci.* **2011**, *108*, 20410–20415.

[80] Roberts, S. T.; Mandal, A.; Tokmakoff, A. Local and Collective Reaction Coordinates in the Transport of the Aqueous Hydroxide Ion. *J. Phys. Chem. B* **2014**, *118*, 8062–8069.

[81] Chen, M.; Zheng, L.; Santra, B.; Ko, H. Y.; Distasio, R. A.; Klein, M. L.; Car, R.; Wu, X. Hydroxide diffuses slower than hydronium in water because its solvated structure inhibits correlated proton transfer. *Nat. Chem.* **2018**, *10*, 413–419.

[82] Jackson, J. D. *Classical Electrodynamics*, 3rd ed.; Wiley: New York, 1999.

[83] Ghowsi, K.; Gale, R. J. Some Aspects of the High Frequency Conductance of Electrolytes. *J. Electrochem. Soc.* **1989**, *136*, 2806–2811.

[84] Anderson, J. The Debye-Falkenhagen effect: experimental fact or friction? *J. Non. Cryst. Solids* **1994**, *172-174*, 1190–1194.

[85] Ellison, W. J.; Lamkaouchi, K.; Moreau, J. M. Water: A dielectric reference. *J. Mol. Liq.* **1996**, *68*, 171–279.

[86] Lileev, A. S.; Loginova, D. V.; Lyashchenko, A. K. Dielectric properties of aqueous hydrochloric acid solutions. *Mendeleev Commun.* **2007**, *17*, 364–365.

[87] Debye, P. *Polar molecules*; The Chemical Catalog: New York, 1929.

[88] Evans, M. W.; Evans, G. J.; Coffey, W. T.; Grigolini, P. *Molecular Dynamics*; Wiley: New York, 1982.

[89] Lorentz, H. A. *The theory of electrons*, 2nd ed.; B.G. Teubner: Leipzig, 1916.

[90] Choy, T. C. *Effective Medium Theory: Principles and Applications*; Clarendon Press: Oxford, 1999.

[91] Christopher Longuet-Higgins, H.; Fisher, M. E. Lars Onsager: November 27, 1903–October 5, 1976. *J. Stat. Phys.* **1995**, *78*, 605–640.

[92] Onsager, L. Electric moments of molecules in liquids. *J. Am. Chem. Soc.* **1936**, *58*, 1486–1493.

[93] Böttcher, C. *Theory of Electric Polarization*, 2nd ed.; Elsevier: Amsterdam, 1973.

[94] Wilson, J. N. The dielectric constants of polar liquids. *Chem. Rev.* **1939**, *25*, 377–406.

[95] Kirkwood, J. G. The Dielectric Polarization of Polar Liquids. *J. Chem. Phys.* **1939**, *7*, 911.

[96] Fröhlich, H. *Theory of dielectrics: dielectrics constant and dielectric loss*, 2nd ed.; Clarendon Press: Oxford, 1986.

[97] Debye, P. Part I. Dielectric constant. Energy absorption in dielectrics with polar molecules. *Trans. Faraday Soc.* **1934**, *30*, 679–684.

[98] Havriliak, S.; Negami, S. A complex plane analysis of α-dispersions in some polymer systems. *J. Polym. Sci. Part C Polym. Symp.* **1966**, *14*, 99–117.

[99] Cole, K. S.; Cole, R. H. Dispersion and absorption in dielectrics I. Alternating current characteristics. *J. Chem. Phys.* **1941**, *9*, 341–351.

[100] Cole, R. H. On the analysis of dielectric relaxation measurements. *J. Chem. Phys.* **1955**, *23*, 493–499.

[101] Kaatze, U. Dielectric spectroscopy of aqueous solutions. Hydration phenomena and hydrogen-bonded networks. *J. Mol. Liq.* **1993**, *56*, 95–115.

[102] Nortemann, K.; Hilland, J.; Kaatze, U. Dielectric Properties of Aqueous NaCl Solutions at Microwave Frequencies. *J. Phys. Chem. A* **1997**, *101*, 6864–6869.

[103] Smit, W. J.; van Dam, E. P.; Cota, R.; Bakker, H. J. Caffeine and taurine slow down water molecules. *J. Phys. Commun.* **2019**, *3*, 025010.

[104] Liszi, J.; Felinger, A.; Kristóf, E. H. Static relative permittivity of electrolyte solutions. *Electrochim. Acta* **1988**, *33*, 1191–1194.

[105] Impey, R. W.; Madden, P. A.; McDonald, I. R. Hydration and mobility of ions in solution. *J. Phys. Chem.* **1983**, *87*, 5071–5083.

[106] Barthel, J.; Hetzenauer, H.; Buchner, R. Dielectric relaxation of aqueous electrolyte solutions. I. Solvent relaxation of 1:2, 2:1, and 2:2 electrolyte solutions. *Ber. Bunsen-Ges. Phys. Chem.* **1992**, *96*, 988–997.

[107] Guardia, E.; Padro, J. A. Molecular dynamics simulation of single ions in aqueous solutions: effects of the flexibility of the water molecules. *J. Phys. Chem.* **1990**, *94*, 6049–6055.

[108] Smith, D. E.; Dang, L. X. Computer simulations of NaCl association in polarizable water. *J. Chem. Phys.* **1994**, *100*, 3757–3766.

[109] Hubbard, J. B.; Onsager, L.; van Beek, W. M.; Mandel, M. Kinetic polarization deficiency in electrolyte solutions. *Proc. Natl. Acad. Sci. U. S. A.* **1977**, *74*, 401–404.

[110] Hubbard, J.; Onsager, L. Dielectric dispersion and dielectric friction in electrolyte solutions. I. *J. Chem. Phys.* **1977**, *67*, 4850.

[111] Hubbard, J. B. Dielectric dispersion and dielectric friction in electrolyte solutions. II. *J. Chem. Phys.* **1978**, *68*, 1649.

[112] Hubbard, J. B.; Colonomos, P.; Wolynes, P. G. Molecular theory of solvated ion dynamics. III. The kinetic dielectric decrement. *J. Chem. Phys.* **1979**, *71*, 2652.

[113] van der Zwan, G.; Hynes, J. Dynamical polar solvent effects on solution reactions: A simple continuum model. *J. Chem. Phys.* **1982**, *76*, 2993.

[114] van der Zwan, G.; Hynes, J. T. Polarization diffusion and dielectric friction. *Physica A* **1983**, *121*, 227–252.

[115] Tielrooij, K. J.; Timmer, R. L.; Bakker, H. J.; Bonn, M. Structure dynamics of the proton in liquid water probed with terahertz time-domain spectroscopy. *Phys. Rev. Lett.* **2009**, *102*, 198303.

[116] Sega, M.; Kantorovich, S.; Arnold, A. Kinetic dielectric decrement revisited: phenomenology of finite ion concentrations. *Phys. Chem. Chem. Phys.* **2014**, *17*, 130–133.

[117] Hall, D. G.; Cole, R. H. Dielectric polarization of sulfuric acid solutions. *J. Phys. Chem.* **1981**, *85*, 1065–1069.

[118] Kaatze, U. The dielectric properties of water in its different states of interaction. *J. Solution Chem.* **1997**, *26*, 1049–1112.

[119] Blackham, D. V.; Pollard, R. D. An improved technique for permittivity measurements using a coaxial probe. *IEEE Trans. Instrum. Meas.* **1997**, *46*, 1093–1099.

[120] Hunger, J. Effects of Polar Compounds on the Dynamics and Dielectric Properties of Room-Temperature Ionic Liquids. Ph.D. thesis, Universität Regensburg, 2009.

[121] Wang, Z.; Pakoulev, A.; Pang, Y.; Dlott, D. D. Vibrational substructure in the OH stretching transition of water and HOD. *J. Phys. Chem. A* **2004**, *108*, 9054–9063.

[122] Perakis, F.; Marco, L. D.; Shalit, A.; Tang, F.; Kann, Z. R.; Kühne, T. D.; Torre, R.; Bonn, M.; Nagata, Y. Vibrational Spectroscopy and Dynamics of Water. *Chem. Rev.* **2016**, *116*, 7590–7607.

[123] Sakurai, J. J. *Modern quantum mechanics*, rev. ed.; Addison-Wesley: Reading, MA, 1994.

[124] Maksyutenko, P.; Grechko, M.; Rizzo, T. R.; Boyarkin, O. V. State-resolved spectroscopy of high vibrational levels of water up to the dissociative continuum. *Philos. Trans. R. Soc. A Math. Phys. Eng. Sci.* **2012**, *370*, 2710–2727.

[125] Morse, P. M. Diatomic molecules according to the wave mechanics. II. Vibrational levels. *Phys. Rev.* **1929**, *34*, 57–64.

[126] Le Roy, R. J.; Dattani, N. S.; Coxon, J. A.; Ross, A. J.; Crozet, P.; Linton, C. Accurate analytic potentials for $Li_2(X^1\Sigma_g^+)$ and $Li_2(A^1\Sigma_u^+)$ from 2 to 90 Å, and the radiative lifetime of Li(2p). *J. Chem. Phys.* **2009**, *131*, 204309.

[127] Lipari, G.; Szabo, A. Effect of librational motion on fluorescence depolarization and nuclear magnetic resonance relaxation in macromolecules and membranes. *Biophys. J.* **1980**, *30*, 489–506.

[128] Griffiths, P. R.; De Haseth, J. A. *Fourier Transform Infrared Spectrom. Second Ed.*; 2006.

[129] Förster, T. Zwischenmolekulare Energiewanderung und Fluoreszenz. *Ann. Phys.* **1948**, *437*, 55–75.

[130] Lynden-Bell, R. M.; Rasaiah, J. C. Mobility and solvation of ions in channels. *J. Chem. Phys.* **1996**, *105*, 9266–9280.

[131] Chakraborty, S. Order Parameter Description of Electrochemical-Hydrodynamic Interactions in Nanochannels. *Phys. Rev. Lett.* **2008**, *101*, 184501.

[132] Zwolak, M.; Lagerqvist, J.; Di Ventra, M. Quantized Ionic Conductance in Nanopores. *Phys. Rev. Lett.* **2009**, *103*, 128102.

[133] French, M.; Hamel, S.; Redmer, R. Dynamical screening and ionic conductivity in water from ab initio simulations. *Phys. Rev. Lett.* **2011**, *107*, 185901.

[134] Yin, H.; Ma, Y.; Mu, J.; Liu, C.; Rohlfing, M. Charge-Transfer Excited States in Aqueous DNA: Insights from Many-Body Green's Function Theory. *Phys. Rev. Lett.* **2014**, *112*, 228301.

[135] Fahrenberger, F.; Hickey, O. A.; Smiatek, J.; Holm, C. Importance of Varying Permittivity on the Conductivity of Polyelectrolyte Solutions. *Phys. Rev. Lett.* **2015**, *115*, 118301.

[136] Minoguchi, A.; Richert, R.; Angell, C. A. Dielectric Studies Deny Existence of Ultraviscous Fragile Water. *Phys. Rev. Lett.* **2004**, *93*, 215703.

[137] Nakanishi, M.; Griffin, P.; Mamontov, E.; Sokolov, A. P. No fragile-to-strong crossover in LiCl-H 2O solution. *J. Chem. Phys.* **2012**, *136*, 124512.

[138] Perticaroli, S.; Nakanishi, M.; Pashkovski, E.; Sokolov, A. P. Dynamics of Hydration Water in Sugars and Peptides Solutions. *J. Phys. Chem. B* **2013**, *117*, 7729–7736.

[139] Popov, I.; Greenbaum (Gutina), A.; Sokolov, A. P.; Feldman, Y. The puzzling first-order phase transition in water–glycerol mixtures. *Phys. Chem. Chem. Phys.* **2015**, *17*, 18063–18071.

[140] Onsager, L. Electric Moments of Molecules in Liquids. *J. Am. Chem. Soc.* **1936**, *58*, 1486–1493.

[141] Robinson, R. A.; Stokes, R. H. *Electrolyte Solutions: Second Revised Edition*; Dover Publications, Inc.: New York, 2002.

[142] Kay, R. L.; Evans, D. F. The Effect of Solvent Structure on the Mobility of Symmetrical Ions in Aqueous Solution. *J. Phys. Chem.* **1966**, *70*, 2325–2335.

[143] Hertz, H. G.; Holz, M.; Mills, R. The effect of structure on ion self-diffusion in concentrated electrolyte solutions. *J. Chim. Phys.* **1974**, *71*, 1355–1362.

[144] Hertz, H. G.; Mills, R. The effect of structure on self-diffusion in concentrated electrolytes : relationship between the water and ionic self-diffusion coefficients. *J. Chim. Phys.* **1976**, *73*, 499–508.

[145] Harris, K.; Hertz, H.; Mills, R. The effect of structure on self-diffusion in concentrated electrolytes : relationship between the water and ionic self-diffusion coefficients for structure-forming salts. *J. Chim. Phys.* **1978**, *75*, 391–396.

[146] Bakker, H. J. Water dynamics: Ion-ing out the details. *Nat. Chem.* **2009**, *1*, 24–25.

[147] Lin, Y.-S.; Auer, B. M.; Skinner, J. L. Water structure, dynamics, and vibrational spectroscopy in sodium bromide solutions. *J. Chem. Phys.* **2009**, *131*, 144511.

[148] Jungwirth, P.; Cremer, P. S. Beyond Hofmeister. *Nat. Chem.* **2014**, *6*, 261–263.

[149] Schienbein, P.; Schwaab, G.; Forbert, H.; Havenith, M.; Marx, D. Correlations in the Solute–Solvent Dynamics Reach Beyond the First Hydration Shell of Ions. *J. Phys. Chem. Lett.* **2017**, *8*, 2373–2380.

[150] Bianchi, H.; Corti, H. R.; Fernández-Prini, R. The conductivity of concentrated aqueous mixtures of NaCl and $MgCl_2$ at 25^{o}C. *J. Solution Chem.* **1989**, *18*, 485–491.

[151] Clough, S. A. Dipole moment of water from Stark measurements of H2O, HDO, and D2O. *J. Chem. Phys.* **1973**, *59*, 2254.

[152] Richens, D. T. *The chemistry of aqua ions*; J. Wiley: New York, 1997.

[153] White, J. A.; Schwegler, E.; Galli, G.; Gygi, F. The solvation of Na+ in water: First-principles simulations. *J. Chem. Phys.* **2000**, *113*, 4668.

[154] Varma, S.; Rempe, S. B. Coordination numbers of alkali metal ions in aqueous solutions. *Biophys. Chem.* **2006**, *124*, 192–199.

[155] Mason, P. E.; Ansell, S.; Neilson, G. W. Neutron diffraction studies of electrolytes in null water: a direct determination of the first hydration zone of ions. *J. Phys. Condens. Matter* **2006**, *18*, 8437–8447.

[156] Rowley, C. N.; Roux, B. The solvation structure of Na^+ and K^+ in liquid water determined from high level ab initio molecular dynamics simulations. *J. Chem. Theory Comput.* **2012**, *8*, 3526–3535.

[157] Kiriukhin, M. Y.; Collins, K. D. Dynamic hydration numbers for biologically important ions. *Biophys. Chem.* **2002**, *99*, 155–168.

[158] Richens, D. T. Ligand substitution reactions at inorganic centers. *Chem. Rev.* **2005**, *105*, 1961–2002.

[159] Ding, Y.; Hassanali, A. A.; Parrinello, M. Anomalous water diffusion in salt solutions. *Proc. Natl. Acad. Sci.* **2014**, *111*, 3310–3315.

[160] Hayes, R.; Warr, G. G.; Atkin, R. Structure and Nanostructure in Ionic Liquids. *Chem. Rev.* **2015**, *115*, 6357–6426.

[161] Morgenstern, K.; Marx, D.; Havenith, M.; Muhler, M. Editorial of the PCCP themed issue on "Solvation Science". *Phys. Chem. Chem. Phys.* **2015**, *17*, 8295–8296.

[162] Bockris, J. O.; Reddy, A. K. N. *Modern Electrochemistry: Ionics*, 2nd ed.; Kluwer Academic, 2002.

[163] Kaatze, U.; Behrends, R.; Pottel, R. Hydrogen network fluctuations and dielectric spectrometry of liquids. *J. Non. Cryst. Solids* **2002**, *305*, 19–28.

[164] Hoang, M.-Q.; Le Roy, S.; Boudou, L.; Teyssedre, G. Implementation of polarization processes in a charge transport model applied on poly (ethylene naphthalate) films. *J. Appl. Phys.* **2016**, *119*, 224105.

[165] Marcus, Y. Concentration dependence of ionic hydration numbers. *J. Phys. Chem. B* **2014**, *118*, 10471–10476.

[166] Marcus, Y. Thermodynamics of solvation of ions. Part 5.—Gibbs free energy of hydration at 298.15 K. *J. Chem. Soc., Faraday Trans.* **1991**, *87*, 2995–2999.

[167] Tongraar, A.; Liedl, K. R.; Rode, B. M. Born-Oppenheimer ab initio QM/MM dynamics simulations of Na^+ and K^+ in water: From structure making to structure breaking effects. *J. Phys. Chem. A* **1998**, *102*, 10340–10347.

[168] Mancinelli, R.; Botti, A.; Bruni, F.; Ricci, M. A.; Soper, A. K. Perturbation of water structure due to monovalent ions in solution. *Phys. Chem. Chem. Phys.* **2007**, *9*, 2959–2967.

[169] Markovitch, O.; Agmon, N. Structure and Energetics of the Hydronium Hydration Shells. *J. Phys. Chem. A* **2007**, *111*, 2253–2256.

[170] Cox, M. J.; Bakker, H. J. Parallel proton transfer pathways in aqueous acid-base reactions. *J. Chem. Phys.* **2008**, *128*, 174501.

[171] Berkelbach, T. C.; Lee, H.-S.; Tuckerman, M. E. Concerted Hydrogen-Bond Dynamics in the Transport Mechanism of the Hydrated Proton: A First-Principles Molecular Dynamics Study. *Phys. Rev. Lett.* **2009**, *103*, 238302.

[172] de Grotthuss, C. J. T. Memoir on the decomposition of water and of the bodies that it holds in solution by means of galvanic electricity. 1805. *Biochim. Biophys. Acta* **2006**, *1757*, 871–5.

[173] Agmon, N. The Grotthuss mechanism. *Chem. Phys. Lett.* **1995**, *244*, 456–462.

[174] Hückel, E. 3. Einzelvorträge: Elektrochemie. Theorie der Beweglichkeiten des Wasserstoff- und Hydroxylions in Wässriger Lösung. *Zeitschrift für Elektrochemie und Angew. Phys. Chemie* **1928**, *34*, 546–562.

[175] Danneel, H. Notiz über Ionengeschwindigkeiten. *Zeitschrift für Elektrotechnik und Elektrochemie* **1905**, *11*, 249–252.

[176] Conway, B. E.; Bockris, J. O.; Linton, H. Proton Conductance and the Existence of the H3O - Ion. *J. Chem. Phys.* **1956**, *24*, 834.

[177] Lengyel, S.; Conway, B. *Proton solvation and proton transfer in chemical and electrochemical processes*; United States: Plenum Press, 1983.

[178] Kaatze, U.; Giese, K. Dielectric relaxation spectroscopy of liquids: frequency domain and time domain experimental methods. *J. Phys. E.* **1980**, *13*, 133–141.

[179] Marx, D.; Tuckerman, M. E.; Hutter, J.; Parrinello, M. The nature of the hydrated excess proton in water. *Nature* **1999**, *397*, 601–604.

[180] Bard, A. J.; Faulkner, L. R. *Electrochemical methods: Fundamentals and Applications*, 2nd ed.; Wiley: New York, 2001.

[181] Dryfe, R. A. W. In *Handb. Electrochem.*; Zoski, C. G., Ed.; Elsevier: Amsterdam, 2007; pp 849–877.

[182] Lapid, H.; Agmon, N.; Petersen, M. K.; Voth, G. A. A bond-order analysis of the mechanism for hydrated proton mobility in liquid water. *J. Chem. Phys.* **2005**, *122*, 014506.

[183] Kresge, A. What Makes Proton Transfer Fast? *Acc. Chem. Res.* **1975**, *8*, 354–360.

[184] Cukierman, S.; Quigley, E. P.; Crumrine, D. S. Proton conduction in gramicidin A and in its dioxolane-linked dimer in different lipid bilayers. *Biophys. J.* **1997**, *73*, 2489–2502.

[185] Pomès, R. Theoretical studies of the Grotthuss mechanism in biological proton wires. *Isr. J. Chem.* **1999**, *39*, 387–395.

[186] Brewer, M. L.; Schmitt, U. W.; Voth, G. A. The Formation and Dynamics of Proton Wires in Channel Environments. *Biophys. J.* **2001**, *80*, 1691–1702.

[187] Pomès, R.; Roux, B. Molecular Mechanism of H+ Conduction in the Single-File Water Chain of the Gramicidin Channel. *Biophys. J.* **2002**, *82*, 2304–2316.

[188] Blomberg, M. R. A.; Siegbahn, P. E. M.; Brewer, M. L.; Schmitt, U. W.; Voth, G. A.; Cukierman, S.; Quigley, E. P.; Crumrine, D. S.; Kresge, A. J. Proton conduction in gramicidin A and in its dioxolane-linked dimer in different lipid bilayers. *Biophys. J.* **2006**, *1757*, 2489–2502.

[189] Swanson, J. M.; Maupin, C. M.; Chen, H.; Petersen, M. K.; Xu, J.; Wu, Y.; Voth, G. A. Proton solvation and transport in aqueous and biomolecular systems: Insights from computer simulations. *J. Phys. Chem. B* **2007**, *111*, 4300–4314.

[190] Hibbs, M. R.; Hickner, M. A.; Alam, T. M.; McIntyre, S. K.; Fujimoto, C. H.; Cornelius, C. J. Transport Properties of Hydroxide and Proton Conducting Membranes. *Chem. Mater.* **2008**, *20*, 2566–2573.

[191] Pan, J.; Chen, C.; Zhuang, L.; Lu, J. Designing Advanced Alkaline Polymer Electrolytes for Fuel Cell Applications. *Acc. Chem. Res.* **2012**, *45*, 473–481.

[192] Deng, H.; Huo, S.; Chang, Y.; Zhou, Y.; Jiao, K. Transient analysis of alkaline anion exchange membrane fuel cell anode. *Int. J. Hydrogen Energy* **2013**, *38*, 6509–6525.

[193] Mohammed, O. F.; Pines, D.; Dreyer, J.; Pines, E.; Nibbering, E. T. J. Sequential Proton Transfer Through Water Bridges in Acid-Base Reactions. *Science* **2005**, *310*, 83–86.

[194] Maupin, C. M.; Aradi, B.; Voth, G. A. The Self-Consistent Charge Density Functional Tight Binding Method Applied to Liquid Water and the Hydrated Excess Proton: Benchmark Simulations. *J. Phys. Chem. B* **2010**, *114*, 6922–6931.

[195] Lee, S. H.; Rasaiah, J. C. Proton transfer and the mobilities of the H+ and OH− ions from studies of a dissociating model for water. *J. Chem. Phys.* **2011**, *135*, 124505.

[196] Meng, X.; Guo, J.; Peng, J.; Chen, J.; Wang, Z.; Shi, J. R.; Li, X. Z.; Wang, E. G.; Jiang, Y. Direct visualization of concerted proton tunnelling in a water nanocluster. *Nat. Phys.* **2015**, *11*, 235–239.

[197] Wolke, C. T.; Fournier, J. A.; Dzugan, L. C.; Fagiani, M. R.; Odbadrakh, T. T.; Knorke, H.; Jordan, K. D.; McCoy, A. B.; Asmis, K. R.; Johnson, M. A. Spectroscopic snapshots of the proton-transfer mechanism in water. *Science* **2016**, *354*, 1131–1135.

[198] Agmon, N. Mechanism of hydroxide mobility. *Chem. Phys. Lett.* **2000**, *319*, 247–252.

[199] Asthagiri, D.; Pratt, L. R.; Kress, J. D.; Gomez, M. A. The hydration state of HO−(aq). *Chem. Phys. Lett.* **2003**, *380*, 530–535.

[200] Nienhuys, H.-K.; Lock, A. J.; van Santen, R. A.; Bakker, H. J. Dynamics of water molecules in an alkaline environment. *J. Chem. Phys.* **2002**, *117*, 8021–8029.

[201] Kropman, M. F.; Bakker, H. J. Dynamics of water molecules in aqueous solvation shells. *Science* **2001**, *291*, 2118–2120.

[202] Kropman, M. F.; Nienhuys, H.-K.; Bakker, H. J. Real-Time Measurement of the Orientational Dynamics of Aqueous Solvation Shells in Bulk Liquid Water. *Phys. Rev. Lett.* **2002**, *88*, 77601.

[203] Woutersen, S.; Emmerichs, U.; Nienhuys, H.-K.; Bakker, H. J. Anomalous Temperature Dependence of Vibrational Lifetimes in Water and Ice. *Phys. Rev. Lett.* **1998**, *81*, 1106–1109.

[204] Roberts, S. T.; Loparo, J. J.; Tokmakoff, A. Characterization of spectral diffusion from two-dimensional line shapes. *J. Chem. Phys.* **2006**, *125*, 84502.

[205] Liu, L.; Hunger, J.; Bakker, H. J. Energy Relaxation Dynamics of the Hydration Complex of Hydroxide. *J. Phys. Chem. A* **2011**, *115*, 14593–14598.

[206] Steinel, T.; Asbury, J. B.; Zheng, J.; Fayer, M. D. Watching hydrogen bonds break: A transient absorption study of water. *J. Phys. Chem. A* **2004**, *108*, 10957–10964.

[207] Park, S.; Odelius, M.; Gaffney, K. J. Ultrafast Dynamics of Hydrogen Bond Exchange in Aqueous Ionic Solutions. *J. Phys. Chem. B* **2009**, *113*, 7825–7835.

[208] Tielrooij, K. J.; Garcia-Araez, N.; Bonn, M.; Bakker, H. J. Cooperativity in ion hydration. *Science* **2010**, *328*, 1006–1009.

[209] Deàk, J. C.; Rhea, S. T.; Iwaki, L. K.; Dlott, D. D. Vibrational energy relaxation and spectral diffusion in water and deuterated water. *J. Phys. Chem. A* **2000**, *104*, 4866–4875.

[210] Elsaesser, T. Ultrafast memory loss and relaxation processes in hydrogen-bonded systems. *Biol. Chem.* **2009**, *390*, 1125–1132.

[211] Fang, C.; Senes, A.; Cristian, L.; DeGrado, W. F.; Hochstrasser, R. M. Amide vibrations are delocalized across the hydrophobic interface of a transmembrane helix dimer. *Proc. Natl. Acad. Sci. U. S. A.* **2006**, *103*, 16740–16745.

[212] Bonn, M.; Hess, C.; Wolf, M. The dynamics of vibrational excitations on surfaces: CO on Ru(001). *J. Chem. Phys.* **2001**, *115*, 7725–7735.

[213] Roeterdink, W. G.; Berg, O.; Bonn, M. Frequency-and time-domain femtosecond vibrational sum frequency generation from CO adsorbed on Pt(111). *J. Chem. Phys.* **2004**, *121*, 10174–10180.

[214] Perkins, S. J. Protein volumes and hydration effects: The calculations of partial specific volumes, neutron scattering matchpoints and 280-nm absorption coefficients for proteins and glycoproteins from amino acid sequences. *Eur. J. Biochem.* **1986**, *157*, 169–180.

[215] Chen, X.; Weber, I.; Harrison, R. W. Hydration water and bulk water in proteins have distinct properties in radial distributions calculated from 105 atomic resolution crystal structures. *J. Phys. Chem. B* **2008**, *112*, 12073–12080.

[216] Thämer, M.; De Marco, L.; Ramasesha, K.; Mandal, A.; Tokmakoff, A. Ultrafast 2D IR spectroscopy of the excess proton in liquid water. *Science* **2015**, *350*, 78–82.

[217] Kratochvil, H. T.; Carr, J. K.; Matulef, K.; Annen, A. W.; Li, H.; Maj, M.; Ostmeyer, J.; Serrano, A. L.; Raghuraman, H.; Moran, S. D.; Skinner, J. L.; Perozo, E.; Roux, B.; Valiyaveetil, F. I.; Zanni, M. T. Instantaneous ion configurations in the K+ion channel selectivity filter revealed by 2D IR spectroscopy. *Science* **2016**, *353*, 1040–1044.

[218] Schwaab, G.; Sebastiani, F.; Havenith, M. Ion Hydration and Ion Pairing as Probed by THz Spectroscopy. *Angew. Chemie Int. Ed.* **2019**, *58*, 3000–3013.

[219] Comez, L.; Paolantoni, M.; Sassi, P.; Corezzi, S.; Morresi, A.; Fioretto, D. Molecular properties of aqueous solutions: A focus on the collective dynamics of hydration water. *Soft Matter* **2016**, *12*, 5501–5514.

[220] Graziano, G. Hydrophobicity of benzene. *Biophys. Chem.* **1999**, *82*, 69–79.

[221] Ghosh, D.; Roy, A.; Seidel, R.; Winter, B.; Bradforth, S.; Krylov, A. I. First-principle protocol for calculating ionization energies and redox potentials of solvated molecules and ions: Theory and application to aqueous phenol and phenolate. *J. Phys. Chem. B* **2012**, *116*, 7269–7280.

[222] Heal, M. R.; Harrison, M. A.; Neil Cape, J. Aqueous-phase nitration of phenol by N_2O_5 and $ClNO_2$. *Atmos. Environ.* **2007**, *41*, 3515–3520.

[223] Rayne, S.; Forest, K.; Friesen, K. J. Mechanistic aspects regarding the direct aqueous environmental photochemistry of phenol and its simple halogenated derivatives. A review. *Environ. Int.* **2009**, *35*, 425–437.

[224] Lajiness, J. P.; Robertson, W. M.; Dunwiddie, I.; Broward, M. A.; Vielhauer, G. A.; Weir, S. J.; Boger, D. L. Design, synthesis, and evaluation of duocarmycin O-amino phenol prodrugs subject to tunable reductive activation. *J. Med. Chem.* **2010**, *53*, 7731–7738.

[225] Li, Z.; Bao, X.; Bai, X.; Zhang, G.; Wang, J.; Zhu, M.; Wang, Y.; Shang, J.; Sheng, C.; Zhang, D.; Wang, Y. Design, Synthesis, and Biological Evaluation of Phenol Bioisosteric Analogues of 3-Hydroxymorphinan. *Sci. Rep.* **2019**, *9*, 2247.

[226] Rao, Y.; Subir, M.; McArthur, E. A.; Turro, N. J.; Eisenthal, K. B. Organic ions at the air/water interface. *Chem. Phys. Lett.* **2009**, *477*, 241–244.

[227] Lu, X.; Han, J.; Shephard, N.; Rhodes, S.; Martin, A. D.; Li, D.; Xue, G.; Chen, Z. Phenolic resin surface restructuring upon exposure to humid air: A sum frequency generation vibrational spectroscopic study. *J. Phys. Chem. B* **2009**, *113*, 12944–12951.

[228] Kusaka, R.; Ishiyama, T.; Nihonyanagi, S.; Morita, A.; Tahara, T. Structure at the air/water interface in the presence of phenol: a study using heterodyne-detected vibrational sum frequency generation and molecular dynamics simulation. *Phys. Chem. Chem. Phys.* **2018**, *20*, 3002–3009.

[229] Minofar, B.; Jungwirth, P.; Das, M. R.; Kunz, W.; Mahiuddin, S. Propensity of formate, acetate, benzoate, and phenolate for the aqueous solution/vapor interface: Surface tension measurements and molecular dynamics simulations. *J. Phys. Chem. C* **2007**, *111*, 8242–8247.

[230] The CP2K developers group, *http://www.cp2k.org.*

[231] VandeVondele, J.; Krack, M.; Mohamed, F.; Parrinello, M.; Chassaing, T.; Hutter, J. Quickstep: Fast and accurate density functional calculations using a mixed Gaussian and plane waves approach. *Comput. Phys. Commun.* **2005**, *167*, 103–128.

[232] Becke, A. D. Density-functional exchange-energy approximation with correct asymptotic behavior. *Phys. Rev. A* **1988**, *38*, 3098–3100.

[233] Lee, C.; Yang, W.; Parr, R. G. Development of the Colle-Salvetti correlation-energy formula into a functional of the electron density. *Phys. Rev. B* **1988**, *37*, 785–789.

[234] Grimme, S.; Antony, J.; Ehrlich, S.; Krieg, H. A consistent and accurate ab initio parametrization of density functional dispersion correction (DFT-D) for the 94 elements H-Pu. *J. Chem. Phys.* **2010**, *132*, 154104.

[235] VandeVondele, J.; Hutter, J. Gaussian basis sets for accurate calculations on molecular systems in gas and condensed phases. *J. Chem. Phys.* **2007**, *127*, 114105.

[236] Goedecker, S.; Teter, M.; Hutter, J. Separable dual-space Gaussian pseudopotentials. *Phys. Rev. B* **1996**, *54*, 1703–1710.

[237] Bussi, G.; Donadio, D.; Parrinello, M. Canonical sampling through velocity rescaling. *J. Chem. Phys.* **2007**, *126*, 014101.

[238] Pérez de Alba Ortíz, A.; Tiwari, A.; Puthenkalathil, R. C.; Ensing, B. Advances in enhanced sampling along adaptive paths of collective variables. *J. Chem. Phys.* **2018**, *149*, 072320.

[239] Park, J. M.; Laio, A.; Iannuzzi, M.; Parrinello, M. Dissociation mechanism of acetic acid in water. *J. Am. Chem. Soc.* **2006**, *128*, 11318–11319.

[240] De Meyer, T.; Ensing, B.; Rogge, S. M.; De Clerck, K.; Meijer, E. J.; Van Speybroeck, V. Acidity Constant (pKa) Calculation of Large Solvated Dye Molecules: Evaluation of Two Advanced Molecular Dynamics Methods. *ChemPhysChem* **2016**, *17*, 3447–3459.

[241] Ensing, B.; Tiwari, A.; Tros, M.; Hunger, J.; Domingos, S. R.; Pérez, C.; Smits, G.; Bonn, M.; Bonn, D.; Woutersen, S. On the origin of the extremely different solubilities of polyethers in water. *Nat. Commun.* **2019**, *10*, 2893.

[242] Laage, D.; Hynes, J. T. On the molecular mechanism of water reorientation. *J. Phys. Chem. B* **2008**, *112*, 14230–14242.

Appendix

Dielectric properties of electrolyte solutions

Complex dielectric spectra were measured for a series of metal-alkali chloride (MCl with M = Na^+, K^+, Rb^+ and Cs^+) solutions both in H_2O and D_2O. For the study of protons (H^+) and hydroxide (OH^-) ion, we recorded complex dielectric spectra for the following solutions: HCl and NaOH dissolved in H_2O and DCl and NaOD dissolved in D_2O. Calibration of the setup was made prior measurements using air (open circuit), deionized water (5.5 μS/m) at 23°C and silver paint (short circuit). The dielectric properties of pure H_2O were extracted from previously reported values by Buchner and co-workers.[45]

To systematically study solvation properties, we perform concentration-dependent measurements in steps of 0.1 molal (or 0.1 molar for the study of protons and hydroxide ions), and determine the amplitude of the Debye dipole relaxation, A_{D}. The densities of all the samples were measured to estimate the solute molarity, c, and to account for the reduction of A_{D} due to dilution of the solvent, referred to as $A_{\mathrm{D,n}}$.

As discussed in previous chapters, the dielectric permittivity of aqueous electrolytes is well described using the Cole–Cole relaxation model, with an additional contribution assigned to the translational motion of ions through the solution, i.e. ionic conductivity. The total permittivity is determined by performing a least-square fit of the following equation:

$$\hat{\epsilon}(\nu) = \epsilon_\infty + \frac{\epsilon_{\mathrm{s}} - \epsilon_\infty}{1 + (i2\pi\nu\tau_{\mathrm{D}})^{1-\alpha}} - \frac{i\sigma}{2\pi\nu\epsilon_0},$$

with $A_{\mathrm{D}}(c) = \epsilon_s(c) - \epsilon_\infty$, τ_D the average dipole relaxation time, α accounts for the spectral broadening due to inhomogeneities upon adding ions to the solvent, σ the DC ionic conductivity and ϵ_0 the vacuum permittivity. Based on previous results,[86] the dielectric response of the solvent in the high frequency range, ϵ_∞, is independent of ion concentration. Therefore, to reduce the number of fitting parameters and to achieve better agreement in our values, we fixed ϵ_∞ to the value for pure solvent. However, since experimental values for the dielectric properties of D_2O are largely lacking, we first performed measurements of pure D_2O at 23°C, and determined its dielectric properties using equation (9.7) with $\alpha = 0$ and $\sigma = 0$, leading to $\epsilon_\infty = 5.803$, $A_{\mathrm{D}}(0) = 72.783$ and $\tau_{\mathrm{D}}(0) = 11.07$ ps.

Apart from the dilution of the solvent, dissolved ions also exert a strong influence on the orientational motion of the surrounding water molecules, an effect conventionally referred as depolarization. To unambiguously account for this effect, we defined $\Delta A_{\mathrm{D}}(c) = A_{\mathrm{D,n}}(c) - A_{\mathrm{D}}(c)$. Tables A.1–A.12 summarize all the experimental values extracted for dielectric properties of the studied solutions.

Table A.1. Molality, m [mol/kg], density, ρ, ionic concentration, c [mol/dm^3], reduced dielectric response due to dilution of the solvent, $A_{\mathrm{D,n}}$, depolarization, ΔA_{D}, dielectric relaxation parameters τ_{D}, α and specific conductivity, σ, of NaCl in H_2O at 23°C.

m	ρ [g/dm^3]	c	$A_{\mathrm{D,n}}$	ΔA_{D}	τ_{D} [ps]	α	σ [S/m]
0.1	1000.65	0.0996	73.043	1.452(33)	8.598	0.0006	1.025(4)
0.2	1004.75	0.1993	72.916	2.706(15)	8.538	0.0031	1.938(7)
0.3	1008.77	0.2984	72.786	3.870(20)	8.455	0.0050	2.806(9)
0.4	1012.70	0.3973	72.650	4.901(23)	8.398	0.0075	3.623(8)
0.5	1016.67	0.4954	72.521	5.904(20)	8.342	0.0098	4.410(5)
0.6	1020.57	0.5933	72.387	6.827(7)	8.299	0.0121	5.175(6)
0.7	1024.50	0.6913	72.255	7.761(33)	8.240	0.0142	5.914(5)
0.8	1028.40	0.7886	72.124	8.684(18)	8.190	0.0164	6.639(10)
0.9	1032.25	0.8854	71.991	9.565(17)	8.137	0.0186	7.338(6)
1.0	1036.00	0.9819	71.853	10.396(52)	8.099	0.0212	8.003(28)

Table A.2. Molality, m [mol/kg], density, ρ, ionic concentration, c [mol/dm^3], reduced dielectric response due to dilution of the solvent, $A_{\mathrm{D,n}}$, depolarization, ΔA_{D}, dielectric relaxation parameters τ_{D}, α and specific conductivity, σ, of NaCl in D_2O at 23°C.

m	ρ [g/dm^3]	c	$A_{\mathrm{D,n}}$	ΔA_{D}	τ_{D} [ps]	α	σ [S/m]
0.1	1108.00	0.0997	72.756	1.491(17)	10.931	0.0019	0.845(3)
0.2	1111.92	0.1992	72.631	2.749(32)	10.830	0.0006	1.592(6)
0.3	1115.93	0.2984	72.513	3.909(9)	10.732	0.0033	2.314(7)
0.4	1119.82	0.3971	72.389	4.969(13)	10.651	0.0055	2.991(6)
0.5	1123.63	0.4956	72.260	5.984(5)	10.575	0.0080	3.650(9)
0.6	1127.35	0.5935	72.129	6.933(12)	10.500	0.0103	4.273(9)
0.7	1131.10	0.6913	71.999	7.870(18)	10.432	0.0127	4.878(3)
0.8	1134.95	0.7886	71.877	8.813(31)	10.336	0.0148	5.491(17)
0.9	1138.57	0.8860	71.741	9.699(26)	10.258	0.0169	6.073(17)
1.0	1142.20	0.9825	71.608	10.545(26)	10.191	0.0190	6.631(16)

Table A.3. Molality, m [mol/kg], density, ρ, ionic concentration, c [mol/dm^3], reduced dielectric response due to dilution of the solvent, $A_{\mathrm{D,n}}$, depolarization, ΔA_{D}, dielectric relaxation parameters τ_{D}, α and specific conductivity, σ, of KCl in H_2O at 23°C.

m	ρ [g/dm^3]	c	$A_{\mathrm{D,n}}$	ΔA_{D}	τ_{D} [ps]	α	σ [S/m]
0.1	1001.00	0.0997	72.950	1.107(10)	8.581	0.0020	1.178(13)
0.2	1005.50	0.1988	72.738	1.961(3)	8.527	0.0046	2.251(9)
0.3	1009.95	0.2973	72.525	2.707(14)	8.446	0.0073	3.305(12)
0.4	1014.40	0.3953	72.316	3.365(14)	8.404	0.0087	4.310(11)
0.5	1018.88	0.4927	72.111	4.028(13)	8.317	0.0125	5.326(14)
0.6	1023.35	0.5896	71.909	4.683(22)	8.260	0.0155	6.333(21)
0.7	1027.70	0.6859	71.702	5.297(16)	8.215	0.0166	7.297(15)
0.8	1032.05	0.7817	71.497	5.899(14)	8.157	0.0186	8.268(15)
0.9	1036.40	0.8769	71.295	6.475(17)	8.091	0.0212	9.219(7)

Table A.4. Molality, m [mol/kg], density, ρ, ionic concentration, c [mol/dm^3], reduced dielectric response due to dilution of the solvent, $A_{\mathrm{D,n}}$, depolarization, ΔA_{D}, dielectric relaxation parameters τ_{D}, α and specific conductivity, σ, of KCl in D_2O at 23°C.

m	ρ [g/dm^3]	c	$A_{\mathrm{D,n}}$	ΔA_{D}	τ_{D} [ps]	α	σ [S/m]
0.1	1108.30	0.0997	72.563	1.130(9)	10.922	0.0008	0.974(11)
0.2	1112.60	0.1988	72.359	1.996(14)	10.813	0.0015	1.889(14)
0.3	1116.80	0.2974	72.152	2.765(16)	10.716	0.0045	2.752(23)
0.4	1121.00	0.3954	71.947	3.442(29)	10.629	0.0070	3.612(17)
0.5	1125.20	0.4929	71.745	4.135(11)	10.539	0.0098	4.439(24)
0.6	1129.50	0.5899	71.552	4.807(13)	10.447	0.0118	5.292(26)
0.7	1133.52	0.6862	71.343	5.425(17)	10.363	0.0144	6.094(33)
0.8	1137.62	0.7820	71.143	6.044(9)	10.269	0.0163	6.900(36)
0.9	1141.60	0.8772	70.937	6.646(25)	10.195	0.0191	7.704(47)

Table A.5. Molality, m [mol/kg], density, ρ, ionic concentration, c [mol/dm^3], reduced dielectric response due to dilution of the solvent, $A_{\mathrm{D,n}}$, depolarization, ΔA_{D}, dielectric relaxation parameters τ_{D}, α and specific conductivity, σ, of RbCl in H_2O at 23°C.

m	ρ [g/dm^3]	c	$A_{\mathrm{D,n}}$	ΔA_{D}	τ_{D} [ps]	α	σ [S/m]
0.1	1005.00	0.0996	72.905	1.026(18)	8.583	0.0015	1.207(6)
0.2	1013.36	0.1985	72.641	1.722(19)	8.510	0.0038	2.304(7)
0.3	1021.70	0.2968	72.381	2.324(16)	8.444	0.0060	3.361(11)
0.4	1029.98	0.3943	72.123	2.878(24)	8.384	0.0083	4.391(8)
0.5	1038.38	0.4912	71.879	3.396(20)	8.330	0.0104	5.412(12)
0.6	1047.03	0.5876	71.658	3.947(19)	8.275	0.0129	6.448(16)
0.7	1055.28	0.6832	71.416	4.392(34)	8.218	0.0148	7.453(7)
0.8	1063.50	0.7782	71.176	4.913(21)	8.163	0.0170	8.422(14)
0.9	1071.70	0.8725	70.940	5.380(25)	8.113	0.0189	9.391(17)

Table A.6. Molality, m [mol/kg], density, ρ, ionic concentration, c [mol/dm^3], reduced dielectric response due to dilution of the solvent, $A_{\mathrm{D,n}}$, depolarization, ΔA_{D}, dielectric relaxation parameters τ_{D}, α and specific conductivity, σ, of RbCl in D_2O at 23°C.

m	ρ [g/dm^3]	c	$A_{\mathrm{D,n}}$	ΔA_{D}	τ_{D} [ps]	α	σ [S/m]
0.1	1112.13	0.0996	72.610	1.045(13)	10.946	0.0005	0.993(4)
0.2	1120.27	0.1986	72.359	1.747(19)	10.840	0.0023	1.910(2)
0.3	1128.40	0.2968	72.111	2.373(16)	10.748	0.0049	2.788(4)
0.4	1136.40	0.3944	71.860	2.932(16)	10.664	0.0075	3.639(6)
0.5	1144.47	0.4914	71.619	3.462(16)	10.581	0.0100	4.487(9)
0.6	1152.63	0.5877	71.388	4.048(7)	10.490	0.0121	5.389(30)
0.7	1160.65	0.6834	71.154	4.511(7)	10.395	0.0137	6.169(6)
0.8	1168.68	0.7785	70.924	5.050(14)	10.313	0.0157	6.995(9)
0.9	1176.60	0.8730	70.694	5.533(14)	10.213	0.0172	7.815(4)

Table A.7. Molality, m [mol/kg], density, ρ, ionic concentration, c [mol/dm^3], reduced dielectric response due to dilution of the solvent, $A_{\mathrm{D,n}}$, depolarization, ΔA_{D}, dielectric relaxation parameters τ_{D}, α and specific conductivity, σ, of CsCl in H_2O at 23°C.

m	ρ [g/dm^3]	c	$A_{\mathrm{D,n}}$	ΔA_{D}	τ_{D} [ps]	α	σ [S/m]
0.1	1009.40	0.0996	72.881	0.975(21)	8.602	0.0016	1.241(7)
0.2	1022.00	0.1982	72.587	1.594(23)	8.534	0.0036	2.367(4)
0.3	1034.60	0.2967	72.295	2.104(32)	8.473	0.0059	3.448(5)
0.4	1047.00	0.3934	72.011	2.533(24)	8.428	0.0082	4.478(12)
0.5	1059.33	0.4902	71.719	2.912(40)	8.363	0.0102	5.490(20)
0.6	1071.55	0.5859	71.433	3.333(39)	8.338	0.0123	6.484(20)
0.7	1083.65	0.6806	71.151	3.720(39)	8.292	0.0140	7.460(8)
0.8	1095.75	0.7749	70.874	4.161(16)	8.246	0.0154	8.419(3)
0.9	1107.55	0.8685	70.583	4.498(47)	8.194	0.0169	9.369(4)
1.0	1119.15	0.9607	70.295	4.882(29)	8.152	0.0180	10.284(10)

Table A.8. Molality, m [mol/kg], density, ρ, ionic concentration, c [mol/dm^3], reduced dielectric response due to dilution of the solvent, $A_{\mathrm{D,n}}$, depolarization, ΔA_{D}, dielectric relaxation parameters τ_{D}, α and specific conductivity, σ, of CsCl in D_2O at 23°C.

m	ρ [g/dm^3]	c	$A_{\mathrm{D,n}}$	ΔA_{D}	τ_{D} [ps]	α	σ [S/m]
0.1	1116.55	0.0996	72.618	1.009(11)	10.946	0.0013	1.030(2)
0.2	1128.80	0.1985	72.327	1.623(28)	10.848	0.0018	1.962(2)
0.3	1140.95	0.2967	72.038	2.119(17)	10.762	0.0045	2.856(1)
0.4	1153.10	0.3937	71.762	2.577(16)	10.695	0.0070	3.719(3)
0.5	1164.90	0.4903	71.468	2.982(10)	10.612	0.0090	4.554(7)
0.6	1176.90	0.5859	71.197	3.427(16)	10.548	0.0113	5.391(3)
0.7	1188.75	0.6809	70.923	3.827(19)	10.469	0.0127	6.213(13)
0.8	1200.25	0.7752	70.635	4.253(36)	10.369	0.0137	7.016(9)
0.9	1211.70	0.8686	70.352	4.647(30)	10.292	0.0150	7.802(9)
1.0	1222.92	0.9609	70.067	5.033(46)	10.232	0.0167	8.576(24)

Table A.9. Ionic concentration, c [mol/dm^3], density, ρ, reduced dielectric response due to dilution of the solvent, $A_{\mathrm{D,n}}$, depolarization, ΔA_{D}, dielectric relaxation parameters τ_{D}, α and specific conductivity, σ, of HCl in H_2O at 23°C.

c	ρ [g/dm^3]	$A_{\mathrm{D,n}}$	ΔA_{D}	τ_{D} [ps]	α	σ [S/m]
0.1	998.9	73.074	2.918(75)	8.66	0.0028	3.824(8)
0.2	1000.7	72.94	5.549(83)	8.622	0.0041	7.455(19)
0.3	1002.5	72.807	8.118(91)	8.583	0.0048	10.963(40)
0.4	1004.4	72.682	10.600(90)	8.53	0.005	14.353(52)
0.5	1006.2	72.551	12.975(90)	8.484	0.0053	17.659(60)
0.6	1008.1	72.428	15.302(84)	8.444	0.0061	20.954(41)
0.7	1009.8	72.291	17.370(82)	8.413	0.0075	24.019(44)
0.8	1011.6	72.163	19.351(73)	8.388	0.0089	26.995(53)
0.9	1013.4	72.035	21.216(82)	8.372	0.0108	29.883(54)
1.0	1015.2	71.909	22.951(78)	8.374	0.0137	32.672(50)

Table A.10. Ionic concentration, c [mol/dm^3], density, ρ, reduced dielectric response due to dilution of the solvent, $A_{\mathrm{D,n}}$, depolarization, ΔA_{D}, dielectric relaxation parameters τ_{D}, α and specific conductivity, σ, of DCl in D_2O at 23°C.

c	ρ [g/dm^3]	$A_{\mathrm{D,n}}$	ΔA_{D}	τ_{D} [ps]	α	σ [S/m]
0.1	1106.1	72.771	2.546(44)	11.032	0.0005	2.667(12)
0.2	1107.8	72.637	4.889(54)	10.981	0.0026	5.174(12)
0.3	1109.5	72.504	7.223(58)	10.909	0.0036	7.615(13)
0.4	1111.2	72.372	9.506(51)	10.832	0.0042	9.998(9)
0.5	1112.9	72.241	11.715(30)	10.749	0.0046	12.310(24)
0.6	1114.6	72.111	13.905(58)	10.666	0.0053	14.618(32)
0.7	1116.3	71.982	15.872(69)	10.591	0.0059	16.783(21)
0.8	1117.9	71.847	17.752(63)	10.522	0.0071	18.893(23)
0.9	1119.6	71.719	19.570(58)	10.456	0.0082	20.949(11)
1.0	1121.2	71.586	21.292(54)	10.39	0.0097	22.958(16)

Table A.11. Ionic concentration, c [mol/dm^3], density, ρ, reduced dielectric response due to dilution of the solvent, $A_{\mathrm{D,n}}$, depolarization, ΔA_{D}, dielectric relaxation parameters τ_{D}, α and specific conductivity, σ, of NaOH in H_2O at 23°C.

c	ρ [g/dm^3]	$A_{\mathrm{D,n}}$	ΔA_{D}	τ_{D} [ps]	α	σ [S/m]
0.1	1001.4	73.231	1.950(8)	8.674	0.0020	2.124(23)
0.2	1005.9	73.264	3.638(45)	8.647	0.0042	4.075(7)
0.3	1010.2	73.289	5.271(38)	8.633	0.0059	5.922(22)
0.4	1014.5	73.311	6.843(14)	8.619	0.0072	7.690(9)
0.5	1018.8	73.332	8.385(18)	8.599	0.0084	9.402(11)
0.6	1023.0	73.346	9.904(16)	8.582	0.0095	11.062(12)
0.7	1027.2	73.359	11.368(32)	8.567	0.0106	12.649(30)
0.8	1031.3	73.366	12.755(28)	8.556	0.0119	14.146(21)
0.9	1035.4	73.372	14.109(9)	8.546	0.0133	15.623(15)
1.0	1039.5	73.379	15.431(49)	8.540	0.0149	17.014(44)

Table A.12. Ionic concentration, c [mol/dm^3], density, ρ, reduced dielectric response due to dilution of the solvent, $A_{\mathrm{D,n}}$, depolarization, ΔA_{D}, dielectric relaxation parameters τ_{D}, α and specific conductivity, σ, of NaOD in D_2O at 23°C.

c	ρ [g/dm^3]	$A_{\mathrm{D,n}}$	ΔA_{D}	τ_{D} [ps]	α	σ [S/m]
0.1	1109.2	72.952	1.951(37)	11.053	0.0018	1.368(11)
0.2	1114.0	72.997	3.487(17)	11.023	0.0013	2.614(22)
0.3	1118.85	73.046	4.990(28)	11.004	0.0024	3.785(15)
0.4	1123.6	73.088	6.392(22)	10.98	0.0045	4.907(27)
0.5	1128.2	73.119	7.766(26)	10.966	0.0059	5.962(23)
0.6	1132.85	73.154	9.107(15)	10.941	0.0076	6.995(23)
0.7	1137.45	73.185	10.374(41)	10.914	0.0092	7.990(32)
0.8	1141.95	73.21	11.574(73)	10.9	0.0106	8.897(61)
0.9	1146.4	73.231	12.837(34)	10.888	0.0121	9.843(26)
1.0	1150.8	73.249	14.041(65)	10.874	0.0135	10.727(45)

Summary

Unraveling the elusive solvation structure of aqueous ions using advanced spectroscopic techniques

In this thesis, we investigate the solvation of ions in water using state-of-the-art spectroscopic techniques: GHz dielectric relaxation spectroscopy (DRS) and femtosecond time-resolved vibrational spectroscopy (TRVS), which are introduced in **Chapters 2** and **3**. In **Chapters 4**, **5**, and **6**, we demonstrate how DRS can be used to investigate solvation properties and the structure of water around ions. In **Chapters 7**, **8** and **9**, we apply TRVS to observe how the negatively charged oxygen atom of hydroxide and phenolate ions, which act as strong hydrogen-bond acceptors, affects the structural dynamics of the hydrogen-bond network of water.

In the experiments presented in **Chapter 4**, we study the extent to which the cooperative dynamics of water are affected by the presence of ions. Isotope-dependent measurements enable us to observe the dielectric response of water molecules surrounding ions. Our results indicate that these water molecules reorient in a much less cooperative manner than bulk water, as a consequence of the local disruption of the hydrogen-bond network by the ions. Our observations allow us to test for the first time and to empirically modify the Hubbard-Onsager model that quantifies the ion-induced dielectric deficiency of water. In contrast to the original model, the modified Hubbard-Onsager equation takes the disruption of the hydrogen-bond network by the ions into account, making it possible to determine hydration numbers in an unambiguous manner. These numbers are of paramount importance since they characterize the chemical and physical properties of aqueous solutions.

In **Chapter 5**, the isotope effect is again used to determine hydration numbers of alkali-metal ions. Based on our observations, Na^+ forms solvation shells of $\sim$7 water molecules, a hydration number slightly larger than the packing capacity of water in the first solvation shell. Upon increasing the size of the ion, the hydration number reduces to 4, 3 and 3 for K^+, Rb^+ and Cs^+, respectively. In these three cases, the hydration number is smaller than the packing capacity, meaning that the first solvation shell is weakly hydrated. Our results are in line with the Hofmeister series which establishes the relative hydration ability of water depending on electrostatic ion–water interactions.

Protons (H^+) and hydroxide ions (OH^-) are cases of special interest since they have the ability to form hydration complexes in which the excess charge is delocalized. In **Chapter 6**, we measure the isotope-dependent dielectric response to study the solvation of H^+ and OH^- ions. From its hydration number, H^+ is found

to mostly exist in water as an Eigen $H_9O_4^+$ complex. From the study of the kinetic effects, we estimate the number of water molecules that are involved in the H^+ and OH^- charge diffusion. This number is at least three times higher for H^+ than for OH^-, meaning that the proton transfer mechanism is significantly different in acidic and alkaline solutions.

In **Chapter 7**, we explore the extent to which OH^- ions affect the reorientation dynamics of water molecules. We examine whether OH^- can have an influence on the molecular dynamics of the solvent (water molecules beyond the first solvation shell). For solutions with OH^- concentration up to 4 molar, the reorientation dynamics of water are slightly slowed down. At higher OH^- concentrations, the remaining bulk-like solvent is cooperatively locked between neighboring OH^- ions due to a crowding effect. In this regime, the solution can be regarded as a semi-rigid hydrogen-bond network.

In **Chapter 8**, we continue our study of the structural properties of OH^- ions, but with a focus on the role that they could play in equilibrating vibrational excess energy of surrounding water molecules. We observe that hydroxide ions accelerate the relaxation of OD-stretch excitations of nearby HDO molecules. This effect is well-described through resonance energy transfer from HDO to OH^- with a Förster radius of 3 Å, a value that matches the intermolecular distance in liquid water. Hence, OH^- ions act as a sink for excess vibrational energy of neighbouring excited water molecules. Our results suggest that OH^- ions may also participate in equilibrating excess energy in chemical reactions in alkaline environments.

Finally, in **Chapter 9**, we study how phenolate ions affect the reorientation dynamics of surrounding water molecules. Our results show that phenolate slows down the dynamics of the surrounding water molecules, an effect that extends even beyond the first solvation shell. This effect is due to the propensity of the negatively charged oxygen to form strong hydrogen bonds, which "lock" the hydrogen-bond structure.

The results presented in this thesis provide new information on the solvation properties of several commonly occupied ions. We hope that this thesis will inspire further experimental and theoretical studies, and may help to improve our understanding of the solvation structure and dynamics of ions in water.

Samenvatting

Het ontrafelen van de raadselachtige structuur van water rondom ionen met behulp van geavanceerde spectroscopische technieken

In dit proefschrift onderzoeken we hoe ionen oplossen in water, waarbij we gebruik maken van *state-of-the-art* spectroscopische technieken: gigahertz diëlektrische relaxatiespectroscopie (DRS) en femtoseconde tijdsopgeloste vibrationele spectroscopie (TRVS). Deze technieken worden geïntroduceerd in **Hoofdstukken 2** en **3**. In **Hoofdstukken 4**, **5** en **6** laten we zien hoe DRS kan worden gebruikt om de eigenschappen van water rond ionen te onderzoeken. In **Hoofdstukken 7**, **8** en **9** passen we TRVS toe om de invloed van het negatief geladen zuurstofatoom in hydroxide- en fenolaat-ionen—beide sterke waterstofbrug-acceptoren—op de structuur en dynamica van het waterstofbrug-netwerk van water te bekijken.

In **Hoofdstuk 4** onderzoeken we de mate waarin de coöperatieve dynamica van water wordt beïnvloed door de aanwezigheid van ionen. Door isotoop-afhankelijke metingen uit te voeren kunnen we de diëlektrische respons van watermoleculen rondom ionen waarnemen. Uit onze resultaten blijkt dat deze watermoleculen op een veel minder coöperatieve manier reoriënteren dan bulkwater, als gevolg van de lokale verstoring van het waterstofbrug-netwerk door de ionen. Onze waarnemingen stellen ons in staat om het Hubbard-Onsager model voor het eerst experimenteel te testen. Dit model beschrijft de door ionen veroorzaakte vermindering van de diëlektrische respons van water. Uit de experimenten blijkt dat het Hubbard-Onsager model moet worden aangepast om een goede beschrijving te geven van water rondom ionen. In tegenstelling tot het oorspronkelijke model, houdt de aangepaste Hubbard-Onsager-vergelijking rekening met de verstoring van het waterstofbrug-netwerk door ionen. Hierdoor wordt het mogelijk om op een ondubbelzinnige manier het aantal hydraterende watermoleculen (kortweg, het "hydratiegetal") te bepalen. Dit aantal is van groot belang omdat het de chemische en fysische eigenschappen van waterige oplossingen karakteriseert.

In **Hoofdstuk 5** wordt het isotoop-effect opnieuw gebruikt om het hydratatiegetal van alkalimetaal-ionen te bepalen. Op basis van onze waarnemingen vormt Na^+ solvatatieschillen van $\sim$7 watermoleculen, een aantal dat iets groter is dan de pakkingscapaciteit van water in de eerste solvatatieschil. Met toenemende ionstraal vermindert het aantal hydraterende watermoleculen tot respectievelijk 4, 3 en 3 voor K^+, Rb^+ en Cs^+. In deze drie gevallen is het hydratatiegetal kleiner dan de pakkingscapaciteit, wat betekent dat de eerste solvatatieschil zwak gehydrateerd is. Onze resultaten komen overeen met de Hofmeister-reeks die de sterkte

van de interactie tussen ionen en water voor verschillende ionen weergeeft.

Protonen (H^+) en hydroxide-ionen (OH^-) zijn bijzondere ionen, omdat ze het vermogen hebben om hydratatiecomplexen te vormen waarin de lading wordt gedelokaliseerd. In **Hoofdstuk 6** meten we de isotoopafhankelijke diëlektrische respons om de solvatatie van H^+ en OH^- ionen te bestuderen. Uit het hydratatiegetal blijkt dat H^+ meestal als een Eigen ($H_9O_4^+$) complex voorkomt in water. Door de diëlektrische respons in gewoon en zwaar water te vergelijken, kunnen we een schatting maken van het aantal watermoleculen dat betrokken is bij de ladingsdiffusie van H^+ en OH^-. Dit aantal is minstens drie keer hoger voor H^+ dan voor OH^-, wat betekent dat het transportmechanisme van protonen en hydroxide ionen aanzienlijk verschilt. Dit is verrassend omdat ook vaak is voorgesteld dat de transportmechanismes van deze twee ionen elkaars spiegelbeeld zouden zijn.

In **Hoofdstuk 7** onderzoeken we de mate waarin OH^- ionen de reoriëntatie van watermoleculen beïnvloeden. We onderzoeken of OH^- invloed heeft op de moleculaire dynamica van de watermoleculen buiten de eerste solvatatieschil. Voor oplossingen met een OH^- concentratie tot 4 molair wordt de reoriëntatiedynamica van water buiten de eerste solvatatieschil enigszins vertraagd, maar het effect is gering. Als de OH^- concentratie verder wordt verhoogd neemt dit effect aanzienlijk toe, het resterende water zit dan als het ware klem tussen de solvatatieschillen van naburige OH^--ionen. In dit regime kan de oplossing worden beschouwd als een semi-rigide waterstofbrug-netwerk.

In **Hoofdstuk 8** bestuderen we de rol die OH^- ionen spelen bij het in evenwicht brengen van de overtollige vibrationele energie van omringende watermoleculen. We zien dat hydroxide-ionen de energierelaxatie van OD-strek excitaties van nabijgelegen HDO-moleculen versnellen. Dit effect wordt goed beschreven door resonante energieoverdracht van HDO naar de solvatatieschil van OH^-. Deze resonante energieoverdracht wordt gekarakteriseerd door een zogenaamde Försterradius van 3 Å, een lengte die overeenkomt met de intermoleculaire afstand in vloeibaar water. Dit duidt er op dat de solvatatieschillen van OH^- ionen kunnen fungeren als een afvoer voor overtollige vibrationele energie van aangrenzende geëxciteerde watermoleculen.

Ten slotte bestuderen we in **Hoofdstuk 9** hoe fenolaat-ionen de reoriëntatiedynamica van omringende watermoleculen beïnvloeden. Onze resultaten tonen aan dat fenolaat de dynamica van de omringende watermoleculen vertraagt, een effect dat zich zelfs tot voorbij de eerste solvatatieschil uitstrekt. Dit effect is een gevolg van de sterke waterstofbindingen die het negatief geladen zuurstof-atoom van fenolaat kan vormen, en waardoor de waterstofbrugstructuur als het ware "vergrendeld" wordt.

De resultaten in dit proefschrift geven nieuwe informatie over de solvatatie-eigenschappen van verschillende veel voorkomende ionen. We hopen dat dit proefschrift tot verdere experimentele en theoretische studies zal leiden, en ons begrip van de solvatatie-structuur en dynamica van ionen in water kan verbeteren.

Resumen

Entendiendo la misteriosa estructura molecular que rodea a los iones disueltos en agua mediante técnicas espectroscópicas de vanguardia.

A lo largo de esta tesis se presenta un estudio sobre la solvatación de iones con agua, usando para ello tecnologías espectroscópicas de vanguardia como la espectroscopía de relajación dieléctrica (ERD) con frecuencias en el orden de gigahercios (súper altas frecuencias) y la espectroscopía vibracional con una resolución temporal de femtosegundos (EVFS). Dichas técnicas son explicadas en los **Capítulos 2** y **3**. Por otra parte, en los **Capítulos 4**, **5** y **6** se muestra la forma de implementar la ERD para el estudio de las propiedades de solvatación y el estudio de las estructuras moleculares del agua que rodea a los iones. Mientras que, en los **Capítulos 7**, **8** y **9**, se usa EVFS para observar cómo el átomo de oxígeno que está contenido en los iones de hidróxido y fenolato, y que actúa como un aceptor de enlaces de hidrógeno, afecta las propiedades dinámicas de la red de enlaces de hidrógeno que forma el agua a nivel molecular.

Con la serie de experimentos presentados en el **Capítulo 4** se estudia la medida en que la dinámica cooperativa de las moléculas de agua cambia ante la presencia de iones. Con base a un análisis de dos isótopos de agua, estudiamos de forma puramente experimental las propiedades dieléctricas de las moléculas de agua en las proximidades de los iones. En ésta región, las moléculas de agua pierden su carácter cooperativo debido a la ruptura local de la red de enlaces de hidrógeno. Adicionalmente, nuestros experimentos permitieron probar por primera vez la validez del modelo de Hubbard y Onsager, que predice la medida en que los iones, debido a su campo eléctrico, obstaculizan la movilidad de las moléculas de agua. Nuestros experimentos dan lugar a modificaciones del modelo de Hubbard y Onsager, de tal forma que el efecto de la ruptura de la red de enlaces de hidrógeno se puede tomar en cuenta, un efecto que es despreciado en el modelo original. Nuestro nuevo modelo permite determinar el número de hidratación de iones en agua de una forma físicamente más completa. Estos números son de primordial importancia porque describen las propiedades químicas y físicas de soluciones acuosas.

Usando el mismo análisis del capítulo anterior, en el **Capítulo 5** se presenta un estudio para determinar los números de hidratación de la familia de iones alcalinos. En este análisis se observa que aproximadamente 7 moléculas de agua forman un caparazón o estructura de solvatación alrededor de los iones de Na^+: este número está por encima de la capacidad espacial de la primera capa de solvatación. Sin embargo, al incrementar el tamaño del los iones, los números de hidratación

disminuyen a 4, 3 y 3 para K^+, Rb^+ y Cs^+. En estos últimos casos, los números de hidratación son menores que la capacidad de la primera capa de solvatación; lo cual indica que el efecto de hidratación es débil incluso en la vecindad inmediata de los iones. Estos resultados son coherentes con la serie de Hofmeister, donde se entiende el efecto de hidratación como el resultado de las interacciones electroestáticas entre los iones y las moléculas de agua.

Los protones (H^+) y los iones de hidróxido (OH^-) son casos de particular interés por su habilidad de formar estructuras de hidratación donde la carga iónica está delocalizada. En el **Capítulo 6** se presenta un estudio de las propiedades de solvatación de estos iones con la misma técnica de los dos capítulos anteriores. El número de hidratación de los protones (H^+) revela que éstos existen primordialmente en agua como estructuras "Eigen'', esto es $H_9O_4^+$. Por otra parte, a partir del estudio de los efectos cinéticos se puede estimar el número de moléculas de agua que participan en el proceso de difusión de la carga iónica. Este último número es al menos tres veces mayor para protones que para iones de hidróxido, lo que significa que el proceso de transferencia de protones es significativamente diferente en soluciones ácidas que en soluciones alcalinas.

En el **Capítulo 7** se presenta un estudio sobre la medida en que los iones de hidróxido afectan la dinámica de reorientación de las moléculas de agua. En particular, examinamos si los iones de hidróxido afectan la dinámica del solvente (moléculas más allá de su primera capa de solvatación). En concentraciones de hasta 4 molares, la dinámica de reorientación molecular del agua es ligeramente desacelerada. Sin embargo, a concentraciones más altas, la dinámica de las moléculas restantes fuera de cualquier caparazón de hidratación se frena de manera cooperativa, atrapadas entre el efecto de múltiples iones de hidróxido. Este fenómeno es debido al efecto de la acumulación de iones. En este último régimen, se puede entender al sistema como una red semirrígida de enlaces de hidrógeno.

En el **Capítulo 8** continuamos con el estudio de las propiedades estructurales de los iones de hidróxido, pero ahora prestando particular atención al rol que podrían tener en el equilibrio del exceso de energía vibracional existente en moléculas circundantes. Nuestros resultados indican que los iones de hidróxido aceleran el proceso de relajación vibracional de los enlaces de OD de las moléculas de HDO cercanas. Además, nuestras observaciones son descritas mediante un proceso de transferencia de energía de resonancia desde las moléculas de HDO hacia los iones de hidróxido con un radio de acción (radio de Förster) de 3 Å, una distancia que coincide con el espaciamiento intermolecular en agua. Así pues, los iones de hidróxido actúan como un pozo para el exceso de energía vibracional contenida en moléculas excitadas circundantes. Estos resultados sugieren que los iones de hidróxido pueden también participar en el equilibrio de la energía excedente que pueda surgir de reacciones químicas en ambientes alcalinos.

Por último, los experimentos presentados en el **Capítulo 9** muestran cómo los iones de fenolato afectan la dinámica de reorientación de las moléculas de agua

en su vecindad. Nuestros resultados también demuestran que la dinámica de las moléculas circundantes es significativamente desacelerada, y que este efecto se extiende más allá de su primera capa de solvatación. Este fenómeno se explica debido a que el átomo de oxígeno del ion de fenolato, negativamente cargado, es susceptible a formar fuertes enlaces de hidrógeno, que a su vez "inmovilizan" la estructura de enlaces de hidrógeno del agua.

Los resultados presentados en esta tesis proveen nueva información sobre las propiedades de solvatación de múltiples iones que son comúnmente usados. Esperamos que el trabajo presentado en esta tesis sea capaz de inspirar futuros estudios, tanto experimentales como teóricos, y que logren mejorar la forma en que entendemos las estructuras de solvatación y las propiedades de los iones disueltos en agua.

Заключение

Изучение неуловимых структур гидратированных ионов с использованием современных спектроскопических методов

В представленной работе проведено исследование сольватации ионов в водных растворах с использованием современных спектроскопических методов: спектроскопии диэлектрической релаксации (СДР) в ГГц диапазоне и фемтосекундной времяразрешённой колебательной спектроскопии (ВРКС), которые описаны в **Главах 2** и **3**. В **Главах 4**, **5** и **6** продемонстрировано, как сольватационные свойства и структура воды вблизи ионов могут быть изучены при помощи СДР. В **Главах 7**, **8** и **9** при помощи ВРКС показано, как отрицательно заряженные атомы кислорода гидроксид и фенолят ионов, являющиеся сильными акцепторами водородной связи, влияют на структурную динамику системы водородных связей в воде.

В экспериментах, представленных в **Главе 4** изучено, до какой степени коллективная динамика молекул воды подвержена влиянию ионов. Измерения с использованием различных изотопов позволили пронаблюдать диэлектрический отклик молекул воды, входящих в сольватную оболочку ионов. Полученный результат свидетельствует о том, что реориентация молекул воды, входящих в сольватную оболочку ионов, происходит под значительно меньшим влиянием кооперативных эффектов, чем в объеме воды, вследствие локальных разрывов в системе водородных связей под влиянием ионов. Наши наблюдения позволили впервые протестировать и модифицировать на основании экспериментов модель Хаббарда-Онзагера, описывающую диэлектрическую дефицитность воды, индуцированную ионами. В противоположность оригинальной модели, модифицированное уравнение Хаббарда-Онзагера учитывает ослабление водородных связей и позволяет таким образом однозначно определить координационные числа ионов. Данные координационные числа имеют огромное значение, так как они определяют химические и физические свойства водных растворов.

В **Главе 5** изотопный эффект снова использовался для определения координацинных чисел щелочных металлов. Исходя из наших наблюдений, катион Na^+ имеет сольватную оболочку, состоящую из $\sim$7 молекул воды, что несколько больше, чем количество воды, способное уместиться в первую сольватную оболочку. При увеличении размера иона координационное число уменьшается до 4, 3 и 3 для K^+, Rb^+ и Cs^+ соответственно. В трёх последних случаях координационное число меньше, чем емкость первой сольватной обо-

лочки, это значит, что ион слабо гидратирован. Наши результаты согласуются с лиотропным рядом Хоффмайстера, который описывает способность молекул воды гидратировать ионы, в зависимости от силы взаимодействий вода-ион.

Особый интерес представляют протоны (H^+) и гидроксид-ионы (OH^-) в силу того, что они могут образовывать гидраты, в которых избыточный заряд делокализован. В **Главе 6** для изучения сольватационных свойств ионов H^+ и OH^- был измерен диэлектрический отклик в зависимости от изотопного состава растворов. Исходя из полученного значения координационного числа, гидратированный протон представляет из себя структуру типа катиона Айгена $H_9O_4{}^+$. По результатам изучения кинетических эффектов было оценено количество молекул воды, вовлеченных в диффузию зарядов H^+ и OH^-. Это количество как минимум в три раза выше для H^+, чем для OH^-, что указывает на существенное различие в механизме переноса протона в растворах кислот и щелочей.

В **Главе 7** исследовано, насколько сильно OH^- анионы влияют на вращательную динамику молекул воды. Мы изучили, может ли OH^- влиять на молекулярную динамику растворителя (молекул, не входящих в первую сольватную оболочку). В растворах, с концентрацией OH^- вплоть до 4 М вращательная динамика молекул воды незначительно замедлена. При больших концентрациях оставшиеся "объёмные" молекулы воды заблокированы между соседними OH^- ионами вследствие стеснения ионов. В этом режиме раствор может считаться полужесткой системой водородных связей.

В **Главе 8** продолжено исследование структурных свойств в системах, содержащих OH^- ионы, однако акцент смещен в сторону изучения их роли в процессе достижения равновесия при колебательной релаксации соседних молекул воды. Показано, что гидроксид-ионы ускоряют релаксацию возбужденных OD-стретч колебаний близлежащих молекул HDO. Этот эффект связан с Фёрстеровским резонантным переносом энергии от HDO к OH^- ионам с эффективным радиусом 3 Å, это значение совпадает с межмолекулярным расстоянием в жидкой воде. Следовательно, OH^- ионы выступают в качестве резервуара для избыточной колебательной энергии от соседних молекул. Эти результаты указывают на то, что OH^- ионы могут участвовать в перераспределении энергии при достижении равновесия в процессе химических реакций в щелочной среде.

Наконец, в **Главе 9** изучено влияние фенолят ионов на вращательную динамику молекул воды. Наши результаты демонстрируют, что присутствие фенолят-анионов приводит к замедлению вращательной динамики молекул воды, этот эффект распространяется дальше первой сольватной оболочки. Эффект связан со способностью атома кислорода фенолят-иона образовывать сильные водородные связи с молекулами воды, что "блокирует" систему водородных связей.

Результаты, представленные в данной диссертации содержат новую инфор-

мацию о сольватации часто встречающихся ионов. Мы надеемся, что эта работа стимулирует новые экспериментальные и теоретические исследования и поспособствует лучшему пониманию сольватационных структур и динамики ионов в водных растворах.

Acknowledgements

At this moment, while sitting by the sea with no company but a beer is when I find the calm to recall all the events that led to the end of my PhD. After the effort of evaluating all the experiences that I have passed through, I must confess that I was trapped between laughs and emotions. Although lasers can give you fantastic results (and make you happy and angry at the same time), the incredible people around me were the ones who made this PhD a one of success, a one of joy, and a one full of laughs and uncountable moments that I will treasure forever. Therefore this is undoubtedly the most important section of my dissertation, and I would have happily shared this beer at the beach with any of those who were part of my PhD story.

From all the possible ways to start with these acknowledgments, I will follow the most classic, mentioning how everything started roughly 5 years ago. One day I received an unexpected email from Huib J. Bakker, who very enthusiastically wrote to me (different to the German-like approach that I was used to) and invited me to visit AMOLF for a collaborative project with Sander Woutersen at UvA after finding my CV somewhere. I understood later that they have lasing eyes capable of finding results and potential opportunities where others will only see chaos — that was the case of my CV. My application came with more surprises: the day of the interview turned in a *faena*[†] where they fried my brain for the first time, one of them suggested me to visit *de rosse buurt*, and afterwards their acceptance came almost at midnight on a Sunday. I should have immediately noticed that this PhD wouldn't be monotonous, but full of surprises that would make it memorable. Sander and Huib, I thank both of you for giving me the chance to be part of your teams at UvA and at AMOLF, for giving me a fast-track introduction on Dutch directness, for all the science that I learned from you, and for all the trust and liberty you gave me to explore and improve my abilities in the lab as well as a researcher. I thank all your support and all the many ideas that you threw at me that encouraged me to grow as a researcher and as a professional. It has been a great pleasure and very rewarding collaborating with you.

I was lucky to be part of the group of molecular photonics at UvA that has other experienced researchers and professors who were always keen to help, and thus I would also like to thank them. Thank you Annemieke Petrignani, Fred Brouwer, Hong Zhang, Rene Williams and Wybren Jan Buma for your criticism and all the useful discussions about my research in group meetings, and for all the interesting and enjoyable chats that I had with you in the corridors, during coffee break, cake moments or borrels.

[†]Faena is defined as the passes that a bullfighter makes before giving the last blow to the bull.

I would also like to express my gratitude to Prof. Dr. Richard Buchner (whose work has inspired part of this thesis), Prof. Dr. Ellen Backus, Prof. Dr. Evert Jan Meijer, and Dr. Bernd Ensing (who I had the chance to collaborate with) for having accepted our invitation to be part of the committee in my PhD ceremony, and for taking the time to read this book.

The work presented in this thesis couldn't have been possible without the help, support and positiveness of all our technical staff. No doubt, they are the spine that holds all our Frankenstein-like experiments alive. In particular, I thank Michiel Hilbers (the one who can fix any machine snapping his fingers), Hans Sanders (the best home-made customized baby powder in the Eastern Hemisphere), Wim Roeterdink (laser charmer and borrel organizer), and Hinco Schoenmakers (there is no impossible in his vocabulary, the Dutch David Hasselhoff). Thank you also for being always willing to listen to our problems, frustrations, and give advice (and beers sometimes). I also thank Sven Koot and Tjeerd Weijers, wizards in milling machines and electronics, respectively.

Certainly this thesis only happened because of the moral support from many people, and so, I would like to thank you all. I first want to thank to the three guys that I share the most in my offices: Benjamin, Caro and Eliane. I consider you as my pillars during my PhD who saw the best and the worst of me, and were always keen to give me a hand. Thank you Benjamin, you were always prepared to talk crap as well as serious topics, mainly politic and finance related (in opposition to the hippie style of Steven). I truly enjoyed all the beers that we took to scape our lab frustrations (I don't know why I was frustrated in my first week, I think it was only a nice summer). I have great memories with you: from being the coolest guys with our boat (at least we see ourselves that way) to the fight in the Swiss Alps (I'm still in shock). I would certainly embark on another project or stupid idea with you. Thanks for deproving my English (Dongdong was right). Thank you Caro, you were always prepared to cheer me up, even in my must stubborn moments. Thanks for your kindness and for stopping your own duties to help me multiple times. Thank you also for taking my concerns as yours. Caro, you were the emotions — thanks for crying all the tears that I did not. Eliane, you were the reasoning and the moral compass in the office, and still we shared a quite crazy Google search history. Eliane, it was a great joy sharing the optical setup with you (although your weren't initially convinced, you showed me how to properly pamper Lucy), and a great pleasure collaborating with you. Caro and Eliane, I will remember our debates, our chocolate shelf, our wigs, our kick-off Prosecco for Christmas party, our guacamole breaks, our conference/trip in USA, etc. Thank you for adopting me in the 2.13 kantoortje. My PhD has rewarded me with your friendship, I'm really going to miss working with you three guys.

Furthermore, I wish to thank the people and friends that had an impact in my PhdD work, as well as the people who I shared time during my PhD with. I thank the past and present members of the molecular photonics group: Ariana (Chata,

por todos esos pinches cotorreos de lavadero que nos echamos y seguirán), Chris (eh, puto!), Arthur (for sharing those latino-style tropical moves), Heleen, Tibert (who were not there anymore when I started but gave me advice on PhD handling), Tomislav (King of P***, you are still jealous at my error bars), Dongdong (or best known as Dong Kong in *de rosse buurt*), Elena (I was always scared that you would hit me in the office), Steven (for showing us that playing guitar will not solve any problem but will delay the stress), Ben (because mentioning you twice doesn't cost me anything), René Beker and Sandra (for your incredible kindness and very nice conversations with spicy food), Robbert (for showing us how to build bad-ass setups), Dina (for coming up always with ideas and activities for the group), Mina (for your infinite kindness that makes anyone feel very comfortable), Bruno (for showing us that rainbow love is cool), Olivier, Jarich, Hernán and Max (por estar dispuestos siempre a discutir cualquier basura), Jing, Yadan, Yanson, Yanni, Jiayun, Yu, Angela (fake Chinese) and all the Chinese mafia (for all the incredible food that you showed us), Ivan (you already earned heaven for sharing an office with Max) and Pauli Mazzella (yo sé que quieres chile). In addition, I would also like to thank the so many student that came and went to our group but contributed to the good vibes: Charlotte Mclovin (second best team of the world!), Rafael (come on, my man!), Leo, Federico, Rebecca (súbele al funky brasileiro), Toen, Heleen, Janita, Evelyn, Nico, Maarten, Chris O'Brien (for our Fridays with halve kip), Lory, Jim (wonderful office mate), Daire (my desk, your desk) and Zoe (you know this will be always a free country to join me for a beer).

Apart from the group of molecular photonics, UvA provided a wider spectrum of incredible people who I also wish to thank for collaborations, discussions, coffees and/or beers that we have had together: Ambuj (hope we ever collaborate again), Arjun (love ya, baby!), Alberto, Alan, (saquen las cheves paisas), Verena, Andreea, Yulia, Maria and Nitish. I would specially like to thank Anna and Alina (tía, llévala con tranquilidad) for making the corridors at UvA something more pleasant, I knew if you were around from far away — you both are awesome.

Similar, I would like to mention and thank people from AMOLF. First, thanks to former and present members of the group of ultrafast spectroscopy: Simona, Wilbert, Carien, Konrad (hope we play squash again), Caro, Eliane (you get double mention), Teresa (for helping us with the schedule of the boss and for sharing your spark with everyone at AMOLF), Aleksandr and Alexander (for been always willing to help and for the incredible and unnecessary vodka nights: Очень приятно!), Giulia (for taking care of all of us, Mamá Juliantra), Balasz (for teaching me that someone can be more stubborn), Harmen, Jan (for pampering nicely our lasers), Marloes (Ay, ay, ay! Gracias por ayudarme a no volverme loco con la tesis, dankjewel), Rahul and Aditi (for sharing your passion towards science, it has very nice talking to you. Hope we keep in touch).

Apart from its scientific contributions, AMOLF is a wonderful box where wonderful people meet, and so I would like to thank more people that make my time

at AMOLF something special: Jacopo (nothing particular but your memory bring always a smile to me and the urge to share memes), Agata (it's really bad that we met in a late stage of our PhD. I am sure that your twisted mind would make me laugh insanely), Tzeni (Tzeeeeeni Kontoleta Burrito, thanks for always provoking a smile in me), Parisa (for being such a positive person and for introducing us the authentic Iranian food), Federica (for your very sharp and smart comments that hide a twisted mind), Cristina (I think you are part of this twisted mind crew), Giorgio (ya sé lo que quieres, princesa), Agustin (y seguro tú no dirás que no), Said (es en verdad un orgullo verte dándole galleta y sacando el fua como los grandes), Hans (for your weird but interesting conversations full of irrelevant and controversial questions), Clyde (one of the real bosses in AMOLF), Lukas (for being always up for coffees and cheerful talks), Yarik (Люблю, куплю, поедем) and to all those who I may have forgotten.

In addition, I also want to thank people who did not directly impact the work presented in this thesis. Yet, they had an impact in my academic formation: all my professors and supervisors both in Mexico and in Germany, in particular to David Delepine (merci beaucoup), Juan Barranco (gracias) and Stavros Christopoulos ($ευχαριστώ\ πολύ$) whose words and lessons resonated with my interest and gave me the strength and the confidence needed for pursuing a PhD. Thanks also to all those who became my friends along my adventure in physics and were of unconditional support. Agradezco enormemente a las suripantas del IFUG incluyendo a Victor Colombias, pero en particular a mi inseparable partner Paulina el Cholillo con Cuchillos Rocha. A César, que me enseñó cómo se rascan los burros y el arte alterado de mentir al extremo. A la simplesa y el humor de los mimosos (Compadre, Manu y #PPP), ¡Caipirinhaaaaa! Ich danke auch meinen Pendejos Deutschen Freunden, Andreas, Charlotte, Dilege und Tim, für eure Freundschaft. I thank the Dynamite group (Ilkin Chocorona, Rip, Pau, Tyler (and Dr. Cage)), Tatjana, Luka and Pritam for your support and for sharing dreams, drinks and emotions over the time of my master and PhD.

One thing that no one explained to me when I started was that Amsterdam would give me a wide spread of good friends within and beyond UvA and Amolf that slowly became a weird family of people from all over the world. I would like to mention the Latino crew imported from Bonn: Miguel, Rebeca, Maricel, Arturín, Eugenio, Margarita, Angela, and Fer. The Mentirosos Latino Eastern crew: Leo, Doyito, Dulia, Abel, and Parisa (I hope we continue our mentiras and friendship for long long time). To Rob (thanks for helping me with your Dutch abilities), Alina, Anna Banana and Yaroslav who can transform any meeting into a wonderful moment. To our King's day partners Camila and Robbert/Cornelius (I wish you always have good evenings). To Myrsini and Dimitris for making any time a joyful moment of laughter. Kristy, thanks for polishing my introduction, and I hope we have more wine at your fantastic terrace. To Ludwin and Stijn, the most spontaneous Amsterdam westerns.

Я хочу поблагодарить семью Кулаковых и семью Бурундуковых за интерес в моей докторской работе и в нашей жизни в Амстердаме. Большое спасибо за участие и помощь в ремонте, происходившему одновременно с работой над докторской диссертацией. Кроме того, спасибо за огурчики, сало, водку и варенье! Для вас Заключение переведено на русский язык.

A mi familia que siempre insistieron y enfatizarion lo valioso que era estudiar, que me impulsaron a explorar mis propias capacidades y que sin entender la empresa en la que me embarqué hace 8 años lejos de México siempre confiaron en mí. Belis y Pelonchas, agradezco que con su ejemplo, y a punta de remolinos y jalones de greñas, me hayan enseñado que los éxitos se contruye con sacrificio, esfuerzo y perseverancia. Sin ustedes nada de esto hubiera occurido. Adriana Gordis, Armida y Guillermina Orangután, quiero agradecerles todo su cariño, lecciones y regaños (para aprender algo de disciplina sirvieron todos esos chingadazos). Pareja, nunca olvides que en este mundo matraca, esa es la única certeza que tenemos. Pedro, que nos mostraste que las conversaciones sobre historia o chismes siempre son mejores con un buen café y/o un arroz con leche. Y a toda la bola de puñales desde Uriel a Demián que mucho aprendimos juntos. Gracias a todos porque seguro me seguirán apoyando incondicionalmente.

And last but surely not least: Cabeza, Cabezota! No hay forma de agradecer tanto tanto apoyo. Sin pensártelo ni poquito buscaste siempre calmarme en mis momentos de desesperación durante el PhD, inluso desde el master. Pero lejos del apoyo en mis momentos más pesados, gracias porque fuiste el motor de muchas experiencias, aventuras y muchas chingaderitas: como haberme presionado para presentar parte de esta tesis en New Zealand (con un toque de tu propio interés por conocer aquellos astonishing places...and we made it). Porque contigo nunca pude aburrirme y seguro seguiré sin aburrirme con tu capacidad inacabale de generar ideas. Porque me basta escuchar “oye” para espantarme, y sé que sin saber lo que viene no hay argumentos para ir en contra. Eres energía (but not that that the universe believers claim), energía que me mantiene feliz, aterrorizado y sorprendido al mismo tiempo, energía que quiero mantener a mi lado. Compatir esta aventura, mis felicidades y mis logros es la mejor forma de expresar lo tanto que te quiero. Looking forward to the upcoming new adventures.

"Atl" (Nahuatl: water)
Aztec representation of water
emerging from the ground to
form streams and waves

Fejérváry-Mayer codex
prior to the Spanish conquest of Mexico (1521)